Integrated measurement-induced nonlinearity with superconducting detectors

Der Naturwissenschaftlichen Fakultät der Universität Paderborn
zur
Erlangung des Doktorgrades Dr. rer. nat.
vorgelegt von

Jan Philipp Höpker

Contents

Acknowledgements

I would like to thank J.-Prof. Dr. Tim J. Bartley for your outstanding support and for giving me the chance to work and grow in your research group. Thank you for your guidance, open ears, various opportunities, and being a great physics role model.
Next, I would like to thank everyone in the Mesoscopic Quantumoptics and Integrated Quantumoptics group. I really enjoyed every day, working and learning with you. Special thanks to Dr. Thomas Hummel, Nina Lange, Maximilian Protte, and Timon Schapeler for your support with writing this thesis. I want to thank Prof. Dr. Christine Silberhorn for giving me the chance to work in your labs and Prof. Dr. Jan Sperling for extensive discussions. I also want to thank all former colleagues, especially Dr. Evan Meyer-Scott, Dr. Johannes Tiedau, and Moritz Bartnick.
I want to thank Dr. Richard P. Mirin and Dr. Sae Woo Nam for giving me the chance to work with your team at NIST in Boulder. Dr. Thomas Gerrits, Dr. Adriana E. Lita, and Dr. Varun B. Verma, working with you was very inspiring and I cannot thank you enough for your support beyond the months in Boulder.
I also want to thank the funding agencies Bundesministerium für Bildung und Forschung and Deutsche Forschungsgemeinschaft and with it all members of the SFB/TRR142 Tailored Nonlinear Photonics.
Last but not least, I want to thank my family and friends and most of all Pia Sundermann.

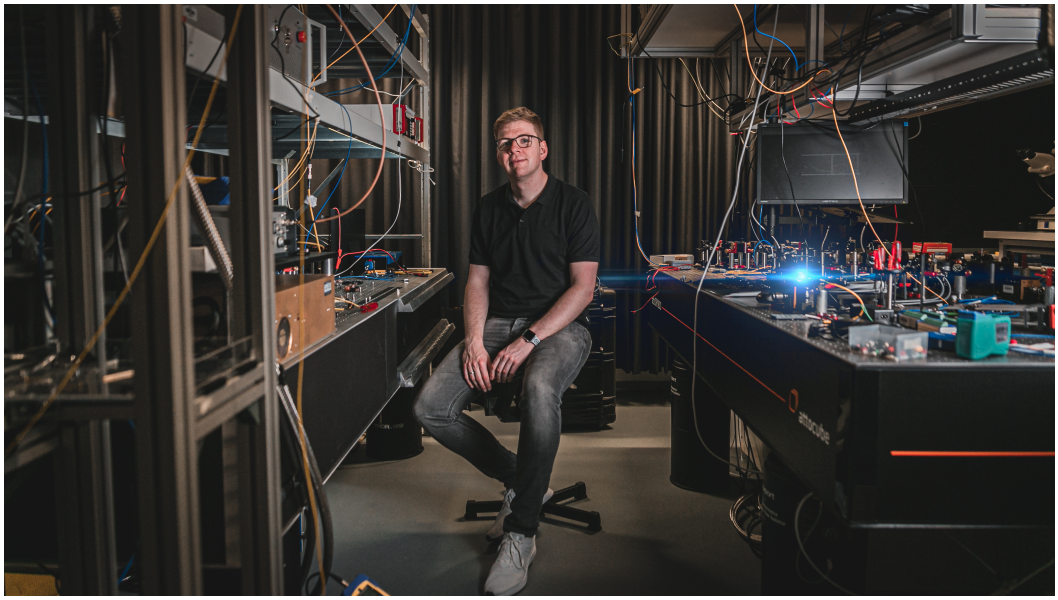

Abstract

In quantum mechanics, a measurement influences the quantum state you are observing. While this complicates the investigation of raw quantum states, it might also be used to create interesting new quantum states.

In this work, photon subtraction implemented with a single-photon measurement (a particle- like phenomenon) is combined with the interference of two quantum states (a wave-like phenomenon). Resulting complex photon-number correlations of a two-mode output state are investigated theoretically and experimentally using coherent states from a pulsed laser and single photons from a spontaneous parametric down-conversion source as the inputs. Furthermore, developments in technology and devices enabling these experiments on an integrated platform, namely titanium in-diffused lithium niobate, are explored. This includes the work on integrating superconducting single-photon detectors on waveguides, the realization of passive integrated optical routing structures, and multi-channel interfacing.

Zusammenfassung

In der Quantenmechanik wird der beobachtete Quantenzustand immer von einer Messung beeinflusst. Dies erschwert die Erforschung reiner Quantenzustände, kann jedoch auch zur Erzeugung neuer Quantenzustände genutzt werden.

In dieser Arbeit wird die Photonensubtraktion, umgesetzt durch eine Einzelphotonenmessung (ein teilchenartiges Phänomen), mit der Interferenz zweier Quantenzustände (ein wellenartiges Phänomen) kombiniert. Die daraus hervorgehenden komplexen Photonenzahlkorrelationen des Zwei-Moden-Ausgangszustands werden theoretisch und experimentell erforscht. Hierbei werden ein kohärenter Zustand eines gepulsten Lasers und einzelne Photonen einer Parametrischen Fluoreszenz-Quelle als Eingangszustände verwendet. Außerdem wird die Entwicklung im Bereich der Technologie und Bauelemente zur Ermöglichung dieser Experimente auf einer Integrationsplattform, hier Titan-eindiffundierte Wellenleiter in Lithiumniobat, untersucht. Dies beinhaltet die Integration supraleitender Einzelphotonendetektoren auf Wellenleitern, die Realisierung passiver, integrierter optischer Schaltkreise und Mehrkanal-Schnittstellen.

Introduction 1

The measurement of light is part of our everyday life. We measure light when taking photos using digital cameras, when using brightness sensors, and motion detectors in our front yard. We use interference phenomena or the speed of light for precise distance measurements, even in space-applications [1] and LIDAR (Light detection and ranging) [2]. Essential for our everyday life, we send and detect light for communication via optical fibers and satellites [3]. Especially, optical communication can be taken as an archetypal example of how scientific progress directly relates into immense improvement. By making light measurement more efficient, more information can be transferred in less time [4]. In this context, "more efficient" means lower loss, lower noise, faster detection, and the ability to package more information into less information carriers. In the extreme, this directly points towards quantum optics, where single photons (the smallest units of light) are investigated. The wish for high-efficient single-photon detectors to readout information becomes obvious. In addition, the quantum nature of photons is particularly important for example in quantum key distribution (QKD) [5], boson sampling [6], and investigating local realism in nature in loophole-free Bell tests [7].

While, intuitively, a measurement does nothing more than assigning numbers to a certain physical state you want to observe, it is well known in quantum mechanics that a measurement also effects the quantum state you are measuring [8] (pp. 304-307). This is a hard problem if you want to investigate raw quantum states and is tackled, for example, by quantum detector tomography [9, 10], but it can also be used to manipulate quantum states. Consequently, a measurement provides exciting possibilities for the creation of new quantum states [11].

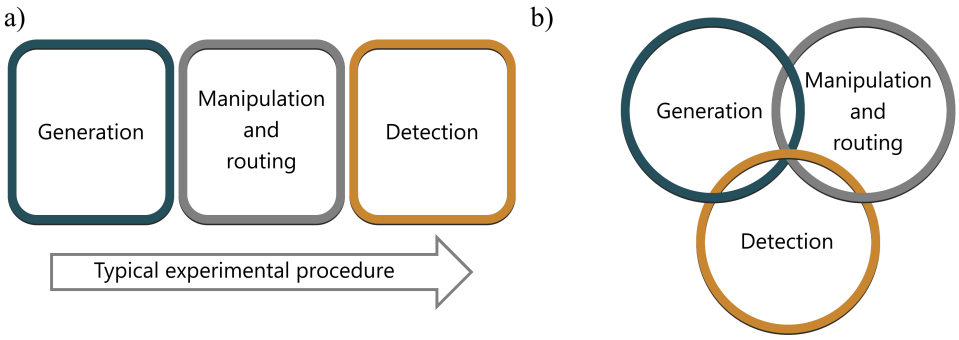

Figure 1.1: Illustration of an experimental procedure, separated in different building blocks. In a), the building blocks are aligned in a clear order from left to right, corresponding to most optics experiments. In b), this order is broken up and the boundaries of the building blocks overlap.

Figure 1.1 a) illustrates a typical optical experimental procedure. The experiment starts with the generation of a photonic state created by some source, for example photon emission from a quantum dot. It is followed by the manipulation of the state, such as a polarization rotation and routing in fiber. In the end, the output state is analyzed using detectors. A consequence of measurement operations in quantum physics is that a measurement can also contribute to the generation and manipulation of a quantum state, as illustrated in Figure 1.1 b). In addition, the boundary between generation and manipulation is also overlapping. This results in more flexibility and more complex setup architectures.

The work in this thesis can be placed in the overlap of the generation and detection building blocks in Figure 1.1 b), explicitly looking at nonlinear changes in the quantum state caused by a measurement operation. As the differentiation between measurement and detection can be inconsistent, this thesis defines a measurement as the operation itself while detection corresponds to the process in a device.

The most prominent example for the intersection of photon generation and measurement (see Figure 1.1 b)) is heralding of a spontaneous parametric down-conversion (SPDC) source which is the "*most studied photon-pair production process and the most used for single-photon generation in quantum information applications*" [12] (p. 16). The outcome of a heralded SPDC source can be seen as an approximation to a pure single-photon state in the photon-number (Fock) basis [13]. SPDC is a nonlinear process where (in a nonlinear medium) a higher-energy photon of a pump beam decays into two lower-energy photons [12] (p. 352). The pairwise created lower-energy photons can be separated using a polarizing beam splitter (PBS) for type-II SPDC and form a two-mode squeezed vacuum (TMSV) state [8] (p. 187). Type-II SPDC corresponds to perpendicular polarization direction of the output photons, fulfilling momentum conservation in the nonlinear medium. Ignoring one arm of the beam splitter results into a thermal photon-number distribution in each arm. If loss is neglected, the photon-number measurement in one arm guarantees the presence of the same photon number in the other arm. Due to the intrinsically low and purely probabilistic nonlinear effect, even the usage of non-photon-number-resolving detectors (click-detectors) results in a good approximation of a single-photon Fock state at low pump powers [13]. For the example of SPDC, the measurement changes the photon-number statistics in one arm of the PBS from a thermal distribution to a single-photon Fock state [12] (p. 389).

There are also more examples for measurement-induced states, explicitly photon subtraction to create number-correlated pairs of coherent states [14] and Schrödinger cat states [15]. Photon subtraction is not per se a measurement but can be experimentally realized with specific measurement schemes [16]. In a lossless scenario, the photon-number measurement in one arm of a beam splitter provides the information of how many photons are subtracted from an input state. Post-selecting on the events of measuring exactly n photons equals to a photon subtraction of n photons. Therefore, the measurement operation is a critical part of the experimental realization of photon subtraction. The beam splitter's splitting ratio can be used to adapt the occurrence of these events, given a certain input state. Several groups have shown applications of this scheme to create interesting quantum states from various input states, such as thermal light [17], squeezed vacuum [15,

18–20], and TMSV [14]. All of them follow the motivation of creating new and exotic photonic quantum states which are classically not available and which serve as resources for applications in quantum information and quantum metrology.

The nonlinear influence of photon subtraction or, generally, any measurement in general becomes more prominent when exploring the combination of photon addition and photon subtraction. While the simultaneous addition and subtraction of one photon should classically not affect the output state, Reference [21] and [22] investigate the effect of a quantum catalysis scheme. Bartley et al. have shown the creation of squeezing using one-photon addition and one-photon subtraction. This mechanism can also be adapted to create discorrelated states, as shown in Reference [23]. As stated before, using a measurement in combination with different input states results in an interesting class of quantum states and induced nonlinearities.

A final example builds on the aforementioned findings of Reference [21]. While they investigated single-mode squeezing using a single photon and coherent state as their input states for their photon subtraction as the partial measurement, the scheme can be extended to investigate two-mode squeezing as presented by Riabinin et al. [24]. As mentioned earlier, a TMSV state can also be created in a parametric down-conversion pulse, where the squeezing depends on the pump power. The authors have shown theoretically that it is possible to create measurement-induced two-mode squeezing which is less dependent on pump power and therefore attractive for quantum experiments in the low photon-number regime [24].

All mentioned examples point at the versatile optical toolbox for quantum-physical experiments and applications. While the need of high-efficient single-photon detectors is obvious, and superconducting detectors are currently the most promising candidates [12] (p. 13), the development and exploration of a platform for working with these fragile but powerful optical quantum states is a task of great interest. Integrated optics is a promising technique to enable complex, scalable, phase-sensitive, and low-loss experiments [25], all of which can have a great impact on our fundamental understanding of quantum physics and quantum-technological applications. Therefore, this work covers quantum optics experiments on measurement-induced nonlinearity as well as developments in technology and devices enabling these experiments on an integrated platform (titanium in-diffused lithium niobate). The latter includes the work on integrating superconducting single-photon detectors on waveguides, the realization of passive integrated optical routing structures, and multi-channel interfacing. The former comprises of exploring created quantum states using single-photon detection as well as interference between different optical input states. With this, widely applicable technologies as well as exotic two-mode quantum states with complex correlations are investigated.

The thesis is structured as follows. In Chapter 2, the theoretical background based on photon statistics is given. In Chapter 3, the optical setup for generating the input states, used to investigate measurement-induced nonlinearities, is introduced and characterized. Chapter 4 continues with the individual building blocks for the integrated circuit. In Chapter 5, measurement-induced nonlinearities are investigated using an integrated circuit but

external superconducting detectors. In Chapter 6, the work on integrating superconducting single-photon detectors on titanium in-diffused lithium niobate waveguides is presented, followed by a conclusion and an outlook in Chapter 7.

Theoretical background 2

As introduced in Chapter 1, a measurement can be used to induce nonlinearity. To this end, the framework for the later experimentally investigated quantum states is elaborated in this chapter underpinned with computer simulations. Firstly, different flavors of quantum states are introduced and investigated using photon-number probability distributions. Secondly, the concept of spontaneous parametric down-conversion for creating single photons is explained. Then, Section 2.3 covers theoretical work on interference of two quantum states, while Section 2.4 closes with the theoretical investigation of measurement-induced nonlinearities neglecting loss effects.

2.1 Introduction to quantum states

The introduction to quantum states goes back to the quantization of the electromagnetic field. Following the formalism in Reference [8] (pp. 10-15), given Maxwell's equations with suitable boundary conditions, one can find an analogy between the resulting field energy of a single-mode electromagnetic field and a harmonic oscillator, with the Hamiltonian $\hat{H}$ given as

$$\hat{H} = \frac{1}{2}(\hat{p}^2 + \omega\hat{q}^2). \tag{2.1}$$

Here, $\hat{p}$ and $\hat{q}$ are the operator equivalents to the generalized position and its conjugate momentum variables q and p in a classical system, and ω is the angular frequency.The representation of these variables as the real and imaginary part of an electromagnet field's amplitude can be found in Appendix A.1. Conventionally, it is possible to introduce the non-Hermitian annihilation $\hat{a}$ and creation $\hat{a}^\dagger$ operators in the form

$$\hat{a} = (2\hbar\omega)^{-1/2}(\omega\hat{q} + i\hat{p}), \tag{2.2}$$

$$\hat{a}^\dagger = (2\hbar\omega)^{-1/2}(\omega\hat{q} - i\hat{p}). \tag{2.3}$$

It holds that

$$[\hat{a}, \hat{a}^\dagger] = 1. \tag{2.4}$$

With Equation (2.2) and (2.3) one can write the Hamilton operator as

$$\hat{H} = \hbar\omega\left(\hat{a}^\dagger\hat{a} + \frac{1}{2}\right). \tag{2.5}$$

The energy eigenstates n of this Hamiltonian are described by

$$\hat{H}\,|n\rangle = E_n\,|n\rangle \tag{2.6}$$

From the harmonic oscillator it is known that the discrete energy levels E_n are given as

$$E_n = \hbar\omega\left(n + \frac{1}{2}\right) \text{ with } n = 0, 1, 2, 3... \tag{2.7}$$

The name creation operator for $\hat{a}^\dagger$ comes from

$$\hat{H}\hat{a}^\dagger\,|n\rangle = \hbar\omega\left(\hat{a}^\dagger\hat{a}\hat{a}^\dagger + \hat{a}^\dagger\frac{1}{2}\right)|n\rangle = \hat{a}^\dagger(E_n + \hbar\omega)\,|n\rangle = (E_n + \hbar\omega)(\hat{a}^\dagger\,|n\rangle). \tag{2.8}$$

This can be seen as an addition of one photon with energy $\hbar\omega$. The opposite holds for the annihilation operator $\hat{a}$ but is lower bounded by

$$\hat{a}\,|0\rangle = 0. \tag{2.9}$$

The operator $\hat{n} = \hat{a}^\dagger\hat{a}$ gives

$$\hat{n}\,|n\rangle = n\,|n\rangle\,, \tag{2.10}$$

and is therefore called the number operator. With these basics, every photon-number state can be formed from the vacuum, using

$$|n\rangle = \frac{(\hat{a}^\dagger)^n}{\sqrt{n!}}\,|0\rangle\,. \tag{2.11}$$

A graphical representation of photon-number probability distributions for the vacuum state and the one-photon or two-photon Fock state are shown in Figure 2.1.

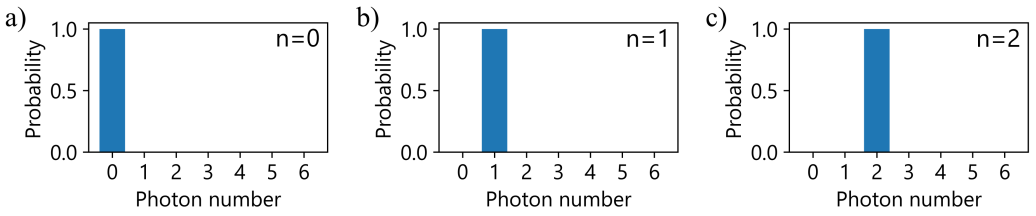

Figure 2.1: Photon-number probability distribution for a) the vacuum state, b) a one-photon Fock state, and c) a two-photon Fock state. The unity probability show the purity of the photon-number states.

Even though this model does not yet take different modes and phase into account, it can also represent different photon-number distributions such as coherent states (the physical output of a laser). The amplitude of a coherent state α is related to the mean photon number

$\bar{n}$ as $\bar{n} = |\alpha|^2$. In the number basis, one can represent the coherent state as

$$|\alpha\rangle = \mathrm{e}^{-\frac{1}{2}|\alpha|^2} \sum_{n=0}^{\infty} \frac{\alpha^n}{\sqrt{n!}} |n\rangle \,. \tag{2.12}$$

Figure 2.2 shows the photon-number probability distribution for coherent states with mean photon numbers of 0.1, 1.0, and 2.0, following a Poisson distribution [8] (p. 46). In Figure 2.2 a), photon numbers higher than one only occur at a very low probability. In contrast, at a mean photon number of $\bar{n} = 1$ the probability of zero photons, exactly one photon, or the sum of all higher photon numbers are equal to each other, shown in Figure 2.2 b). When measuring a coherent state with a mean photon number of $\bar{n} = 2$, it is equally likely to measure exactly one photon or two photons, as shown in Figure 2.2 c).

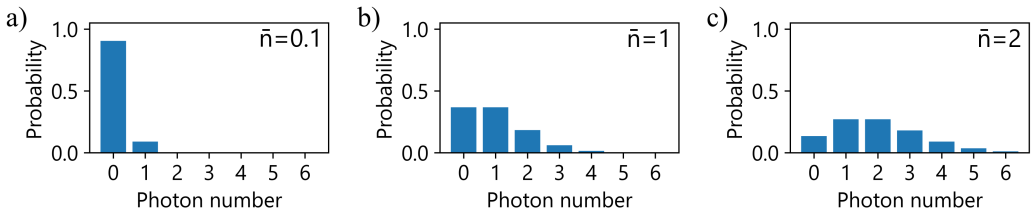

Figure 2.2: Photon-number probability distributions of coherent states with a mean photon number of a) $\bar{n}$=0.1, b) $\bar{n}$=1.0, and c) $\bar{n}$=2.0.

In contrast, Figure 2.3 shows the photon number probability distributions for thermal states (as black-body radiation) with the same mean photon numbers as used for the coherent states in Figure 2.2 following a Bose-Einstein distribution. When comparing the shown photon-number probability distributions, the distributions of a coherent state and a thermal state look very similar at low mean photon numbers. At higher photon numbers, they deviate significantly, especially from the single-photon Fock states. Therefore, coherent states and thermal states are generally not good approximations of pure single-photon Fock states. In addition, the probability of measuring zero photons for a thermal state is always the highest at any mean photon number.

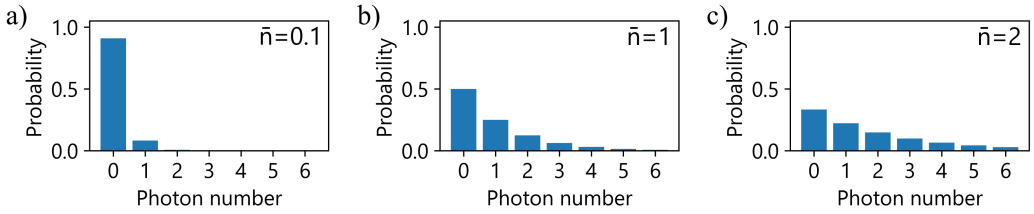

Figure 2.3: Photon-number probability distributions of thermal states with a mean photon number of a) $\bar{n}$=0.1, b) $\bar{n}$=1.0, and c) $\bar{n}$=2.0.

2.2 Spontaneous parametric down-conversion

As shown in the previous section, single-photon states can be intuitively represented in the photon-number basis. However, the physical creation of single-photon Fock states is rather challenging as coherent or thermal states are non-ideal candidates. Therefore, spontaneous parametric down-conversion as a source for single-photon states is discussed further.

The underlying physics rely on the polarization response $\hat{P}_\mathrm{i}$ of a dielectric medium with its electric susceptibility tensor elements χ to an electro-magnetic field $\hat{E}$ as (Reference [12] (p. 354))

$$\hat{P}_i = \chi^{(1)}_{i,j}\hat{E}_j + \chi^{(2)}_{i,j,k}\hat{E}_j\hat{E}_k + \chi^{(3)}_{i,j,k,l}\hat{E}_j\hat{E}_k\hat{E}_l + \dots \tag{2.13}$$

Using a suitable nonlinear crystal for SPDC, one can focus on the $\chi^{(2)}$-interaction, while the $\chi^{(3)}$-interaction is important for 4-wave mixing. SPDC creates two output fields with one input field and can therefore be seen as the counterpart of sum-frequency generation. Based on Reference [8] (p. 214), for the nondegenerate case, it holds the relation that

$$\hat{H} \sim \chi^{(2)}\hat{a}_\mathrm{p}\hat{a}^\dagger_\mathrm{s}\hat{a}^\dagger_\mathrm{i} + H.c. \tag{2.14}$$

Here, $\hat{a}_\mathrm{p}$ is the annihilation operator for the pump-photon and $\hat{a}^\dagger_\mathrm{s}$ and $\hat{a}^\dagger_\mathrm{i}$ are the creation operators for the signal and idler photons. With initially no photons in the signal and idler states,

$$\hat{a}_\mathrm{p}\hat{a}^\dagger_\mathrm{s}\hat{a}^\dagger_\mathrm{i} \left|1\right\rangle_\mathrm{p} \left|0\right\rangle_\mathrm{s} \left|0\right\rangle_\mathrm{i} \Rightarrow \left|0\right\rangle_\mathrm{p} \left|1\right\rangle_\mathrm{s} \left|1\right\rangle_\mathrm{i}. \tag{2.15}$$

It has to be noted that this process happens spontaneously and simultaneously. Therefore, the process has to fulfill energy and momentum conservation which can be transferred to conservation of frequency ω and wavevector k as

$$\omega_\mathrm{p} = \omega_\mathrm{s} + \omega_\mathrm{i}, \tag{2.16}$$

$$k_\mathrm{p} = k_\mathrm{s} + k_\mathrm{i}. \tag{2.17}$$

The latter is tackled either by finding a suitable spatial configuration for the nonlinear crystal, addressing the specific output angles of signal and idler photons, or by using a periodic inversion of the crystal orientation (periodic poling). This adds an additional term to Equation (2.17) for so-called quasi-phase-matching.

$$k_\mathrm{p} = k_\mathrm{s} + k_\mathrm{i} + k_\mathrm{c}, \tag{2.18}$$

where $k_\mathrm{c} = 2\pi/\Lambda$ is an additional term from the crystal's (first order) poling period Λ. With this, it is possible to achieve copropagation of signal and idler photons, which allows these processes also to work in waveguides [26] .

Further elaborating Equation (2.16) and (2.17) as the pump-distribution function $\alpha(\omega_s + \omega_i)$

and the material-dependent phase-matching function $\Phi(\omega_s, \omega_i)$, it is possible to calculate the full joint spectral intensity (JSI) F as

$$F = (\alpha(\omega_s + \omega_i)\Phi(\omega_s, \omega_i))^2 \tag{2.19}$$

Figure 2.4 shows the resulting JSIs for the same pump-distribution function but two different phase-matching functions based on the nonlinear crystals lithium niobate and potassium titanyl phosphate (KTP). It can be seen, that the combination of pulse bandwidth and phase-matching function which includes the crystal dispersion, poling period, and crystal length, determines whether there exist spectral correlations between signal and idler photons. Depending on the application, some experiments require these correlations while others require non-correlated signal and idler pairs [27].

Reference [28] shows that these correlations can be elaborated from orthogonal Hermite-Gauss modes (also called Schmidt modes) and that these modes can further be used for information encoding. However, as indistinguishable photons are needed for the later experiments, the reduction to one mode (Schmidt number = 1) is necessary.

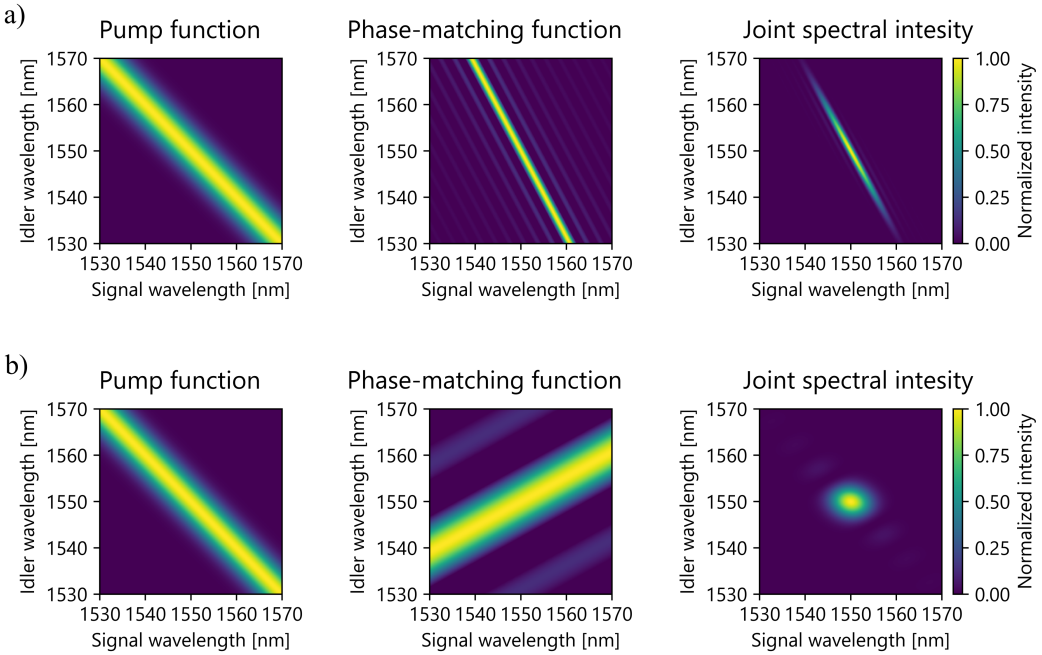

Figure 2.4: Pump function, phase-matching function, and resulting JSI from left to right for a) lithium niobate and b) KTP.

While signal and idler photons are always created pairwise and entangled, the individual photon-number probability distributions look like thermal distributions due to the spontaneous character of the process [8] (p. 186). Together, they can be described as a two-mode squeezed vacuum sate (in one Schmidt mode), where signal and idler form one

state with their strong correlations in photon number [29]. Their joint, highly correlated photon-number probability distribution is shown in Figure 2.5.

When deterministically separating signal and idler photons and measuring the photon number of the idler, one can directly infer the photon number in the signal arm, which is called heralding. Therefore, the idler photon is sometimes called herald photon. While the occurrence of signal and idler creation in SPDC is still probabilistic, one can postselect on these occasions. At low generation rates, it is sufficient to approximate the signal arm to a pure single photon postselected on the measurement of any photon number in the idler arm [13].

Other single-photon sources such as quantum dots or color centers in crystals don't rely on a probabilistic process which can be advantageous. However, the single-photon source of choice strongly depends on the application. In the following section, advantages of SPDC sources which are important for this work are discussed that have not been considered, yet.

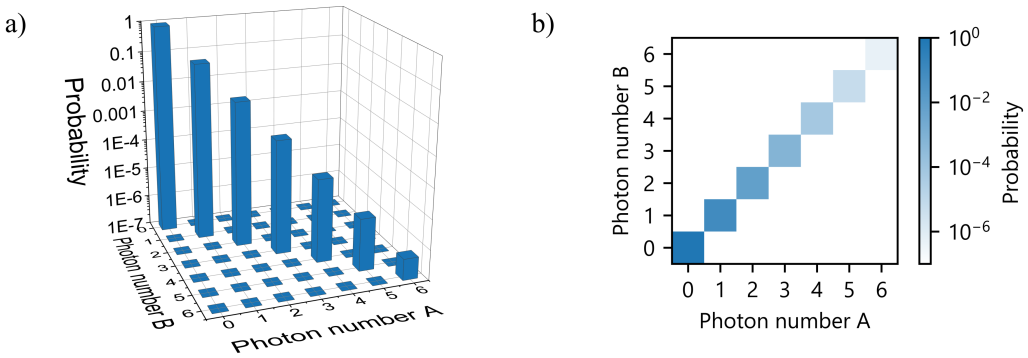

Figure 2.5: Joint photon-number probability distributions for signal and idler photons (A and B) of a two-mode squeezed vacuum state (SPDC state) in a) a logarithmic 3D bar chart and b) colormap representation.

2.3 Single-photon interference

Single photons are powerful information carriers due to the many bases in which information can be encoded [4]. These bases are directly related to the different ways two photons can be distinguished as for example spatial, temporal, and frequency modes [30]. Here, SPDC has proven to be well suited for reliable preparation of single photons [31]. While distinguishability between photons is at first sight advantageous for information encoding, it hinders the interaction of two photons [30].

Many interference phenomena from classical optics can be directly translated to quantum optics. As an example in Figure 2.6, four different outcomes can occur when two distinguishable photons A and B (red and orange) interfere at a 50:50 beam splitter, for example

in the form of an integrated directional coupler. In Figure 2.6 a), both photons chose the left arm after the integrated coupler. In Figure 2.6 b), both photons cross at the beam splitter and therefore arrive at different outputs. In Figure 2.6 c), both photons stay at their initial waveguide side, such that photon A stays in the left waveguide and photon B stays in the right waveguide. In Figure 2.6 d), photon A and B bunch together and leave at the right output.

The outcome after the beam splitter (BS) with the operator $\hat{U} = e^{i\frac{\pi}{4}(\hat{a}^\dagger\hat{b}-\hat{a}\hat{b}^\dagger)}$ can be written as (Reference [8] (pp. 139-141))

$$\hat{U}\,|1,1\rangle \xrightarrow{BS} \frac{1}{2}(i\hat{a}^\dagger\hat{a}^\dagger + \hat{a}^\dagger\hat{b}^\dagger - \hat{b}^\dagger\hat{a}^\dagger - i\hat{b}^\dagger\hat{b}^\dagger)\,|0,0\rangle\,. \tag{2.20}$$

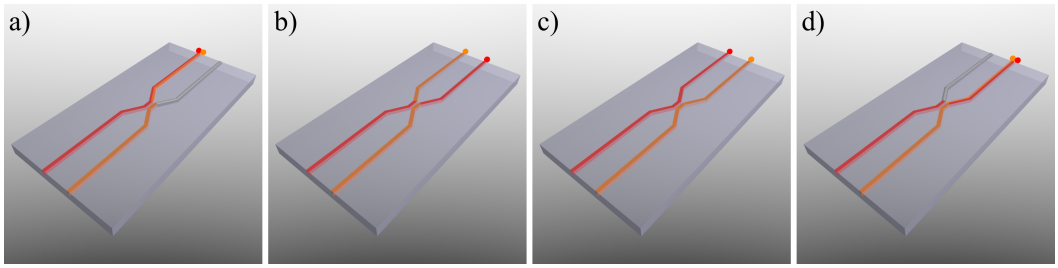

Figure 2.6: Two-photon interference at a 50:50 beam splitter in form of an integrated directional coupler. In this waveguide circuit (represented by gray lines on the rectangular sample), two input photons can enter at the two bottom left inputs and meet in the narrowed region in the middle, before leaving at the two outputs. The four figures show the four different outcomes as described in the main text. The red and orange lines illustrate the pathways, the two photons take.

For two indistinguishable photons, the two middle terms in Equation (2.20) cancel out, resulting in the output state

$$|\Psi\rangle = \sqrt{\frac{1}{2}}i(|2,0\rangle - |0,2\rangle). \tag{2.21}$$

Therefore, when two indistinguishable photons interfere at a 50:50 beam splitter, the two photons bunch together, called the Hong-Ou-Mandel (HOM) effect [32]. This means that no simultaneous detection of one photon at each output is possible. The joint photon-number statistics are depicted in Figure 2.8 a). For distinguishable photons, the maximum probability of a simultaneous detection of one photon at each output according to Equation (2.20) is 0.5. If one can change the distinguishability of the photons, the ratio of the coincidental measurement of (at least) one photon in both output arms for maximal distinguishable photons p_{ab} and maximal indistinguishable photons p_{aa}, gives the HOM visibility V, with

$$V = \frac{p_{\mathrm{ab}} - p_{\mathrm{aa}}}{p_{\mathrm{ab}}}. \tag{2.22}$$

The distinguishability of two photons is not discrete but continuous and can be observed in all previously mentioned bases.

The spectral mode of a photon can be introduced according to Reference [30] as

$$|1;\phi\rangle = \int d\omega \phi(\omega) \hat{a}^\dagger(\omega) |0\rangle , \tag{2.23}$$

where $\phi(\omega)$ is the spectral amplitude function and $\hat{a}^\dagger(\omega)$ the creation operator for the spectral mode ω. In addition, a temporal delay τ on one of the input modes can be introduced as

$$\hat{a}^\dagger(\omega) \rightarrow \hat{a}^\dagger(\omega) e^{i\omega\tau}. \tag{2.24}$$

When choosing a Gaussian spectral distribution for both input photons with equal spectral width σ, unequal central frequencies $\bar{\omega}_a$ and $\bar{\omega}_b$, and a relative temporal delay τ between the modes, the visibility transforms to (Reference [30])

$$V = \frac{\frac{1}{2} - \left(\frac{1}{2} - \frac{1}{2} e^{-\frac{\sigma^4\tau^2 + (\omega_a - \omega_b)^2}{2\sigma^2}}\right)}{\frac{1}{2}} = e^{-\frac{\sigma^4\tau^2 + (\omega_a - \omega_b)^2}{2\sigma^2}}. \tag{2.25}$$

It can be seen that the HOM visibility decreases for temporal or spectral mismatches of the two photons. This is illustrated in Figure 2.7 for three different spectral mismatches.

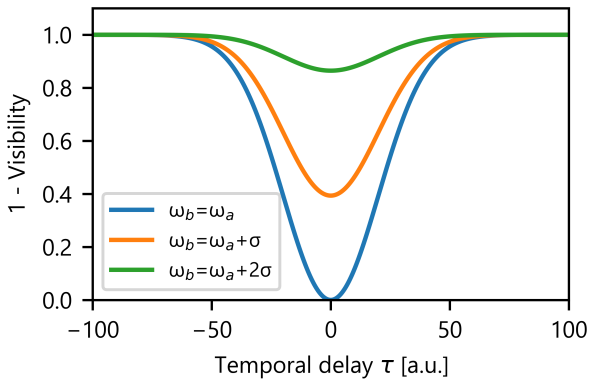

Figure 2.7: HOM visibility of two photons dependent on the temporal mismatch for three spectral mismatches based on Equation (2.25)

When interfering two single photons, the HOM visibility is often used as a measure for their distinguishability. This phenomenon can be expanded to higher photon orders as depicted in Figure 2.8 c)-d). The depicted as well as subsequent theoretical results in the form of colormap plots are based on Python QuTiP simulations [33]. The QuTiP package for Python is an open-source library and simulation tool based on commonly used numerical packages (Numpy, Scipy, and Cython) [34]. It directly provides the numerical implementation of Hamiltonians, as well as operators as the annihilation and creation operators, and density

matrices to represent quantum states as Fock states, thermal states, and coherent states. This way, we can directly implement optical circuits.

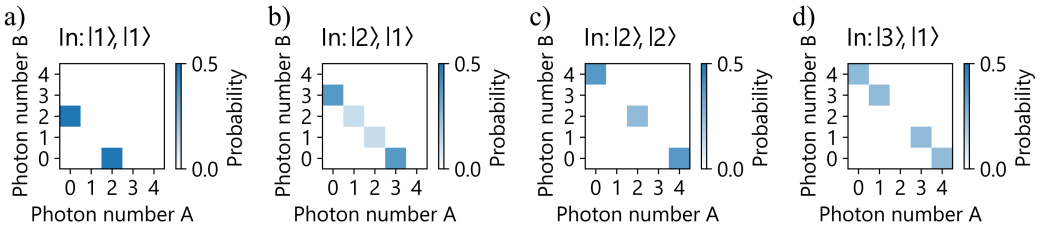

Figure 2.8: Photon-number statistics (probability distribution) in the two output arms of a 50:50 beam splitter after interference of: a) two indistinguishable single photons, b) a one-photon and a two-photon state, c) two two-photon states, and d) a one-photon and a three-photon state in the two input arms.

For comparison, Figure 2.9 shows the interference of vacuum with different photon-number states. Figure 2.9 a) shows the 50:50 chance for a one-photon state, measured either in port A or B. One can compare the photon-number statistics in Figure 2.9 b)-d) and Figure 2.8 a)-d) with the same total number of photons. As no multi-photon interference effects are involved in Figure 2.9 b) and c), the results differ drastically from the findings in Figure 2.8 a)-d). Most important, the interference effects in Figure 2.8 cannot be treated as a combination of other photon-number statistics, as also shown analytically in Appendix A.2..

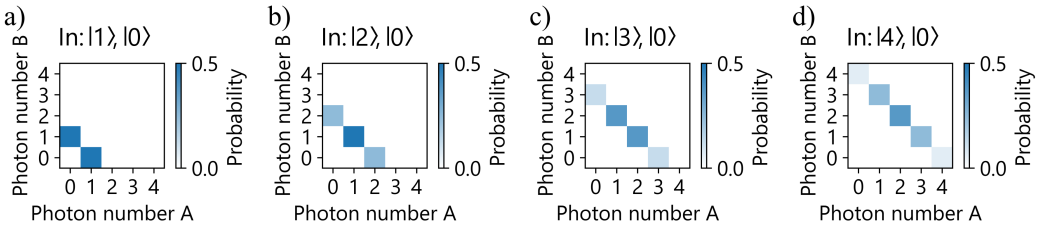

Figure 2.9: Photon-number statistics (probability distribution) in the two output arms of a 50:50 beam splitter after interference of a) a single photons, b) a two-photon state, c) a three-photon state, and d) a four-photon state and vacuum in the two input arms.

The Hong-Ou-Mandel effect can also be studied for other types of input states. For coherent states, the HOM visibility depends on the relative phase of the two input states in analogy to the classical case and is lower bounded by 50 % [12] (p. 505). In contrast, the interference of a single-photon Fock state and a coherent state is independent of a relative phase of the coherent input state. Since the mean photon number of a coherent state determines the multi-photon probability, the HOM visibility is lower bounded by the coherent-state amplitude [35]. This is true, even for otherwise perfectly indistinguishable photons. An analytical expression of the HOM visibility V for the interference of a coherent state and a single photon is given by (Reference [35])

$$V = \frac{|\alpha|^2}{2} \frac{e^{\frac{-|\alpha|^2}{2}}}{1 - e^{\frac{-|\alpha|^2}{2}}} \tag{2.26}$$

and is visualized in Figure 2.10.

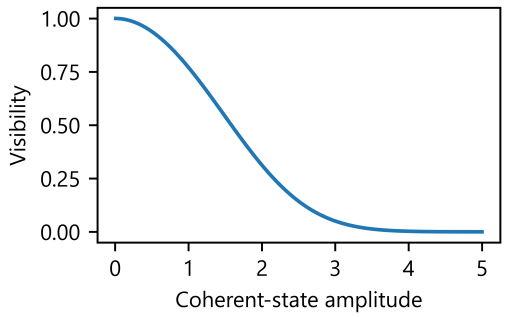

Figure 2.10: HOM visibility for the interference of a coherent state and single photon dependent on the coherent-state amplitude.

In addition, Figure 2.11 shows the photon-number statistics following interference between a single photon and a coherent state with amplitude (and mean photon number) of one, illustrating a discorrelated photon-number distributions [23]. Here, the creation of exotic two-mode quantum states with complex correlations in the joint photon-number statistics becomes visible. The measurement outcome for the photon number in both outputs cannot be predicted with 100 % certainty while measuring the same photon number in both outputs is prohibited.

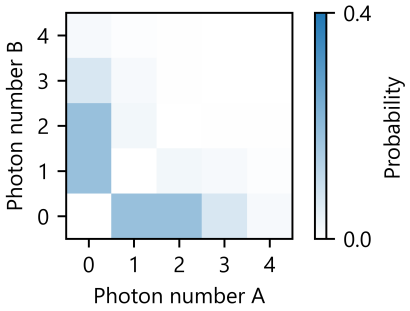

Figure 2.11: Photon-number statistics (probability distribution) in the two output arms of a 50:50 beam splitter after interference of a single photon and a coherent state with amplitude α=1 ($\bar{n}$=1).

Photon loss can be simulated by mixing the initial state with vacuum at a beam splitter [36] (pp. 79-83). As shown in Appendix A.3, including loss at the coherent-state input reduces the coherent-state amplitude which on the contrary increases the HOM visibility,

as shown in Figure 2.10. Using QuTiP simulations, we investigate the influence of loss on the single-photon state. As shown in Figure 2.12 a), the HOM visibility decreases with increasing loss. In Figure 2.12 b), one can see that this decreasing HOM visibility is not just caused by a decreasing probability for a coincidental measurement of at least one photon in both output arms for maximal distinguishable photons p_{ab} but also an increasing probability for maximal indistinguishable photons p_{aa}. Therefore, when investigating the HOM visibility for different quantum states as the interference of coherent states and single photons experimentally (see Chapter 5), the visibility cannot be interpreted as a measure of the indistinguishability in the earlier introduces basis. Furthermore, an individual blocking of the individual inputs cannot be used for a background subtraction.

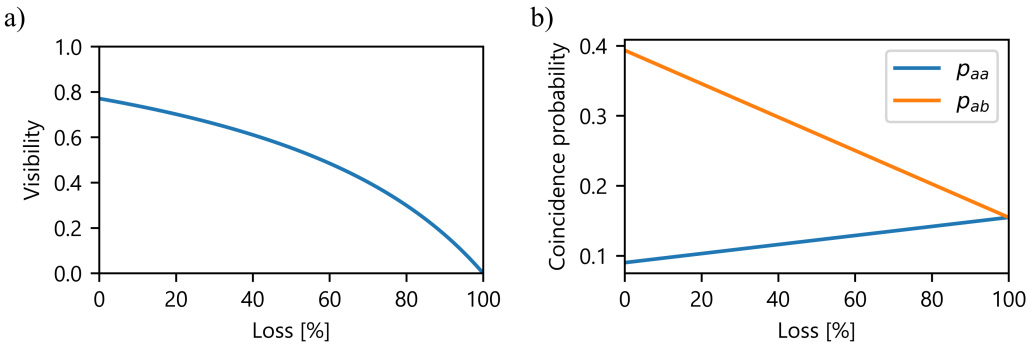

Figure 2.12: a) HOM visibility for the interference of a coherent state with amplitude α=1 ($\bar{n}$=1) and single photon dependent on loss at the single-photon input state, and b) corresponding probabilities for the coincidental measurement of at least one photon in both output arms (see Equation 2.22).

2.4 Measurement-induced nonlinearity

As photons lose all their energy when being detected, only a partial detection of a photonic state can be useful for quantum-state preparation. Partial detection of a photonic state can be realized for spatially separated states, where SPDC was introduced as an example in Chapter 1. In addition, a partial detection can be realized using the already introduced beam splitter [16], as illustrated in Figure 2.13. In this section, we investigate nonlinearities in the photon-number statistics based on this measurement scheme theoretically.

When sending only a coherent state into the beam splitter (vacuum in the other arm), the output statistics of the arm with no detector are independent of any detection event in the other arm. Therefore, postselecting on for example a detection of one photon in the detection arm and (according to Chapter 1) subtracting one photon does not change the photon-number statistics. This is shown analytically in Appendix A.3. The outcome photon-number probability distribution is independent of any photon-number measurement at the detector which is unique for these states.

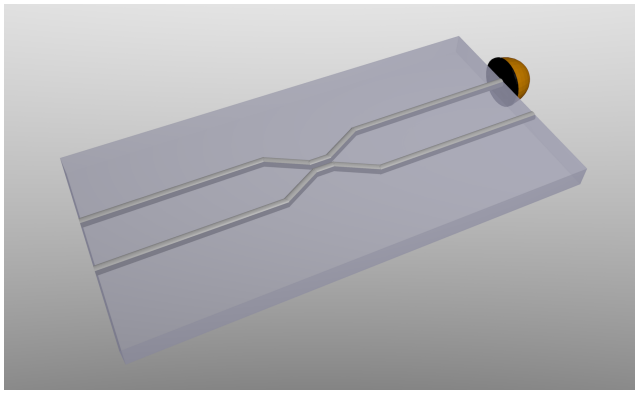

Figure 2.13: Illustration of a partial detection of a photonic state using a detector (represented by the orange hemisphere) in one arm of an integrated beam splitter introduced in Figure 2.6.

When we use a thermal state with the same mean photon number at the input ($\bar{n} = 1$) and postselecting on different photon-number measurements, the output statistics change from a Bose-Einstein distribution or super-Poissonian light to a Poisson distribution [17], as shown in Figure 2.14.

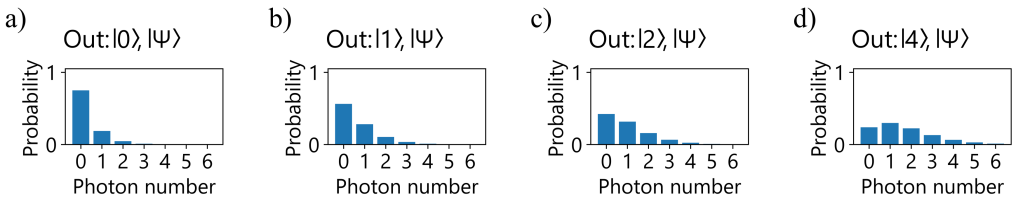

Figure 2.14: Photon-number probability distributions of one output of a 50:50 beam splitter (Ψ) with a thermal state with mean photon number of $\bar{n} = 1$ at one input, postselected on a detection of a) no photon, b) one photon, c) two photons, and d) four photons at the detector output, illustrated by the photon number in the first part of the labeled output state.

Changes in the photon statistics can also be investigated for the interference of a single photon and a coherent state. These results were already shown in Figure 2.11. However, when only looking at the joint statistics of this example, the unintuitive and interesting features of quantum mechanics are easily overseen. A measurement of a single photon in one arm corresponds to a one-photon subtraction. When considering a coherent state as the input, interfering it with a single photon, and executing a one-photon subtraction, the output state must include the same overall photon number as the input coherent state (quantum catalysis). Bartley et al. [21] showed that this process induces nonlinearity (especially quadrature squeezing up to 1.25 dB below the shot-noise limit).

In summary, with the simple scheme from Figure 2.13, it is possible to create strong nonlinearities, when using a coherent state and a single photon at the inputs and measuring

a single photon at the other output. This leads to the question, whether it is possible to create advanced two-mode output states as for example two-mode squeezed vacuum by extending the scheme.

2.4.1 Phase-independent optical circuit

We realize the extension of the previously discussed scheme by adding two more 50:50 beam splitters (BS 2 and BS 3 in Figure 2.15) to extend the number of spatial modes. As single-photon Fock states are phase insensitive and the states do not recombine after interference, the optical circuit is phase-independent. Here this means that all results are independent of the path lengths of the individual waveguide sections. As this circuit design is later compared to a second circuit, we call it *optical circuit A* in the following.

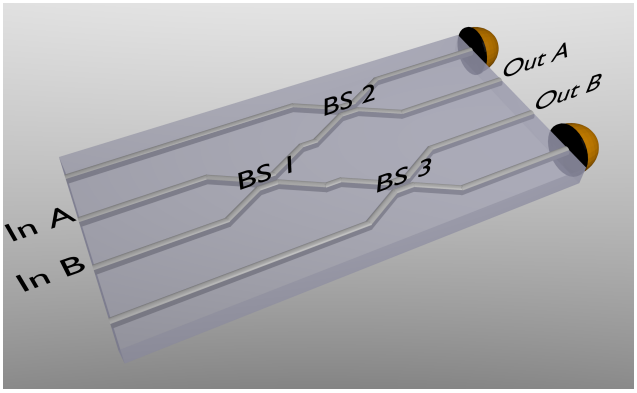

Figure 2.15: Optical circuit to create two-mode quantum states with three beam splitters. With respect to the measurement scheme in Figure 2.11, this circuit adds one beam splitter in each arm of the first beam splitter and a second detector. The two inputs are labeled with In A and In B, while the two modes of the output state are labeled Out A and Out B.

We use the two inputs to investigate the interference of a coherent state and a single photon. For first investigations the mean photon number and with it the amplitude of the coherent state is set to one photon. With no measurement at the two detectors, each arm of the first beam splitter undergoes 50 % loss, as seen in Figure 2.16 a). This loss cannot be eliminated by postselecting on a measurement of zero photons in both measurement output ports. Therefore, the corresponding results, shown in Figure 2.16 b), differ from the earlier findings in Figure 2.11 in terms of the absolute values but not the created discorrelation. In addition, the photon-number statistics are equal for an equal photon subtraction in both measurement output ports independent of the actual photon subtraction. For the cases of a subtraction of zero, one, or two photons, the results are shown in Figure 2.16 b) - c).

Instead, when only subtracting one photon in one of the arms, the photon-number statistics change drastically, as can be seen in Figure 2.16 e) - h). Here, the symmetry is broken. The probability of measuring a photon at the output of which another photon was subtracted

is higher than the probability of measuring a photon at the other output. In addition, the probability of measuring one photon in this arm is increased, compared to the cases a) - d). Therefore, the influence of the measurement operation is highly nonlinear.

In Figure 2.16 e) and f), the second measurement output is not observed, while in g) and h) a measurement on zero photons is executed. The difference of these cases becomes less prominent for lower mean photon numbers of the input coherent state, therefore the simulation results for higher mean photon numbers ($\bar{n}$=2 and $\bar{n}$=4) are shown in Appendix A.4.

While these examples are all using photon-number resolving detectors, non-photon-number resolving detectors (click detectors) are often more accessible in the laboratory. Therefore, we also investigate the photon-number statistics of the two-mode output state for the interference of a single photon and a coherent state with a mean photon number of one for click detectors. The results are presented in Figure 2.17.

When comparing the results for photon-number resolving detectors in Figure 2.16 and click detectors in Figure 2.17, the influence of a measurement is very similar. With the exception for the results of a symmetric photon subtraction at both measurement arms, as a click-detection event can be caused by unequal numbers of photons. In addition to the shown nonlinearities in the photon-number statistics and interesting correlations, further investigations by Riabinin et al. in connection with this work have shown that it is possible to induce two-mode squeezing with this design [24]. Usually, the amount of squeezing (using PDC) scales with the number of involved photons and is therefore limited by laser power or source brightness. This method provides a more effective way for generating squeezing per involved photons as the interacting states are all at the single-photon level. This is critical for future work where the detectors in the form of superconducting devices are integrated in an optical circuit and pump suppression and a minimized heat load are crucial. While the demonstration of induced squeezing can be seen as a key element for future concepts of measurement induced nonlinearity, this work focuses more on the general concepts and related technologies.

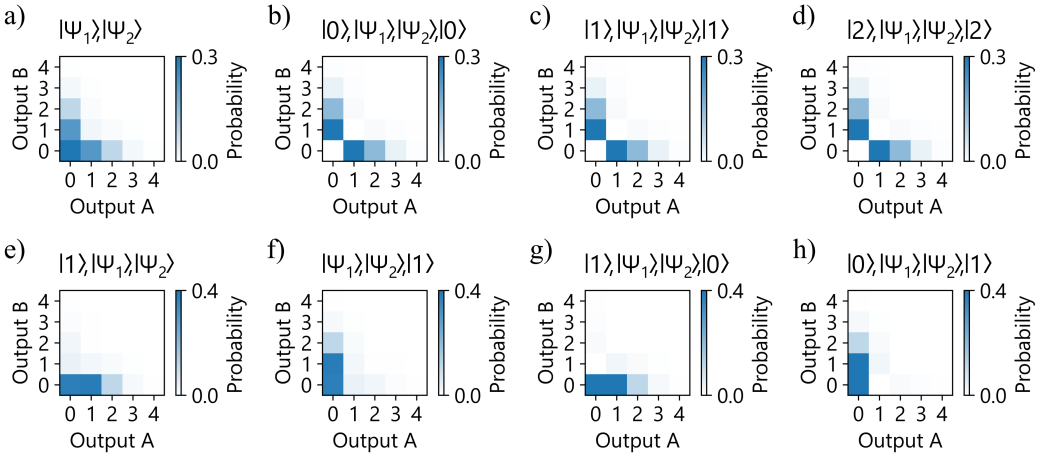

Figure 2.16: Photon-number statistics for a single photon and coherent state of mean photon number $\bar{n}$=1 interfering in *optical circuit A*; a) no measurement at both detectors, b) subtraction of zero photons at both detectors, c) subtraction of one photon at both detectors, d) subtraction of two photons at both detectors, e) and f) subtraction of one photon at one detector and no measurement at the other detector, and g) and h) subtraction of one photon at one detector and zero photons at the other detector.

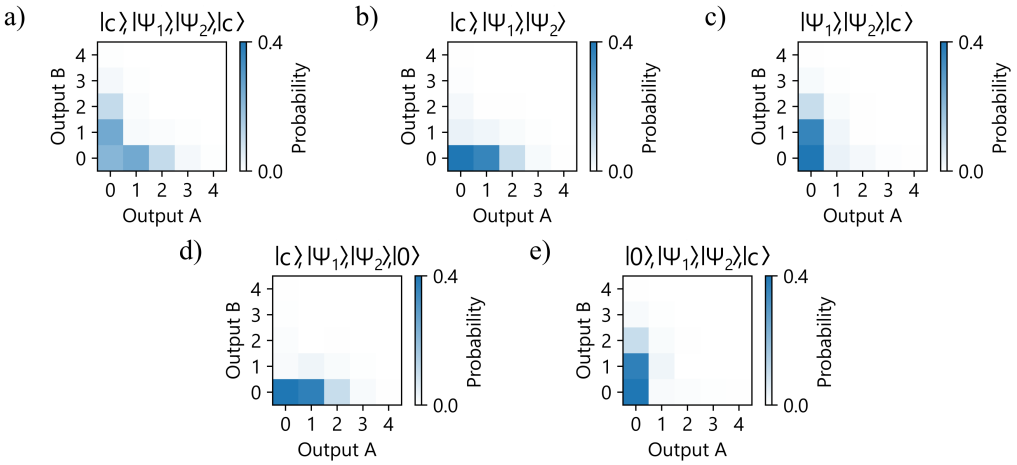

Figure 2.17: Photon-number statistics for a single photon and coherent state of mean photon number $\bar{n}$=1 interfering in *optical circuit A*; a) subtraction of at least one photon at both detectors, b) and c) subtraction of at least one photon at one detectors and no measurement at the other detector, and d) and e) subtraction of at least one photon at one detector and zero photons at the other detector.

2.4.2 Phase-dependent optical circuit

In the last part of this chapter, the previous optical circuit is further expanded. Adding another (fourth) beam splitter before coupling out the two-mode state, as shown in Figure 2.18, results in a Mach-Zehnder geometry.

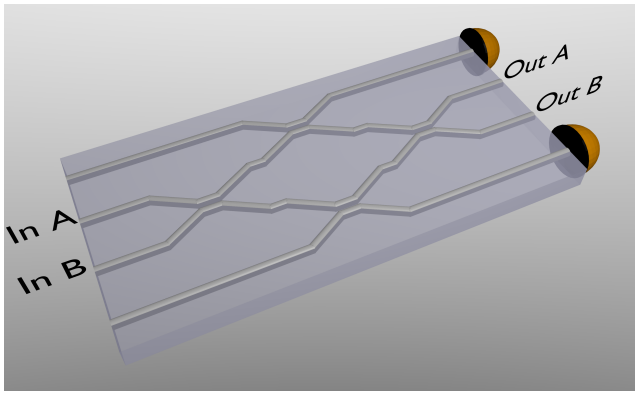

Figure 2.18: Phase-dependent optical circuit to create exotic two-mode quantum states with four beam splitters in a Mach-Zehnder geometry. The two inputs are labeled with In A and In B, while the two modes of the output state are labeled Out A and Out B.

In this optical circuit (in the following called *optical circuit B*), the difference in path length (relative phase shift) within the interferometer design influences the interference outcome when recombining the states. Riabinin et al. investigated theoretically the influence of different beam-splitting ratios as well as phaseshifts inside the Mach-Zehnder structures and theoretically verified the generation of two-mode squeezing [24]. The maximum possible two-mode squeezing equals the value for the earlier discussed single-mode case [21, 24]. Nevertheless, the theoretical investigations here in this work are restricted to photon-number statistics. Also, the presented simulations do not include a difference in path length of the two paths inside the Mach-Zehnder structure. Therefore, a fixed phase relation which influences the photon-number correlations of the two-mode state is experimentally realized with the passive and phase-stable integrated circuit. However, active control over the phase inside the interferometer enables continuous tuning between the maximum squeezed and non-squeezed state.

When we compare the photon-number statistics of the two circuits for no measurement in both detectors (accepting all measurement outcomes), as shown in Figure 2.16 a) and Figure 2.19 a), the influence of the different interferometer structures become visible. For both circuits, the subtraction of either zero, one, or two photons in both arms shows the same results. However, as already shown for the case with no measurement in Figure 2.19 a), the photon-number statistics of the two outputs is not symmetric for *optical circuit B*. In addition, with no loss taken into account, the photon subtraction of the same photon number in both arms guarantees the existence of exactly one photon at one output port, independent of the statistics in the other port, as shown in Figure 2.19 b) - d).

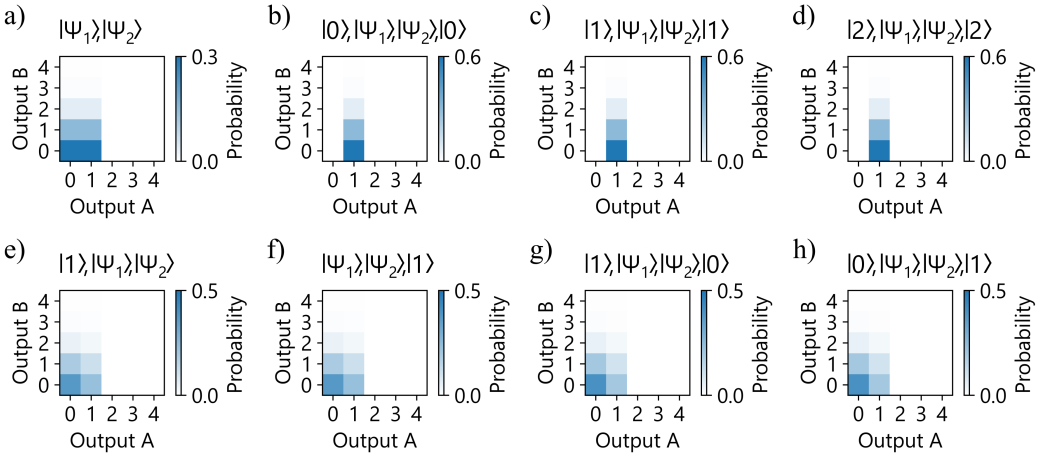

Figure 2.19: Photon-number statistics for a single photon and coherent state of mean photon number $\bar{n}$=1 interfering in *optical circuit B* with no phase difference between the two paths in the interferometer; a) no measurement at both detectors, b) subtraction of zero photons at both detectors, c) subtraction of one photon at both detectors, d) subtraction of two photons at both detectors, e) and f) subtraction of one photon at one detector and no measurement at the other detector, and g) and h) subtraction of one photon at one detector and zero photons at the other detector.

For a photon subtraction in only one arm, it makes no difference at which detector the photon is subtracted, as the fourth beam splitter has a 50:50 beam-splitting ratio. Furthermore, for the interference of a coherent state with mean photon number one and a single photon, the resulting photon-number statistics are similar for the subtraction of one photon at one detector and either no measurement at the other detector, or a zero-photon measurement at the other detector, as shown in Figure 2.19 e) - h).

Following the investigations in the previous section, the subtraction of at least one photon using click detectors is investigated. Here, the measurement in both arms or one arm and no measurement, or a zero-photon measurement at the other detector are shown in Figure 2.20. Again the findings in Figure 2.19 e)-h) for photon-number resolving detectors are very similar compared to the findings in Figure 2.20 b)-e).

It can be seen that it is possible to create complex correlations in the photon numbers of the two output states with both circuits. Based on a parameter optimization by Matvei Riabinin, the maximum two-mode squeezing, based on a measurement in the outer detectors can be achieved for a beam-splitting ratio of 1:0 for the fourth beam splitter in *optical circuit B*, which directly corresponds to *optical circuit A*. While the main focus therefore lies on the latter, both optical circuits are experimentally investigated to also explore the critical phase stability for the interferometric design. In Chapter 4 we discuss the experimental realization of these circuits, followed by first experiments using these components in Chapter 5. All in all, the combination of coherent states, single-photon states and measurement operations are a promising tool to create interesting multi-mode quantum states with

complex correlations in the joint photon-number basis.

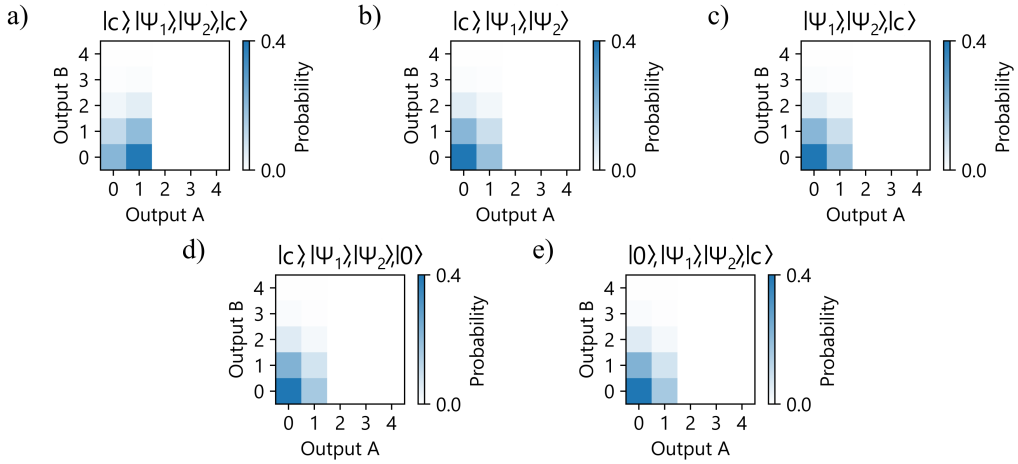

Figure 2.20: Photon-number statistics for a single photon and coherent state of mean photon number $\bar{n}$=1 interfering in *optical circuit B* with no phase difference between the two paths in the interferometer; a) subtraction of at least one photon at both detectors, b) and c) subtraction of at least one photon at one detectors and no measurement at the other detector, and d) and e) subtraction of at least one photon at one detector and zero photons at the other detector.

Source characterization 3

When observing quantum-interference phenomena, whether or not measurement-induced effects are investigated, indistinguishability between photons is crucial. In this chapter, the optical setup for experimentally creating the different input states for interference experiments, namely coherent light and single photons, is introduced. Furthermore, the created output states of this source are characterized.

3.1 Input state setup

In this section, we introduce the setup for creating single photons based on SPDC as well as coherent states. As discussed previously, these states can be differentiated in the photon-number basis. However, if one wants to use multiple states at once and investigate interference phenomena between the different states, maximum mode overlap must be ensured, which is not included in the photon-number basis. Especially for the spectral mode, the single-photon purity and therefore an uncorrelated JSI of an SPDC single photon source is important. In addition, the usage of only one input laser avoids a difficult synchronization between two systems. The setup to create coherent states and single photon Fock states is shown in a simplified schematic in Figure 3.1 and in a full overview in Figure 3.2.

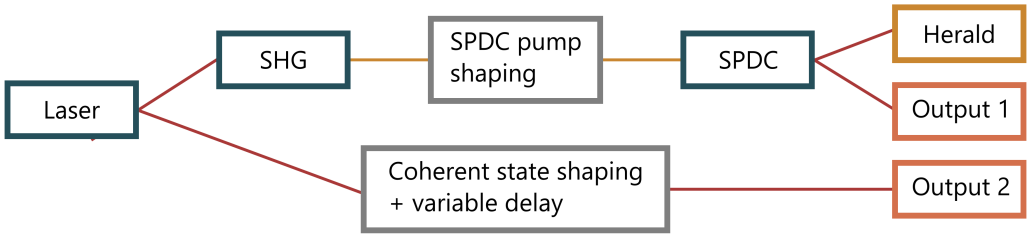

Figure 3.1: Simplified schematic of the experimental setup for creating various input states as described in the main text with colored boxes based on the illustration in Figure 1.1. The connecting lines represent a laser beam with red corresponding to 1550 nm wavelength and yellow corresponding to 775 nm wavelength. The wavelength conversion is caused by second harmonic generation (SHG) and spontaneous parametric down-conversion (SPDC). The orange boxes represent the two output states, which can then be used as the actual input states for later experiments.

In the simplified schematic in Figure 3.1, the optical path starts with a pulsed 1550 nm laser. The laser is partially used as a pump for a second harmonic generation (SHG) process in a

nonlinear crystal, resulting in a laser beam at half the wavelength. We shape this beam in the frequency domain and pump a second nonlinear crystal for SPDC. Using a type-II SPDC process, where signal and idler photons are in orthogonal polarization modes, they can be separated deterministically. Without heralding, the photon statistics in Output 1 ideally follow a thermal distribution. With heralding exactly one photon, Output 1 equals a one-photon Fock state. In the low pump-power regime, heralding with a click detector also approximates a one-photon Fock state in the signal arm, as discussed Section 2.2. The non-converted part of the input laser is also shaped in frequency to match the frequency properties of Output 1. Assuming bandwidth-limited (Fourier-transform limited) pulses, the spectral shaping also causes temporal shaping. A variable delay line (VDL) enables control of the arrival time of Output 2 in comparison to Output 1.

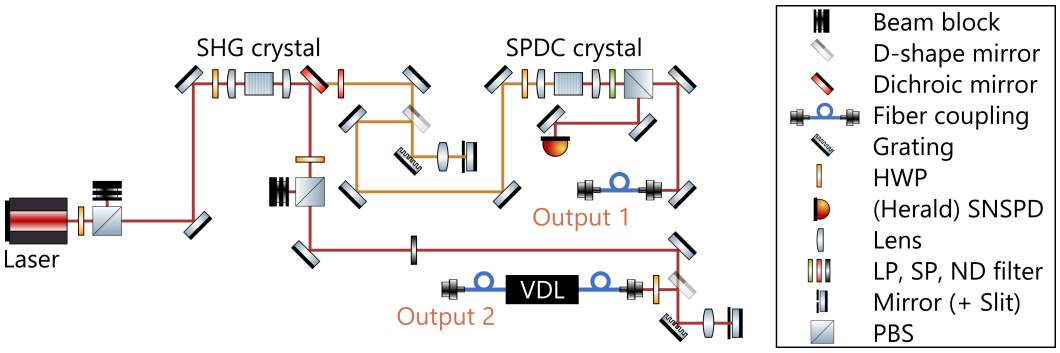

Figure 3.2: Experimental setup for creating various input states as described in the main text. The wavelength conversion is caused by second harmonic generation (SHG) and spontaneous parametric down-conversion (SPDC). The arrival time of photons at Output 2 is controlled by a variable delay line (VDL). Component drawings are partially taken from Reference [37].

The more complex illustration of the experimental setup for creating the input states for the later experiments is shown in Figure 3.2 and is explained in analogy to the simplified schematic in Figure 3.1.

Laser: The optical path starts with a pulsed 1550 nm lasers of which we control the laser power using a half wave plate (HWP) followed by a polarizing beam splitter (PBS) with a beam block in one output.
SHG: We create 775 nm light in a nonlinear bulk periodically poled Mg:$LiNbO_3$ crystal in which the beam is focused. With a surrounding oven, the phase-matching can be temperature controlled. A half wave plate in front of the crystal is used to optimize the input polarization of the 1550 nm light for maximum frequency conversion.
Coherent state shaping + variable delay: After the SHG process, remaining 1550 nm light is separated using a dichroic mirror, attenuated using a second set of HWP, PBS, and beam block, a neutral density (ND) filter, and send to a 4f-line for spectral shaping. In theory, a 4f-line consists of two gratings and a slit standing in the focal plane of two lenses. Practically, we simplified this construction using a mirror after the slit, reducing the resources to one grating and one lens. After a D-shape mirror, the polarization of the

resulting light beam is adjusted using one more half wave plate.
Output 2: We couple the light to optical fiber, and send it through a fiber-connected polarization-maintaining variable delay line. Its fiber-output corresponds to Output 2 in Figure 3.1.
SPDC pump shaping: For the transmitted 775 nm path of the dichroic mirror, the beam is further filtered using a short pass (SP) filter and also undergoes the spectral filtering in a 4f-line optimized for 775 nm wavelength.
SPDC: The resulting beam acts as a pump beam for an SPDC process in a periodically poled KTP crystal which is again surrounded by lenses and a HWP for brightness optimization and a long pass (LP) filter to remove the pump beam after the crystal. The resulting 1550 nm photon pairs with orthogonal polarization are split on a PBS and fiber-coupled.
Herald and Output 1: We send one fiber to a superconducting nanowire single-photon detector (SNSPD) for herald detection, while the other path corresponds to the other output for new created input states for later experiments. This port it labeled Output 1.

The device names for the main components are highlighted in Appendix Table A.1. The usage of a "*common master laser*" provides a stable phase relation between the output ports [36] (p. 86). Similar schemes are used for (weak-field) homodyne detection [38] or for "*measuring the joint spectral mode of photon pairs using intensity interferometry*" [39].

Ideally, the phase-matching function (see Section 2.2) directly matches the second harmonic pump light, such that the created SPDC signal photons have the same spectral and temporal profile as the initial pump laser. This can only be achieved for a pure, degenerate SPDC source. At 1550 nm wavelength, such a source can be realized with a KTP crystal [40]. Deviations from a degenerate source, mainly resulting from fabrication imperfections of the periodically poled source crystal, can partially be compensated using the 4f-lines. With these, it is possible to fine-tune the central wavelength as well as the bandwidth. For more flexibility, a wavelength-tunable laser system is preferable. Additional filtering of signal and idler photons can improve the purity [40] but either induces loss when filtering the signal output or induces noise when filtering the idler output.

For an ideal system, the laser pulse repetition rate must match the recovery time of the utilized detectors (the recovery time is explained in Section 6.1). If this is not the case, not every new laser pulse can be interpreted as an equal repetition of the experiment as fully recovered detectors are one element of the initial conditions. In a first approximation, a mismatch between the recovery time and laser repetition rate can be interpreted as a reduced detection efficiency and therefore an additional loss source.

For the presented work in this thesis, two laser systems were available. For a first comparison, the datasheets for the laser systems are shown side-to-side in Appendix Table A.2. Both lasers do not provide a tunable central wavelength. Therefore the poling period of the nonlinear crystals must directly fit to this wavelength. The NKT Photonics Origami laser's repetition rate is two orders of magnitude higher than the Calmar Cazadero FLCPA laser's repetition rate and therefore does not fit the detector's recovery time. Unfortunately, due to a broken *dispersion control*-knob of the Cazadero laser, this laser does not provide bandwidth-limited pulses, a disturbed wavelength spectrum, and clipped spatial profile.

While it is still possible to use the system to pump an SPDC source, it cannot be used as a reliable source for single-photon interference. Therefore, we use the Origami laser for further experiments, while the characterization of a single-photon source using the Cazadero laser can be found in Appendix A.6.

3.2 Coherent state characterization

After introducing the experimental setup for creating different input states, the optical properties of the two output-arms of this part of the experiment must be characterized to ensure maximum indistinguishability. At first, the created coherent states are investigated.

Figure 3.3 shows the optical spectra of the pump laser, measured with a commercial optical spectrum analyzer. It can be seen that the laser provides a clean spectrum. The spectral bandwidth of 13.8 nm also agrees with the temporal pulse length from the datasheet, suggesting a bandwidth-limited laser. Therefore, the pump laser is expected to be well suited for interference experiments based on the optical spectrum.

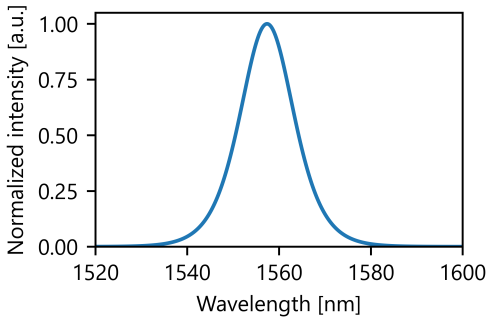

Figure 3.3: Optical spectrum of the Origami laser measured with an optical spectrum analyzer.

Due to their slow recovery time, the later used superconducting detectors cannot detect more than $2 \cdot 10^6$ occupied pulses per second when using laser repetition rates faster than the detector recovery time. As mentioned in Section 3.1, this mismatch induces loss. In addition, the combination of a too high repetition rate and high mean photon number (more than $2 \cdot 10^6$ occupied pulses per second) causes the superconducting detector to stay in a fully resistive, non-functional state after photon absorption (latching).

Therefore, it is not possible to measure a mean photon number of one with the combination of the Origami laser and utilized superconducting detectors. This would correspond to on average $50.6 \cdot 10^6$ pulses per second occupied by at least one photon, based on Poisson statistics. For the experimentally identified limit of $2 \cdot 10^6$ occupied pulses per second, a pulsed laser with 79.9 MHz repetition rate has to be attenuated down to a mean photon number of 0.025 photons per pulse. As we saw at the end of the previous chapter, measurement-induced nonlinearities are especially interesting at high photon numbers.

Therefore, the required attenuation is disadvantageous. However, the discussed mismatch between the laser repetition rate and detector recovery time affects the detected photons at the outputs not the interacting photons itself. This means that imperfections and photon loss after interference makes it possible to use higher mean photon numbers. On the other hand, additional loss lowers the interference visibility.

Furthermore, we must investigate, whether the laser system follows the photon-number statistics for a coherent state, introduced in Chapter 2. As measuring the full photon-number distribution of the output is demanding due to the lack of suitable photon-number resolving detectors, the second-order autocorrelation function, sometimes called second-order Glauber function $g^{(2)}(\Delta t)$, is introduced [41]. For classical fields, the second-order autocorrelation function describes the relation of a lightfield with intensity I at a certain time t and a different point in time $t + \Delta t$ as (Reference [8] (p. 128))

$$g^{(2)}(\Delta t) = \frac{\langle I(t)I(t+\Delta t)\rangle.}{\langle I(t)\rangle^2}. \tag{3.1}$$

Here, $g^{(2)}(\Delta t = 0)$ is lower bounded by one. This limitation does not hold for quantum light. Therefore, $g^{(2)}(\Delta t = 0) \leq 1$ can be seen as an indication for non-classical light. For coherent light, a $g^{(2)}(0)$-value of one is expected. Deviations upwards from this number point towards a mixed and therefore non-pure state. While a coherent state provides a $g^{(2)}(0)$-value of one, the latter does not automatically imply a coherent state. Nevertheless, the second-order autocorrelation function is an important indicator for state classification.

For pulsed lasers, the second-order autocorrelation function with the same pulse (not its nearest subsequent neighbors) $g^{(2)}[0]$ can be written as (Reference [12] (p. 34))

$$g^{(2)}[0] = \frac{\langle \hat{n}(\hat{n}-1)\rangle}{\langle \hat{n}\rangle^2}. \tag{3.2}$$

This equation can be rewritten in terms of the mean photon number $\bar{n}$ and the variance $(\Delta\bar{n})^2 = \langle \hat{n}^2\rangle - \langle \hat{n}\rangle^2$ as (Reference [12] (p. 43))

$$g^{(2)}[0] = 1 + \frac{(\Delta\bar{n})^2 - \bar{n}}{\bar{n}^2}. \tag{3.3}$$

For Poissonain light and therefore coherent states, it holds that $(\Delta\bar{n})^2 = \bar{n}$ and with it $g^{(2)}[0] = 1$.

When investigating the second-order autocorrelation function in the low photon-number regime, at least two click detectors are needed. When splitting the optical signal at a 50:50 beam splitter, the probability of measuring a signal (measuring at least one photon) on both detectors at the same time $p(\mathrm{Det}_1, \mathrm{Det}_2)$ can be compared to the probability of measuring a signal at each detector individually $p(\mathrm{Det}_i)$. For pulsed lasers, each probability equals to the number of detection events (counts) in an acquisition time C_i, divided by the number of laser pulses in that time R. Therefore, the second-order autocorrelation function transforms

to

$$g^{(2)}[0] = \frac{p(\mathrm{Det}_1, \mathrm{Det}_2)}{p(\mathrm{Det}_1)p(\mathrm{Det}_2)} = \frac{C_{\mathrm{Det}_1,\mathrm{Det}_2} R}{C_{\mathrm{Det}_1} C_{\mathrm{Det}_2}}. \tag{3.4}$$

The number of pulses R is measured using a photodiode installed in transmission of the dichroic mirror in Figure 3.2. We measure the different countrates of the two click detectors using a fiber-coupled 50:50 beam splitter, followed by two commercial high-efficient superconducting nanowire single-photon detectors. Both detectors and a laser-synchronized time reference are electrically connected to a streaming time-to-digital converter (time tagger). The results for the second-order autocorrelation measurement are shown in Table 3.1. It can be seen that the laser provides a $g^{(2)}[0]$-value of almost one for a coherent state.

Table 3.1: Measurement results for the second-order autocorrelation function $g^{(2)}[0]$ and contained laser and detection rates for the Origami laser.

R [1/s]	79895302 ± 2
C_{Det1} [1/s]	410700 ± 700
C_{Det2} [1/s]	423500 ± 700
$C_{\mathrm{Det1,Det2}}$ [1/s]	2210 ± 50
$g^{(2)}[0]$	1.015 ± 0.023

To summarize, with no spectral filtering, Output 2 in Figure 3.1 and 3.2 has a bandwidth-limited spectrum centered at 1557.4 nm with a spectral bandwidth of 13.8 nm. Based on a second-order autocorrelation measurement, we infer that the output is a coherent state. The linear polarization of the output is given by the PBS that is also used to control the mean photon number and the HWP in front of the fiber coupling. We adjust the HWP such that the light polarization direction matches the slow axis of the polarization-maintaining fiber for incoupling with which also the spatial mode is set.

3.3 Single-photon state characterization

To interfere a single photon with the characterized coherent state on a beam splitter, they must overlap in all degrees of freedom. In addition, for repeatable measurements, all created single photons should have the same properties. Those properties can be tackled by quantum source engineering. For SPDC sources, one has access to several techniques to tailor the single-photon source, such as the pump spectrum, crystal material, crystal length, temperature, and poling period as discussed in Section 2.2. In the following subsections, the different components for single-photon source engineering are introduced and the setup source is further characterized.

3.3.1 Pump spectrum

With an oven around the periodically poled Mg:$LiNbO_3$ crystal, it is possible to optimize the brightness of the second harmonic generation. The corresponding spectrum of the second harmonic signal is shown in Figure 3.4. With this spectrum, we pump the spontaneous parametric down-conversion process.

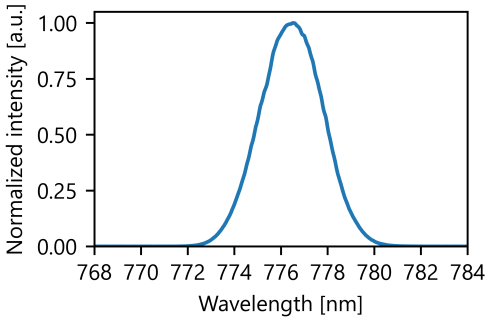

Figure 3.4: Optical spectrum of the SHG signals using the Origami laser, measured with an optical spectrum analyzer.

3.3.2 Joint spectral intensity

SPDC processes always cause some frequency conversion. This is contrary to second-harmonic generation, where frequency conversion due to energy and momentum conservation only occurs for certain wavelength combinations and no frequency conversion is observed for other wavelength combinations. However, as shown with the photon-number statistics of two-mode squeezed vacuum in Section 2.2, most of the light is not converted. Vacuum fluctuations in the non-classical process mean that one can always find a pair of photons fulfilling energy and momentum conservation. Nevertheless, for interference experiments, the created photons must have specific properties like the desired central wavelength and spectral bandwidth.

To investigate the joint spectral intensity (see Section 2.2) experimentally, the SPDC crystal (bulk periodically poled KTP) is pumped with the frequency-converted Origami laser. The created signal and idler photons are both coupled to fibers. Instead of the Herald SNSPD in Figure 3.2, the herald output and Output 1 are sent to two identical scanning-grating single-photon spectrometers, as shown in Reference [42]. By varying the angle between the incoming light and a blaze grating, a wide wavelength range can be scanned. As investigated by Nina Lange, influences of unwanted wavelength-dependent coupling efficiencies of reflective collimators and wavelength-dependent misalignment of the motorized movable grating can be neglected. The spectrometer resolution is given by the collimator's numerical aperture and distance between the blaze grating and output collimator, while a

resolution limit based on the motor resolution can be neglected. We execute a wavelength-characterization scan of both identically set-up spectrometers using a wavelength-tunable narrowband continuous-wave laser (Yenista Tunics T100S-HP/SCL with ± 20 pm wavelength accuracy). The results are shown in Figure 3.5. From the measurement data, we calculate a full-width-at-half-maximum (FWHM) of 1.1 nm for one and 1.4 nm for the other spectrometer.

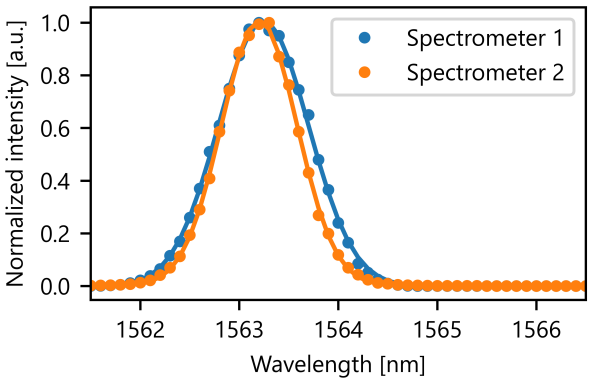

Figure 3.5: Normalized measured intensity over the wavelength of a wavelength-tunable narrowband continuous-wave laser for both identically set-up spectrometers at a wavelength of 1563.2 nm.

By investigating the simultaneous (coincidence) detection events of signal and idler photons over different wavelength combinations, set with the motorized movable gratings, we measure the full JSI. The measurement results are found in Figure 3.6. The marginal spectra on the right are based on a horizontal or vertical integration of the measured data.

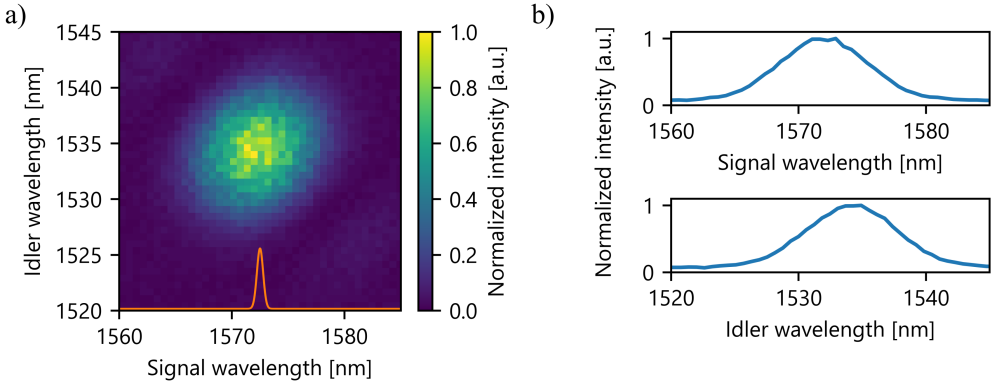

Figure 3.6: a) Joint spectral intensity measurement pumping the KTP crystal with the frequency-converted Origami laser and b) marginal spectra based on the horizontal or vertical integration of the JSI. The orange line corresponds to the narrowband filter later applied to the signal spectrum.

Due to the fixed poling period and fixed central wavelength of the laser, it is not possible to create spectrally degenerate photon pairs. These photons would not just have an equal spectrum for signal and idler wavelength, but would also match the initial spectrum of the coherent state. With the measured signal spectra, the photons of the different input states would barely interfere. While this can be solved with a new nonlinear crystal with a different poling period or a tunable laser system, it can also be solved with additional spectral filters. This solution provides the possibility to carefully match the spectra of the different states but also induces loss.

As the JSI shows no spectral correlations between signal and idler photons, filtering the idler photons and therefore only heralding on a specific wavelength range does not change the signal spectrum. When filtering the coherent state with the 4f-line, induced loss can be compensated with higher laser power. Here, the filtering has no negative effect on the state's purity. Due to the large mismatch between the signal spectrum and coherent state spectrum, wideband filtering the coherent state to match the signal spectrum would drastically reduce the interference visibility between the two outputs. Therefore, we use narrowband filtering of both outputs to match the spectral profiles of both states. This filtering can be realized by repurposing the scanning-grating single-photon spectrometers as fiber-coupled filters at the outputs. When adjusting both scanning-grating single-photon spectrometers to the same wavelength, as already shown in Figure 3.5, they can be used as two almost identical bandpass filters with 92 % overlap. Therefore, for the later interference of a coherent state and a single photon, both filters are set to match the SPDC signal wavelength (where the JSI has its maximum), as seen in Figure 3.6. Unfortunately, this option induces loss at the single-photon output which is further investigated in Section 3.3.3.

Another option is the usage of a spectrally correlated SPDC source. With a spectrally correlated source, the spectra of the coherent state and signal output can be matched without an additional filter in the signal arm. Instead, a filter is placed in the idler arm. Post-selecting on a detection of a filtered idler photon, the central wavelength of the signal photons is constrained. Using a narrowband filter (the scanning-grating single-photon spectrometer), further spectral correlations between the filtered idler photons and signal photons can be minimized. This option does not induce loss in the single-photon output and is therefore generally advantageous. However, as the signal photons are only filtered in post-processing (restricting the measurement results to a coincidence detection with herald photons), the single-photon detectors predominantly detect later discarded detection events. Due to the earlier mentioned mismatch between the laser repetition rate and detector recovery time, this effect drastically lowers the detection efficiency. Therefore, the results presented in this work are restricted to the first option (narrowband filtering) for matching the single-photon output and coherent state output.

3.3.3 Heralding efficiency

Up to now, we did not include the influence of loss. Because of that, it was assumed that the detection of an idler photon heralds and therefore guarantees having a signal

photon at the output port of the source setup. However, due to imperfections of optical components, misalignment, and filtering, the detection of an idler photon only heralds a signal photon with a certain probability, called the heralding or Klyshko efficiency η_s. In the low pump-power regime, the probability of detecting a photon in each arm is given by

$$p_s = p_{SPDC}\eta_s\eta_{Det\ s}, \tag{3.5}$$

$$p_i = p_{SPDC}\eta_i\eta_{Det\ i}. \tag{3.6}$$

Here, p_{SPDC} is the probability of creating a photon pair in one laser pulse and $\eta_{Det\ s}$ or $\eta_{Det\ i}$ accounts for the non-unity detection efficiency, when investigating the single photons. In addition, the probability of the simultaneous detection of a photon in each arm p_{cc} is given by

$$p_{cc} = p_{SPDC}\eta_s\eta_{Det\ s}\eta_i\eta_{Det\ i}. \tag{3.7}$$

From this together with Equation (3.6), the heralding efficiency can be calculated as

$$\eta_s = \frac{p_{cc}}{p_i\eta_{Det\ s}}. \tag{3.8}$$

We execute the corresponding measurement with and without the scanning-grating single-photon spectrometer used as a bandpass filter. The results are shown in Table 3.2. As mentioned in Section 2.2, heralding on at least one photon (instead of exactly one photon) is only an estimation of a single-photon source. Therefore, the creation probability and (in the following section) the second-order autocorrelation function are investigated. Commonly, the generation probability is set (by adjusting the pump power for the SPDC process) to be upper limited by 0.1. The generation probability can be calculated from the measured data in Table 3.2 using

$$p_{SPDC} = \frac{p_s}{\eta_s\eta_{Det\ s}} \leq 0.1 \tag{3.9}$$

As can be seen from the data in Table 3.2, the calculated generation probability is low, while the laser power was already maximized (7.15 mW pump power at 775 nm wavelength for the SPDC process). With no filtering, we achieve a heralding efficiency of 33.9 % ± 1.7 %. The deviation from 100 % is mainly caused by loss at the KTP crystal endface (conchoidal fractures) in combination with imperfections in the setup alignment (fiber-coupling alignment and non-Gaussian spatial mode after 4f-line). Furthermore, imperfections in the optical elements, such as photon loss at fiber-connections are included. Assuming 3 % loss per fiber connector (two connectors were used) and 8 % loss due to reflection at the (uncoated) crystal endface, the maximum achievable Klyshko efficiency reduces to 87 %. A resulting coupling efficiency of 39 % is considered realistic.

When we use the scanning-grating single-photon spectrometer as a bandpass filter, 50 % loss is induced due to loss at the blaze grating in addition to the intrinsic spectral selectivity.

With an ideal poling period and therefore matching wavelengths of signal and coherent state photons, no additional filtering is needed as explained in Section 3.3.2. For the later experiments however, the additional filtering improves the interference visibility as no interference effects were visible without additional filtering, whereas we reached an interference visibility of 36 % with filtering (see Chapter 5).

Table 3.2: Measurement results for the heralding efficiency for the Origami laser with and without the bandpass filter in the signal arm. The count and repetition rate are shown in 1/s, while the actual measurement was executed for 30 s. The shown detection efficiencies are based on an independent detection-efficiency characterization.

	No filter	Signal filter
R [1/s]	79895302 ± 1	79895302 ± 1
$\eta_{\text{Det s}}$	0.80 ± 0.04	0.80 ± 0.04
$\eta_{\text{Det h}}$	0.83 ± 0.04	0.83 ± 0.04
$C_{\text{s}}[1/s]$	92360 ± 60	5852 ± 14
$C_{\text{h}}[1/s]$	85350 ± 60	85430 ± 60
$C_{\text{s,h}}$ [1/s]	18606 ± 25	1194 ± 7
p_{s}	$1.156 \cdot 10^{-3}$ ± (0.07 %)	$7.325 \cdot 10^{-5}$ ± (0.24 %)
p_{h}	$1.068 \cdot 10^{-3}$ ± (0.07 %)	$1.069 \cdot 10^{-3}$ ± (0.07 %)
p_{cc}	$2.329 \cdot 10^{-4}$ ± (0.14 %)	$1.494 \cdot 10^{-5}$ ± (0.6 %)
$\eta_{\text{s}}\eta_{\text{Det s}}$ [%]	21.80 ± 0.04	1.398 ± 0.008
η_{s} [%]	27.2 ± 1.4	1.75 ± 0.08
p_{SPDC}	0.00530 ± 0.00001	0.00524 ± 0.00003

3.3.4 Single-photon second-order autocorrelation measurements

Similar to the characterization of the coherent state, we investigate the second-order autocorrelation function. For this, the signal arm is split using a 50:50 beam splitter, and both ports together with the herald arm are connected to three superconducting nanowire single-photon detectors. For an ideal spontaneous parametric down-conversion source, the $g_u^{(2)}[0]$-value of the signal photons with no heralding should equal two, as this would correspond to a perfectly mixed (thermal) state. In contrast, for a perfect single-photon source, the $g_h^{(2)}[0]$-value should be zero, implying that only one and never two photons are found in one pulse. As mentioned in Section 3.2, $g^{(2)}[0] \leq 1$ corresponds to nonclassical light. For the experimental setup, an unheralded $g_u^{(2)}[0]$-value of two and a heralded

$g_h^{(2)}[0]$-value close to zero are desirable. In addition, the number of spectral (Schmidt) modes K, mentioned in Section 2.2, can be calculated from the unheralded $g_u^{(2)}[0]$-value as (Reference [43])

$$K = \frac{1}{g_u^{(2)}[0] - 1}. \tag{3.10}$$

For the unheralded second-order autocorrelation function, we use Equation (3.4). For the heralded second-order autocorrelation function, one must postselect only on events when there was a herald photon. Therefore, Equation (3.4) transforms to (Reference [44])

$$g_h^{(2)}[0] = \frac{C_{\mathrm{s1,\,s2,\,h}} C_{\mathrm{Det\,h}}}{C_{\mathrm{s1,\,h}} C_{\mathrm{s2,\,h}}}. \tag{3.11}$$

The results for this measurement are presented in Table 3.3. Both $g^{(2)}$-values are independent of the individual detection efficiencies. It can be seen that we almost reached the targeted values for the second-order autocorrelation function at zero time delay. The nonclassical character of both sources, indicated by a heralded $g_h^{(2)}[0]$-value far beyond one, is verified. Furthermore, it can be seen that filtering of signal photons improves the spectral purity and number of Schmidt modes, as the unheralded $g_u^{(2)}[0]$-value approaches two [29].

For following interference experiments in Chapter 5, the low Schmidt number points towards a pure, single-mode single-photon source. The interference visibility should not be limited by hidden spectral correlations. When we interfere this single-photon source with a coherent state, multi-photon events only caused by the single-photon source can be neglected due to the low heralded second-order autocorrelation function.

Table 3.3: Measurement results for the heralded and unheralded second-order autocorrelation function for 100 s for the Origami laser.

C_{s1}	367500 ± 600
C_{s2}	257300 ± 500
C_{h}	19100000 ± 5000
$C_{s1,\,s2}$	22 ± 5
$C_{s1,\,h}$	38000 ± 200
$C_{s2,\,h}$	24570 ± 160
$C_{s1,\,s2,\,h}$	2.0 ± 1.4
$g_u^{(2)}(\Delta t = 0)$	1.9 ± 0.4
K	1.1 ± 0.5
$g_h^{(2)}(\Delta t = 0)$	0.041 ± 0.029

3.4 Source characterization summary

In this chapter, the setup to create coherent states and single photons for interference experiments was introduced and characterized. Based on second-order autocorrelation measurements, the typical characteristics for the two targeted states were fulfilled. As the single-photon source is used for interference experiments in Chapter 5, we also investigated similarities with the characterized coherent state. Due to the nontunable poling period and pump wavelength, the single-photon spectra do not agree with the spectra of the coherent states. Therefore, filtering the single-photon spectrum and coherent-state spectrum becomes essential. The central wavelength of the single photons is still in the range of the coherent-state spectrum. However, in order to match the spectral shapes, additional narrowband filtering is necessary. This additional filtering drastically lowers the heralding efficiency. In future experiments however, a new nonlinear crystal for SPDC or a different laser system, or pulse-picking can compensate the drawbacks.

Passive integrated circuits 4

In this chapter, we introduce the integrated circuits for the experiments to investigate measurement-induced nonlinearities. Two waveguide samples, one for each optical circuit (see Section 2.4.1 and 2.4.2) were fabricated with the help of Maximilian Protte and the Paderborn University IQO technology team led by Christof Eigner.

For the demonstrated proof-of-principle experiment, integration may not be the preferred option based on the number of required integrated components. Interface loss when coupling light into and out of the integrated circuit predominates the advantages of integrated optics (see Section 4.1). However, considering a further expansion and extended complexity of the schemes for measurement-induced nonlinearities, it is important to show the usage of integrated optics in this context. In addition, Chapter 6 shows a simplification of the optical circuit when integrating more devices, namely the single-photon detectors.

This chapter focuses on the characterization of integrated routing structures and multi-channel interfacing. In the first section, the waveguiding platform and its characterization methods are introduced. The second section continues with more complex integrated routing structures. Section 4.3 explains the technology for efficient packaging and interfacing of multi-channel fibers and waveguides. Section 4.4 summarizes the characterization of the two devices which we use for the quantum optics experiments in the next chapter.

4.1 Titanium in-diffused waveguides in lithium niobate

Integrated optics has proven to be a great solution for complex, compact and low-loss circuits [25]. The complexity is enabled by exploiting different material properties, starting from basic features as temperature stability, up to electrooptic effects, and optical nonlinearities, where a strong spatial mode confinement usually achieved in integrated circuits results in high-efficient components [26]. On a lot of different integration platforms, optical toolboxes have been developed with which complete optical tables can be replaced [25]. The already mentioned strong spatial mode confinement in optical waveguides together with the progress in fabrication technologies enables incomparable scalability. In only a few fabrication steps, several components can be fabricated at once on a small footprint. With this, the complexity of the circuits can be enhanced and the requirements on the surrounding environment are far less restricted, such that optical circuits can be installed in a cryogenic environment. Last but not least, huge effort is put into improvement of fabrication technologies and optimization of circuit designs to minimize loss. Compared to freespace optics, loss at interfaces between different components in the circuit and misalignment or instabilities are diminished.

In this work, we use titanium in-diffused waveguides in lithium niobate as a basis for integrated circuits. When classifying integration platforms, they can be divided into the groups of nanophotonics and microphotonics, or platforms for passive and active components. In the former classification, silicon-on-insulator and silicon nitride waveguides are common examples for nanophotonic materials [25]. They provide high component densities and rely on highly sophisticated fabrication processes. Nevertheless, due to the structure sizes (typically in the wavelength range), coupling light into or out of a circuit requires the usage of additional wavelength selective grating couplers, mode converters, or alignment-sensitive lenses. On the other hand, microphotonics (for example UV-written waveguides in silica and titanium in-diffused waveguides in lithium niobate) provide lower component densities but easier coupling methods, as shown in Section 4.3. While the optical circuits from Section 2.4 do not contain active components which can manipulate the light depending on an electric signal, a future integration of an active phase-shifter and variable beam splitter can provide further possibilities.

To summarize, a microphotonics platform can provide easier outcoupling of quantum states which is important when using the created two-mode quantum states from the optical circuits in further off-chip experiments. In addition, an active material gives the possibility to enhance the complexity of the circuits. Therefore, titanium in-diffused lithium niobate was chosen as it is an active, microphotonic integration platform.

In addition, titanium in-diffused lithium niobate waveguides are cryo-compatible [45–48]. Therefore, all passive and active integrated devices can be operated at cryogenic temperatures suited for superconducting detectors. The integration of these detectors is discussed in Chapter 6. The cryo-compatibility of a 50:50 beam splitter, one of the essential components for the demonstrated scheme for measurement-induced nonlinearity is shown in Figure 4.1. Here, we investigated the beam-splitting ratio of an integrated directional coupler (see Section 4.2) during a cooldown to 0.8 K. It can be seen that the beam-splitting ratio is independent of the surrounding temperature since relative changes between the two waveguides forming the coupler are negligible. Fluctuations in the beam-splitting ratio can be fully attributed to changes in the outcoupling efficiency to fiber-coupled powermeters independent of the integrated directional coupler.

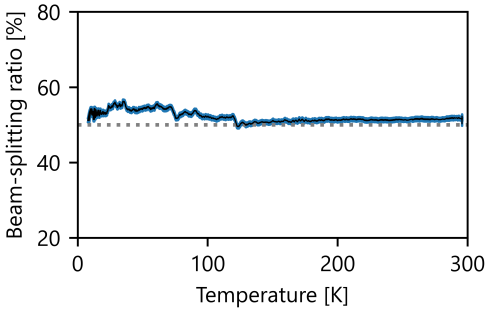

Figure 4.1: Beam-splitting ratio of an integrated large-gap directional coupler on a fiber-coupled lithium niobate sample during a cooldown from room temperature to 0.8 K in a helium sorption cryostat. The blue error bands show temporal fluctuations for the two power-meters at the two outputs. The dotted line illustrate the targeted 50:50 beam-splitting ratio.

4.1.1 Waveguide fabrication

For a better overview over the material platform, this section describes the fabrication process of the utilized waveguides. It starts with a 0.5 mm thick, diced sample of congruently grown z-cut lithium niobate, as shown in Figure 4.2 (Step 1), on which an 80 nm high titanium layer is deposited (Step 2). Next an optical photoresist is deposited via spin coating (Step 3). Using a direct laser-lithography system, the photoresist is structured (Step 4). After a post-exposure bake, the photoresist is developed (Step 5). The design is imprinted onto the titanium layer in a wet-etching process (Step 6). After etching, the residual photoresist is removed (Step 7). The structured titanium layer is then in-diffused into the lithium niobate by placing the sample in an oven at 1060 °C for 9 h, resulting in optical waveguide structures (Step 8). Afterwards the endfaces of the sample are polished to optimize coupling.

As lithium niobate is an electrooptic and nonlinear material, the refractive index of the material can be changed with an applied electric field [49]. In addition, nonlinear changes of the optical fields, as for example sum-frequency generation, can be achieved under fulfilled phase-matching conditions. In z-cut lithium niobate, quasi-phase-matching using periodic poling can be realized by periodic inversion of the crystal domains. For active electrooptic devices, additional conductive structures, usually made of chrome or gold, are deposited by sputtering and subsequent structuring in further lithography steps. With these fabrication techniques, a whole optical toolbox, comprising of straight or curved waveguides, beam splitters, phaseshifters, polarization modulators, active switches, and frequency converters has been developed for titanium in-diffused lithium niobate waveguides [49]. While active components can be included in future extensions of the presented scheme, the two 8 cm long waveguide samples for the passive optical circuits, depicted in Figure 2.15 and 2.18, were fabricated following the steps above.

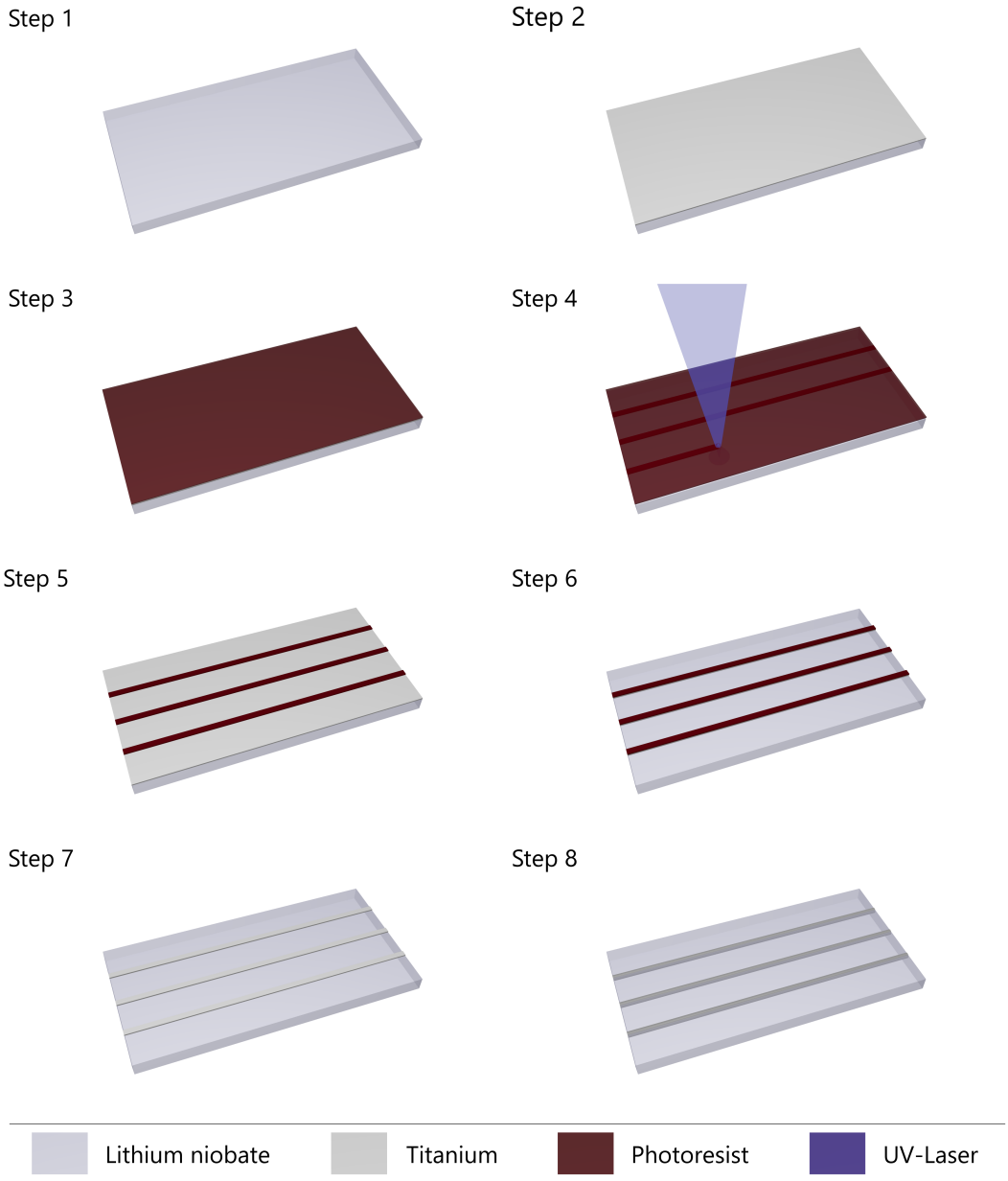

Figure 4.2: Fabrication of Ti:$LiNbO_3$ waveguides. The individual steps are explained in the main text.

The waveguiding itself is caused by a positive refractive index change due to the titanium in-diffusion. Despite lithium niobate's birefringence, the relative change is almost similar for both refractive indices n_o and n_e. For the fabricated waveguides for the later interference experiments a titanium stripe width of 7 µm and height of 80 nm is used. Here, single-mode waveguiding is achieved at 1550 nm wavelength for both crystal orientations. With the sketched waveguide structures in x-propagation on z-cut lithium niobate, two orthogonal polarization modes (transverse-electric (TE) polarization and transverse-magnetic (TM) polarization) are guided and experience two different effective refractive indices due to birefringence. The refractive index distributions and resulting polarization modes for 1550 nm light are shown in Figure 4.3. For the latter, we execute Finite Element Method simulations, using a commercially available mode-solving tool (Synopsis RSoft). The origin of the modeled refractive index distributions as well as more details on the mode simulations are found in Section 6.2.1.

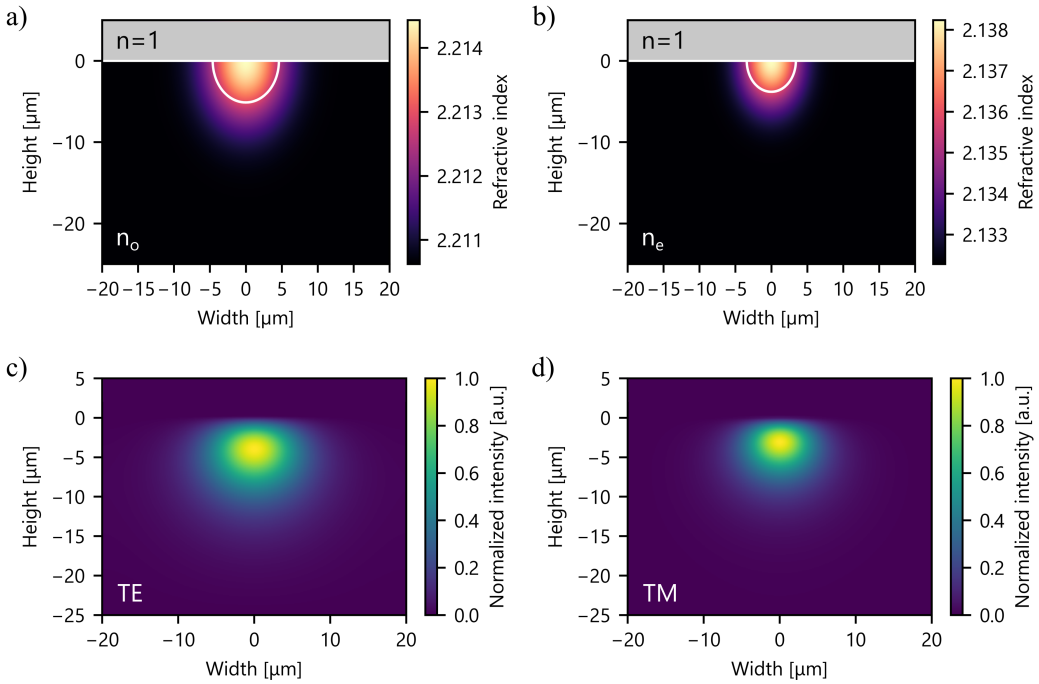

Figure 4.3: Refractive index distribution for titanium in-diffused lithium niobate waveguides using a) the ordinary refractive index of lithium niobate and b) the extraordinary refractive index. Corresponding simulated modes are shown underneath in c) and d). The figure is adapted from Reference [50].

As can be seen in the spatial mode profiles in Figure 4.3 c) and d), the mode size is similar to the initial titanium stripe width in the few micron-range due to the weak confinement resulting from the small refractive index changes. This limits the number of components per integrated circuit. It therefore reduces the complexity and causes restrictions on minimum bending radii with reasonable loss. On the other hand, it lowers the fabrication requirements

for low-loss waveguiding. Due to the small and slow refractive index transition, roughness caused by the optical fabrication can be tolerated. This results in a high fabrication yield for integrated circuits as well as mode-size-matching with standardized single-mode optical fiber (SMF-28) at 1550 nm wavelength.

4.1.2 Waveguide loss characterization

As shown in Section 2.3, photon loss must be minimized for maximal interference visibility. This does not just include loss in the source setup but also the waveguide circuit. To ensure low-loss guiding for the fabricated samples, we deposit straight waveguides for test measurements next to all more complex integrated structures. Even for straight waveguides, a precise and non-destructive loss characterization is generally challenging and often depends on the coupling efficiency to the waveguide. Due to the internal reflections at the two ends of the waveguide after endface polishing, a waveguide loss characterization method from Regener and Sohler based on the measurement of Fabry-Perot resonances is executed [51] . The setup for this non-destructive, polarization-sensitive characterization method is shown in Figure 4.4.

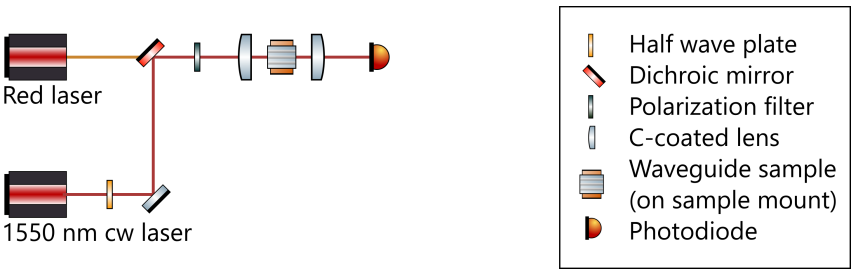

Figure 4.4: Optical setup for waveguide loss characterization based on a scheme by Regener and Sohler [51]. Component drawings are partially taken from Reference [37].

Waveguide coupling is executed with a red alignment laser. For the loss characterization, the red alignment laser is replaced with a narrowband continuous wave (cw) linearly polarized laser at 1550 nm wavelength. Using a half wave plate and a subsequent polarization filter, only horizontally polarized light (corresponding to TE polarization inside the waveguide), or vertically polarized light (corresponding to TM polarization inside the waveguide) is let through. The two polished endfaces of the sample create a low-finesse Fabry-Perot interferometer. Therefore, the waveguide-outcoupled measured laser power I_{out} depends on the initial laser power I_0, effective coupling η_{coupling}, endface transmissivity T and reflectivity R, crystal length L, propagation constant β, and waveguide loss α, as shown in Equation (4.1) based on Reference [51].

$$I_{\text{out}} = \frac{T^2 I_0 \eta_{\text{coupling}} \mathrm{e}^{-\alpha L}}{(1 - R\mathrm{e}^{-\alpha L})^2 + 4\sin^2(\beta L) R\mathrm{e}^{-\alpha L}} \tag{4.1}$$

By changing the sample temperature with the Peltier element, the effective sample length is changed due to thermal contraction and the temperature-dependent refractive index. This results in an interference pattern, when evaluating the output power I_{out} over the sample temperature. For the executed loss measurements, we changed the sample temperature over time with a Peltier-element included in the sample holder. An example is shown in Figure 4.5. Antireflective coatings (c-coatings) on both lenses in Figure 4.4 avoid additional interference patterns between each endface and adjacent lens. The irregularity in the position of the optical-power maxima and minima in the depicted measurement result (increasing period) can be explained by a nonuniform temperature increase over time. The contrast between interference maxima and minima is however independent of this irregularity.

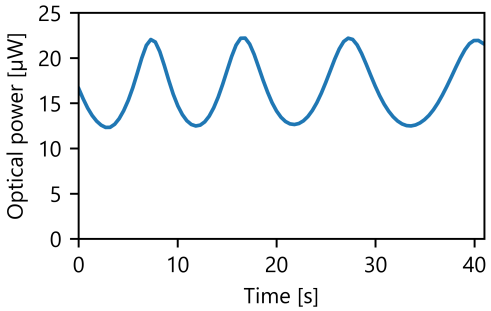

Figure 4.5: Measured photocurrent at the photodiode over the ramped up sample temperature in arbitrary units, resulting in an interference pattern.

The concrete value of the output power depends on the effective coupling efficiency. Nevertheless, the contrast K between interference maxima and minima can be written as (Reference [51])

$$K = \frac{I_{\text{max}} - I_{\text{min}}}{I_{\text{max}} + I_{\text{min}}} = \frac{2R\mathrm{e}^{-\alpha L}}{1 + R^2\mathrm{e}^{-2\alpha L}}. \tag{4.2}$$

Approximating $R\mathrm{e}^{-\alpha L} \approx K/2$ for small K ($K^2 \approx 0$), and doing a logarithm basis change to rewrite the waveguide loss α in dB/cm, it follows that

$$\alpha = \frac{10\log_{10}(\mathrm{e})}{L}(\ln(R) - \ln(R\mathrm{e}^{-\alpha L})) \approx \frac{4.34}{L}(\ln(R) + \ln(2) - \ln(K)). \tag{4.3}$$

The endface reflectivity R for the two crystal orientations can be determined from Fresnel equations [52] (p. 238) and the refractive index obtained by mode-solver simulations. Together with the sample length L and the contrast K, we can calculate the waveguide

loss with great precision independent of the coupling efficiency. This non-destructive loss characterization can be executed for both polarization orientations, but is limited to single waveguides.

A similar characterization method can also be executed using a tunable narrowband cw laser eliminating the need of a Peltier-element and therefore moving parts, due to the temperature shifts in the setup. This method is advantageous for short samples which are generally harder to align. For long samples however, the requirements on the laser's tuning resolution increases as interference maxima move closer together. Therefore, we execute temperature scans for the two investigated samples used for the later quantum optics experiments. We characterize the loss for all straight waveguides which we deposited next to the more complex integrated circuits on each sample for both polarization orientations. The results are shown in Figure 4.6. Both samples show an average loss of 0.03 dB/cm ± 0.02 dB/cm for TM polarized light and 0.01 dB/cm ± 0.01 dB/cm for TE polarized light. The measurement uncertainties are calculated from statistical variations (standard deviation) between the waveguides, showing the good homogeneity along each sample (see Figure 4.6). The measurement uncertainty for the individual values are dominated by the precision of the value for the endface reflectivity for the two crystal orientations, as they are based on simulations and deviations of the individual maxima and minima in each scan as shown in Figure 4.5. Due to the lower waveguide loss for TE polarized light, this polarization is chosen for further experiments. In addition, as the waveguide loss for 8 cm long samples is below 2 %, it is neglected in further investigations.

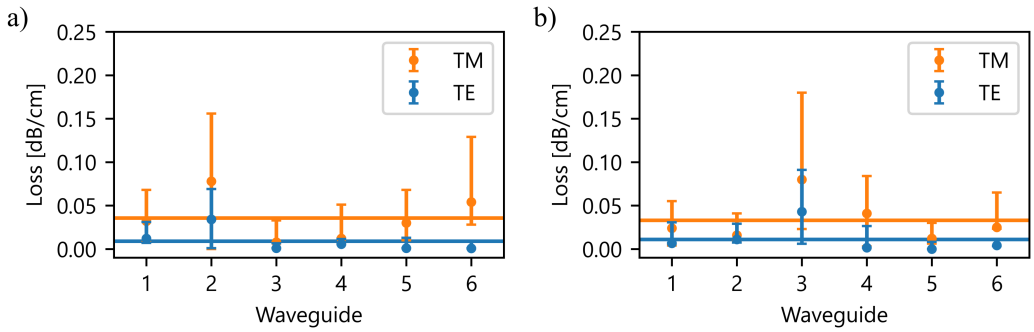

Figure 4.6: Loss measurement results for neighboring waveguides on the fabricated waveguide samples for a) *optical circuit A* and b) *optical circuit B*.

4.2 Integrated directional coupler

For waveguide routing and interference experiments, integrated beam splitters are of great importance. While an integrated beam splitter can be designed in several ways, the so-called zero-gap coupler and large-gap directional coupler are the two most common design approaches for titanium in-diffused lithium niobate waveguides [49]. While the

former offers smaller coupler designs with usually a wide spectral bandwidth [49], we choose large-gap directional couplers with a desired beam-splitting ratio of 50:50 for TE polarization for this work due to a better fabrication predictability.

Table 4.1: Typical values for integrated 50:50 large-gap directional couplers on lithium niobate waveguides, optimized for TE polarization and 1557.4 nm wavelength.

Waveguide width	7 µm
Waveguide distance	127 µm
Coupling length	5450 µm
Waveguide distance (coupling region)	13 µm

The large-gap directional coupler is based on two separate waveguides and a branching region, followed by a straight waveguide section in which optical coupling between the two waveguides occurs due to the evanescent field between the guided modes. This coupled waveguide section is then followed by a second branching region. While the waveguide width stays constant, the beam-splitting ratio depends on the wavelength, length of the coupling region and waveguide distance inside the coupling region.

Typical parameters for achieving a 50:50 beam-splitting ratio for TE polarization at 1557.4 nm wavelength (central wavelength of the Origami laser) are shown in Table 4.1. As the beam-splitting ratio oscillates with the coupling length (dependent on the refractive index), it is possible to also achieve 50:50 beam splitting for both guided polarization orientations. However, for this even longer coupling regions are necessary due to the birefringence. For the two investigated samples, we deposit directional couplers with varying length in addition to straight waveguides for loss characterization to compensate for varying waveguide widths or other imperfections. Figure 4.8 shows the averaged beam-splitting ratio per coupling length for one of the two fabricated samples.

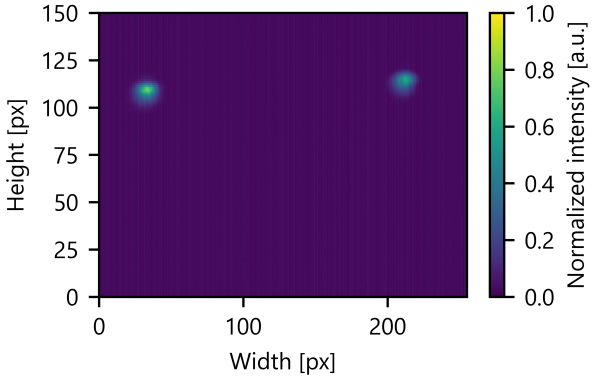

Figure 4.7: Camera picture of the two output modes of an integrated directional coupler.

To characterize the beam-splitting ratio, we use the same setup as for the loss characterization (depicted in Figure 4.4). While the sample temperature is left constant, the photodiode is replaced by an IR-camera. With this camera, the two outcoupled waveguide modes are recorded simultaneously. An example camera picture is shown in Figure 4.7. The two modes are located, pixelwise integrated, and compared.

From the measurement data in Figure 4.8 it can be seen that we reach the targeted 50:50 beam-splitting ratio within the measurement accuracy for light at 1557.4 nm wavelength. Furthermore, using a Sine fit no maximum nor minimum beam-splitting ratio of 100:0 or 0:100 is reached. While this can be caused by an insufficient background filtering or non-optimal camera settings, the investigation of the ideal coupling length for 50:50 splitting is not influenced. Therefore, as already shown in Table 4.1, the optimal coupling length for TE polarization and 1557.4 nm wavelength is determined to be 5450 µm for a large-gap directional coupler. Using the same beam splitter for TM polarized light, we determine a beam-splitting ratio of 78:22. While these structures are characterized and initially optimized for 1557.4 nm light, we also execute a wavelength scan up to 1570 nm in 1 nm steps. The measurement results are shown in Figure 4.9. We determine the standard deviation of the calculated beam-splitting ratio to be 4 %. This result shows a sufficient spectral bandwidth, even compared to commercially available fiber beam splitters [53].

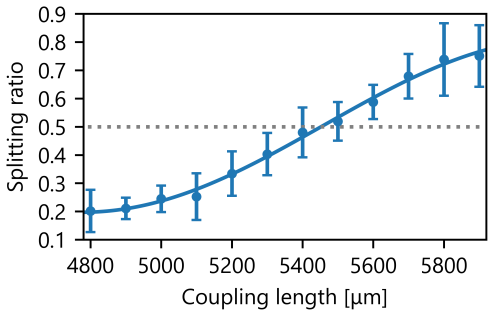

Figure 4.8: Beam-splitting ratio over coupling length in TE polarization for one fabricated lithium niobate waveguide sample (*optical circuit B*) and corresponding Sine fit. The dotted line shows the targeted 50:50 beam-splitting ratio.

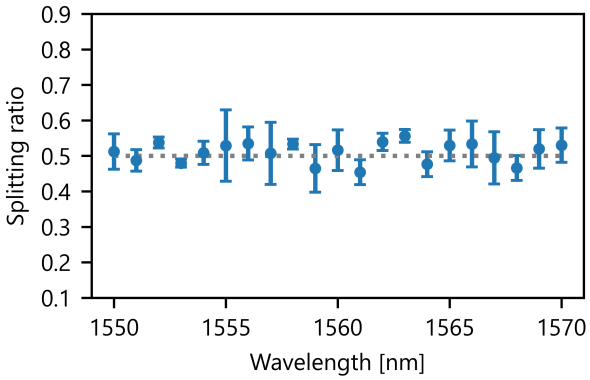

Figure 4.9: Beam-splitting ratio over wavelength in TE polarization for one fabricated lithium niobate waveguide sample (*optical circuit B*). The dotted line shows the targeted 50:50 beam-splitting ratio.

4.3 Multi-channel fiber interfacing

For modular integrated circuits, where an integrated circuit is combined with freespace optical components, efficient and stable coupling in and out of the integrated circuit is important. For multi-channel circuits such as the integrated beam splitter, coupling with optical lenses is difficult, especially when different optical quantum states are coupled. As mentioned in Section 4.1.1, the single-mode waveguides in lithium niobate are optimized to match the modesize of a standard single-mode fiber at 1550 nm photons. Therefore, optical coupling can be achieved by moving an optical fiber close to the sample endface. Additional antireflective coatings on the sample endface as well as the fiber endface can improve the coupling. However, for a robust and more compact solution, the fiber is glued to the sample endface with an index-matching glue. Endface coupling is sometimes called buttcoupling and gluing a fiber to the endface is called pigtailing. Even polarization-maintaining fibers can be used for efficient coupling. The highest experimental pigtailing efficiency is 92 % for TE polarized light and 85 % for TM polarized light including anti-reflective coatings [54]. For the fabricated samples presented in this work, we achieve a maximum coupling efficiency of 78 % per (four-channel) interface for both polarization orientations (see Table 4.2). One endface (input side) is connected to a four-channel polarization-maintaining fiber, while the other endface (output side) is connected to a four-channel single-mode fiber. As deviations of the waveguide distance or distance between two fiber cores (127 µm) in the v-groove ferrule can prohibit efficient multi-channel coupling, a coupling efficiency of 70 % per interface is a reasonable expectation value for multi-channel coupling with no additional coatings.

As a single fiber ferrule consists of one fiber with core and cladding encased in a polished, solid glass housing with an endface in the square-millimeter range, the connection of several single-fiber ferrules per waveguide endface is not feasible. Nevertheless, multi-

channel fiber interfacing is possible using v-groove ferrules, consisting of multiple fibers per ferrule with a fixed distance of 127 µm, as depicted in Figure 4.10 b). This multi-channel fiber design is commercially available for single-mode and polarization-maintaining fibers with up to six channels. The fabrication steps for multi-channel fiber pigtailing a beam splitter structure are shown in Appendix A.7.

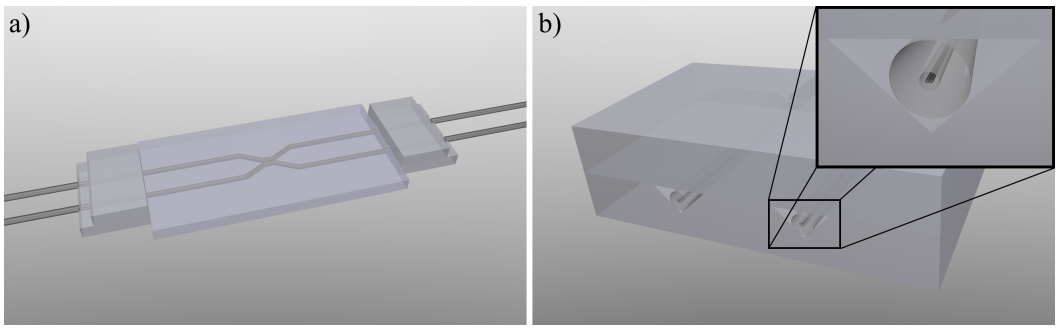

Figure 4.10: Illustration of a) a multi-channel pigtailed integrated optical circuit and b) v-groove fiber ferrule. The inset shows the orientation of the fiber's slow axis parallel to the waveguide surface

Figure 4.11 shows the curing process, when pigtailing the second endface. While the fabrication steps shown in Appendix A.7 describe two-channel fiber pigtailing, this process can directly be adapted for four-channel interfaces.

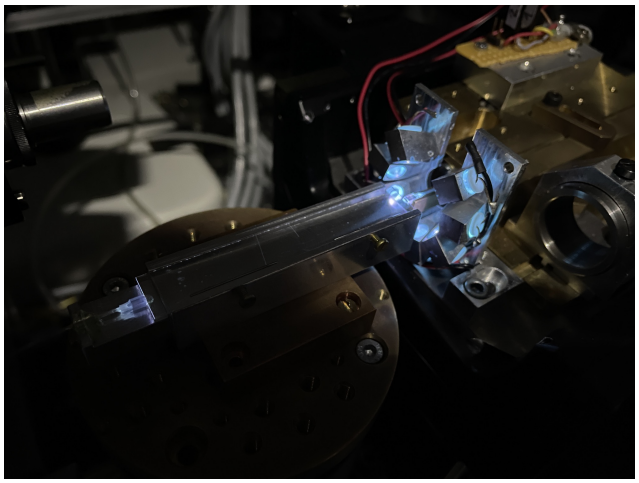

Figure 4.11: Photograph of a sample while executing Step 10 (Appendix A.7) of the pigtailing process for the second endface.

4.4 Integrated optical circuits

After discussing the fabrication and characterization of integrated low-loss fiber-coupled routing structures, this section summarizes the results of the two optical circuits, introduced in Section 2.4.1 and Section 2.4.2. For both circuits, the fabrication scheme from Section 4.1.1 is used and we verify low-loss waveguiding as described in Section 4.1.2. Using varying coupling lengths for the integrated beam splitters, we determine the optimal coupling length for 50:50 coupling, as described in Section 4.2, and fiber-couple both samples, as explained in Section 4.3. Figure 4.12 shows photographs of the two fabricated samples. Table 4.2 summarizes the characterization results. With these fiber-coupled integrated circuits, it is possible to feed in the two quantum states, explained in Chapter 3. The two outer fibers on the output side can be connected to fiber-coupled superconducting nanowire single-photon detectors, for single-photon measurements and photon subtraction. The two inner ports form the resulting two-mode quantum state, which is further investigated.

Table 4.2: Comparison of the characterization results for the two fabricated waveguide samples.

Sample	*Optical circuit A*	*Optical circuit B*
Waveguide loss (TE polarization) [dB/cm]	0.01 ± 0.01	0.01 ± 0.01
Splitting ratio (TE polarization) [%]	52:48 (± 4 %)	51:49 (± 4 %)
Pigtailing efficiency (input) [%]	72 ± 2	77 ± 2
Pigtailing efficiency (output) [%]	78 ± 2	77 ± 2

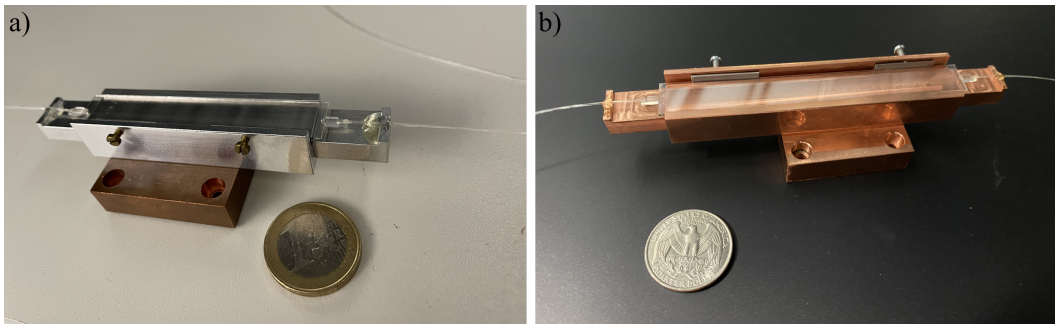

Figure 4.12: Photographs of the fabricated samples: a) *optical circuit A* and b) *optical circuit B*.

When sending a coherent state through one of the inputs of *optical circuit A*, it causes an equal distribution of along the four different outputs due to the cascaded 50:50 beam splitters. For *optical circuit B*, as discussed in Section 2.4.2, the light distribution over the four output channels depends on the phase difference within the interferometer structure. Therefore, when we investigate the coupling ratio of the four outputs prior to or after pigtailing (as shown in Figure 4.13) we measure no equal distribution as expected. This measurement shows the stable phase relation of the two paths of the interferometer which

cannot be modulated in this passive circuit. The clearly visible minimized light intensity in the second output is the result of a $2n/\pi$ phase relation of the two paths. While also a damaged output port can cause this outcome, this is excluded when using a different input port of the symmetric design and measuring a reduced intensity in Output 3.

In summary, titanium in-diffused lithium niobate waveguides, fabricated using the presented technologies, are a promising tool for creating complex integrated routing structures for low-loss quantum optics experiments.

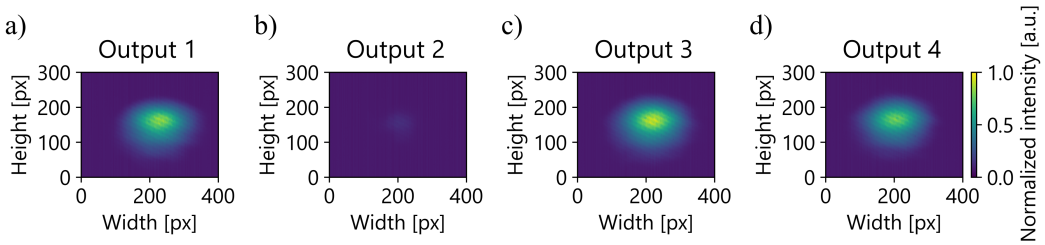

Figure 4.13: Measurement results for the coupling ratio based on the scheme presented in Section 4.2 for the fabricated sample *optical circuit B*.

Measurement-induced nonlinearity with integrated circuits

5

In this chapter, we explore the experimental realization of measurement-induced nonlinearity. For this, we combine the setup to create the various input states from Chapter 3 with the fabricated integrated circuits from Chapter 4. For both circuit designs (*optical circuit A* and *optical circuit B*), we investigate interference effects and the influence of a measurement operation, similar to the theoretical findings in Chapter 2. For a complete overview of the experimental setup, Figure 5.1 shows a simplified schematic.

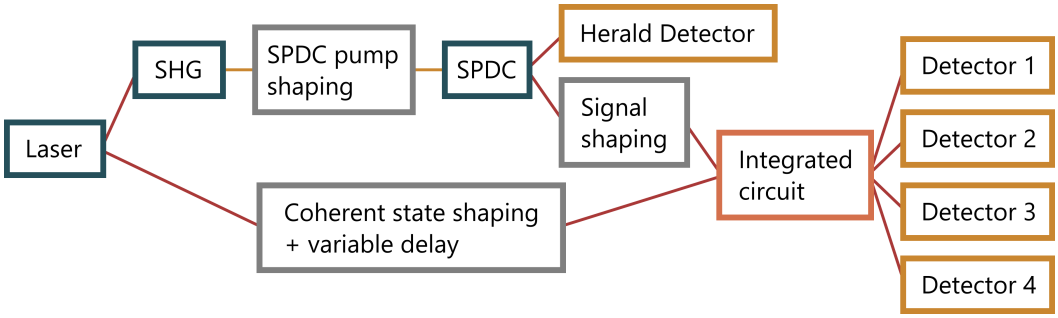

Figure 5.1: Simplified schematic of the experimental setup for investigating measurement-induced nonlinearity as an extension of the schematic for the input-state creation in Figure 3.1 with colored boxes based on the illustration in Figure 1.1. The connecting lines represent a laser beam with red corresponding to 1550 nm wavelength and yellow corresponding to 775 nm wavelength. The wavelength conversion is caused by second harmonic generation (SHG) and spontaneous parametric down-conversion (SPDC).

The more complex illustration in Figure 5.2 combines the elements from Figure 3.2, the fiber-coupled integrated circuits, and single-photon detectors. With this setup, the created single photons from a heralded SPDC process and coherent state are spectrally and temporally shaped for maximum interference visibility, and then routed in one of the passive integrated circuits. The four outputs of the optical circuit are sent to superconducting nanowire single-photon detectors, housed in a helium sorption cryostat. The specifications of the five single-photon detectors are shown in Appendix Table A.3. Additional fiber-polarization controllers are used to optimize the polarization-dependent detection efficiency. The detector responses of the individual detectors are read out with a time-to-digital converter (time tagger). As discussed in Section 2.3, the indistinguishability between photons determines the interference effects between them. Therefore, it is critical that both narrowband filters

in the form of the grating-scanning single-photon spectrometers, are set up identically. In addition, the polarization is set identically in both arms to match the TE polarization direction in the samples. To compensate dispersion effects, great care is taken that all fiber lengths are equal for both states before the interference. Furthermore, by scanning the variable optical delay line, the temporal overlap of the states is optimized. This setup is built up for both integrated circuits and the results are presented in the following sections.

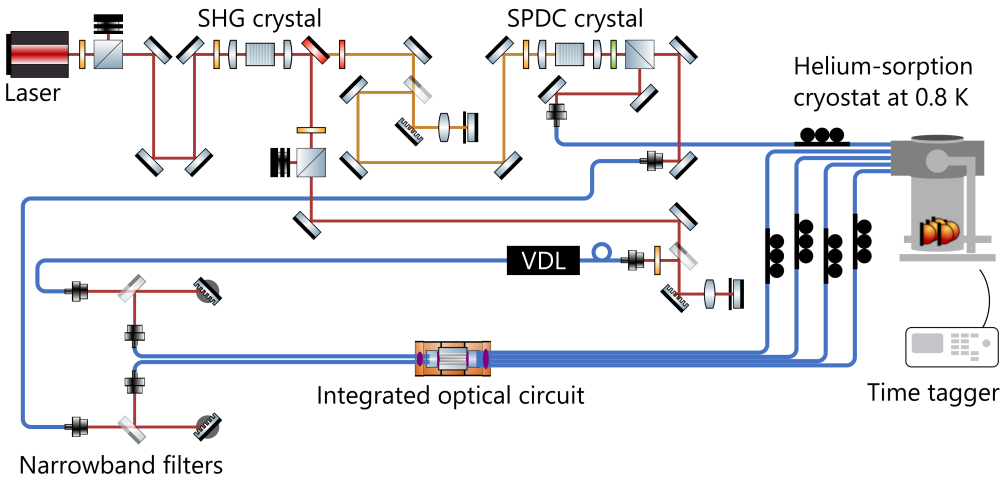

Figure 5.2: Detailed experimental setup for investigating measurement-induced nonlinearity as an extension of the input-state creation in Figure 3.2. Wavelength conversion is caused by second harmonic generation (SHG) and spontaneous parametric down-conversion (SPDC). The arrival time of photons at one input of the integrated optical circuit is controlled by a variable delay line (VDL). Component drawings are partially taken from Reference [37].

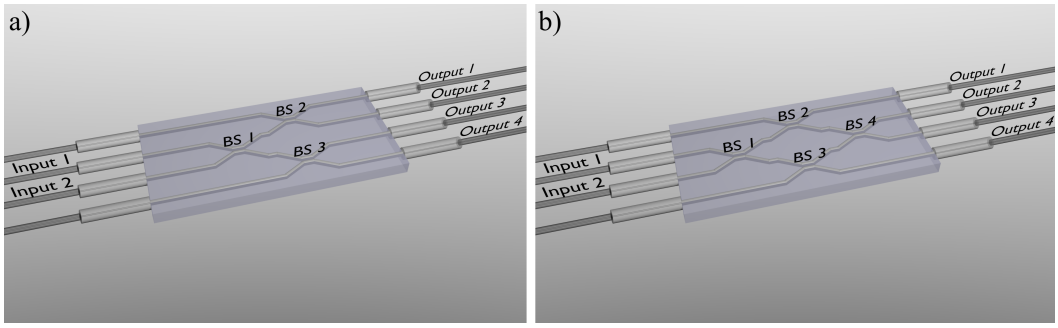

Figure 5.3: Illustrations of the two investigated designs: a) *optical circuit A* and b) *optical circuit B*. Input ports are labeled with Input 1 and Input 2, integrated beam splitters are labeled with BS 1 to BS 4, and output ports are labeled with Output 1 to 4.

5.1 Optical circuit A

In this section, we investigate interference effects and measurement-induced changes in the photon-number statistics for *optical circuit A* which is shown with labeled ports in Figure 5.3 a), while a picture of the sample is shown in Figure 4.12 a). Using the two input ports, consisting of polarization-maintaining fibers, the two input states interfere at the first beam splitter (BS 1). After that, each individual output of the beam splitter is again split into two outputs with no recombination.

5.1.1 Single-photon interference

Due to the single interference beam splitter in *optical circuit A*, a photon-bunching effect is expected, when both input states arrive simultaneously, according to the findings in Section 2.3. Using the setup in Figure 5.2, we can change the arrival time of the coherent state using the variable optical delay line. Postselecting on the detection of a herald photon, the individual countrates in the four output arms are not influenced by the delay setting (and therefore the coherent state arrival time), as can be seen in Figure 5.4.

When looking at the coincidence detection of a herald photon and combinations of two outputs of the integrated circuit, an influence of the coherent state arrival time becomes visible, as shown in Figure 5.5. It can be seen, that the probability for a coincidence detection of a herald photon together with a photon from Output 1 and Output 2 (HO1O2) increases when overlapping the two input states in time. The same holds for a coincidence detection of a herald photon together with a photon from Output 3 and Output 4. On the contrary, all other threefold combinations become less likely. As discussed in Section 2.3, the interference of a weak coherent state and single photon on a 50:50 beam splitter causes a bunching effect, similar to the Hong-Ou-Mandel effect for two indistinguishable single photons. The two bunched photons are as likely to be detected at each individual output of the circuit. However, as the utilized detectors are all click detectors, a pure single-photon

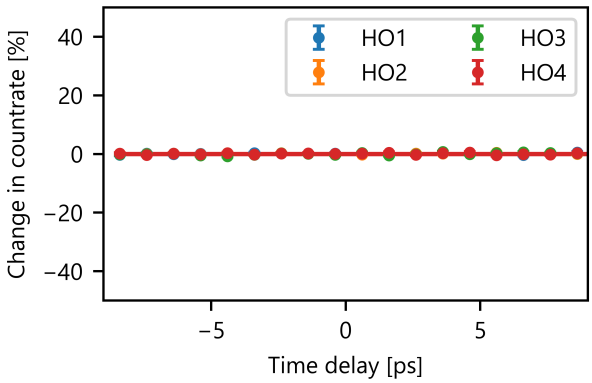

Figure 5.4: Percentage change in countrate for the four outputs postselected on a herald detection over the set time delay for *optical circuit A*, normalized to the constant countrate outside the shown measurement window. For a better comparison, the range of the vertical axis is chosen to match the vertical axis in Figure 5.5.

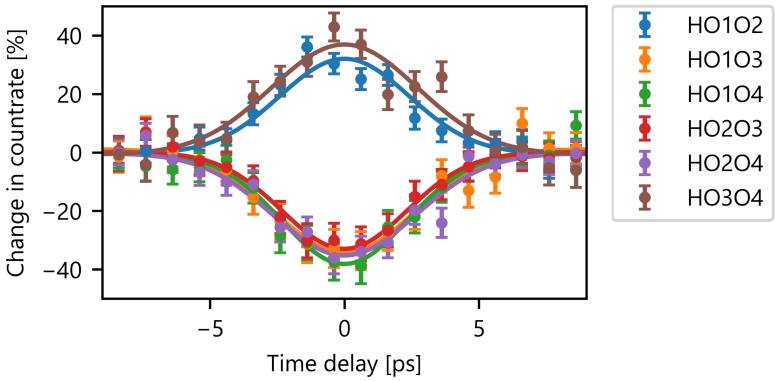

Figure 5.5: Percentage change in countrate for the simultaneous detection in two outputs postselected on a herald detection over the set time delay, normalized to the constant countrate outside the shown measurement window, and corresponding Gaussian fitting for *optical circuit A*.

detection cannot be differentiated from a two-photon detection in contrast to pure photon-number resolving detectors [55]. Nevertheless, the additional beam splitters in *optical circuit A* provide the possibility of distributing the bunched photons onto two detectors which share the same output port of the first beam splitter. With this, the bunching effect leads to an increased probability of measuring a photon pair in these outputs. Detection events for combinations of other outputs, as for example Output 1 and Output 3, are reduced for the same reason. The summation of these four output combinations for a coincidence detection is shown in Figure 5.6. From this, the interference visibility is calculated to be 35 %. As discussed in Section 2.3, the interference visibility depends on the indistinguishability of the inputs and coherent-state amplitude. While loss in the input arm of the coherent state only influences the coherent-state amplitude, photon loss in the single-photon state also drastically reduces the interference visibility, as shown in Figure 2.12 different from the interference of two single photons. Here, a background subtraction, based on the individual blocking of the two input states is not valid. The blocking of the single-photon input can be interpreted as 100 % loss at this input which was investigated in Section 2.3. Due to the positive slope of p_{aa} in Figure 2.12 b), this background subtraction can result in negative probabilities and the HOM visibility is no longer upper bounded by one, leading to a visibility of 105 % in this case. When we include loss and an individually measured coherent state mean photon number of $\bar{n} = 0.04$ in QuTiP simulations, a maximum visibility of 39 % is calculated. The included loss is based on the Klyshko efficiency (Section 3.3.3), pigtailing efficiency (Section 4.3), and detection efficiencies (Table A.3). It can be seen that the experimental results almost reach the theoretical limit which includes loss effects but no mode mismatch between the input states.

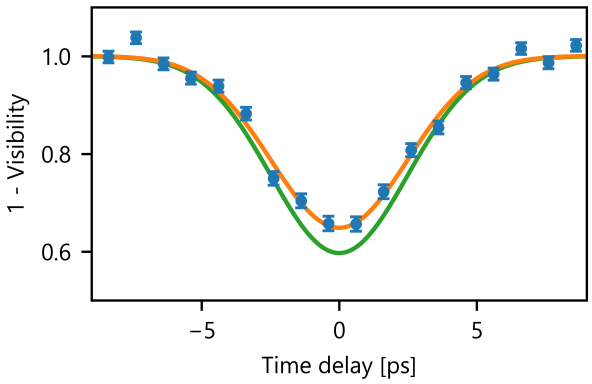

Figure 5.6: Interference visibility based on Equation (2.22) for the coincidence detection in the output combinations O1O3, O1O4, O2O3, and O2O4 postselected on a herald detection over the set time delay and corresponding Gaussian fitting for *optical circuit A* in orange. The green line marks the maximum visibility based on QuTiP simulations.

5.1.2 Measurement-induced changes in the photon-number statistics

In the previous section, changes in the arrival time of one input state were investigated for threefold detection events, including pairs of outputs of *optical circuit A* and the herald detector. In this section, we also investigate fourfold and fivefold detection events while keeping the variable delay line at the point of maximum interference visibility. The unprocessed recorded detection events for the five click detectors (including the herald detector) are shown in the second column of Appendix Table A.7. For comparison, Appendix Table A.8 shows the data when blocking the single photon state and just using the coherent state input. Postselecting and therefore dividing by the number of clicks from the herald detector, the individual probabilities of the different click events are shown in the third column.

As each output arm of the first beam splitter in *optical circuit A* is split and sent to two detectors, a quasi-photon-number resolution can be determined. Here, the click events on one individual detector necessarily contribute to coincidence counts with other detectors. Therefore, subtraction of higher orders allows for a gradual convolution of single click events, as shown in Reference [56]. Nevertheless, a single click event (at one detector) can still be caused by multiple photons. The resulting click statistics for the two arms of the first beam splitter for *optical circuit A* are shown in Figure 5.7.

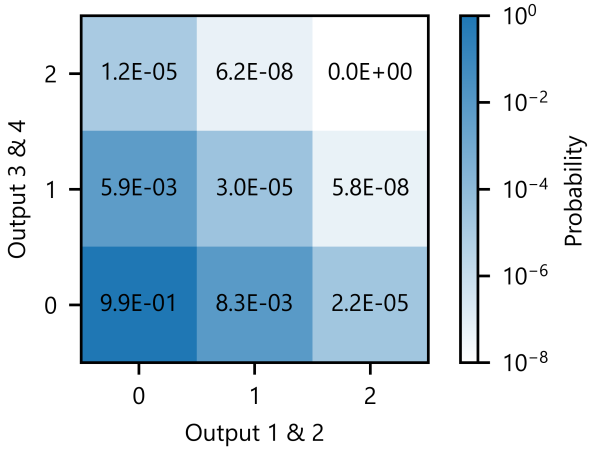

Figure 5.7: Measurement results for the photon count statistics based on coincidence click detection events of the output combinations Output 1, Output 2 and Output 3, Output 4, all postselected on a herald detection for *optical circuit A*.

Up to now, all four detectors after the integrated circuit were treated in the same way. As discussed in Section 2.4, the combination of one beam splitter with the vacuum state in one input port and a detector in one output port, can be seen as a photon-subtraction scheme. Furthermore, the nonlinear influence of a measurement can be investigated in that way. Therefore, Output 1 and Output 4 are now treated as the measurement detectors,

which should induce nonlinearities, while the two-mode state in Output 2 and Output 3 is treated as a newly created quantum state. This scheme matches the theoretical scheme in Section 2.4.1.

Using the same dataset as presented in Figure 5.7, we investigate the photon statistics of the two-mode output state, characterized with the detectors connected to Output 2 and Output 3, and postselected on different measurement combinations of Output 1 and Output 4. The results are presented in Figure 5.8.

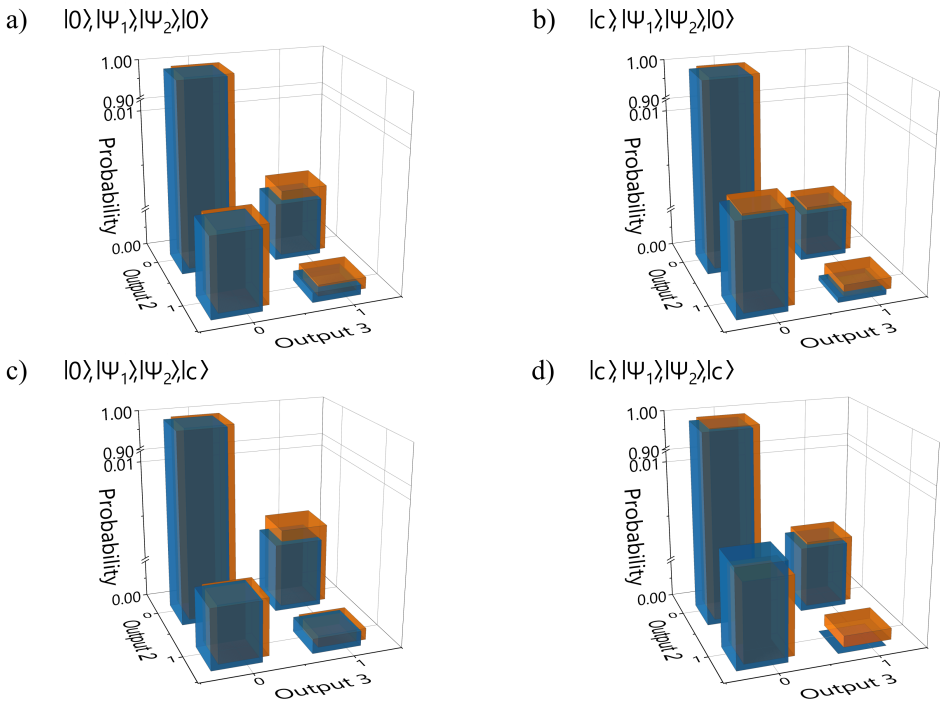

Figure 5.8: Photon count statistics of Output 2 and Output 3, postselected on different detection events in Output 1 and Output 4 and postselected on a herald detection for *optical circuit A*. The state $|c\rangle$ represent a click detection and therefore a state with at least one photon at this output. The blue bars correspond to the measured data, the orange bars correspond to simulation results.

Despite the experimental results not showing effects of measurement-induced nonlinearity like the shifted discorrelation as clearly as in the simulation in Figure 2.17, features of the induced nonlinearity are visible. This can be seen in the [0,1] or [1,0] output combinations when we compare the results in Figure 5.8 a) to the results in Figure 5.8 b), and Figure 5.8 c). Here, the probability of single elements are increased, despite the intuition that a photon detection and therefore annihilation should not increase the probability of finding a photon somewhere else but linearly reduce the state by one photon. Precisely, the probability of measuring a photon in Output 2 increases by 27 % when subtracting at least one photon in the adjacent output, and it decreases by 40 % when subtracting at least one photon in the other output. For Output 3, the probabilities increase by 35 % and decrease by

36 %, respectively. QuTiP simulations (orange bars in Figure 5.8) including loss predict an increase of 31 % for the adjacent and decrease of 44 % for the nonadjacent output. It must be pointed out that this increase only occurs when postselecting on the measurement subset with successful photon subtraction.

Unfortunately, with the presented measurement scheme and evaluation it is not possible to investigate the creation of two-mode squeezing in the output state in phase-space (in terms of the real and imaginary components of the electric field, see Appendix A.1). However, Riabinin et al. showed in their theoretical simulations that two-mode squeezing is induced, also discussed in Section 2.4. Simulation results in Figure 5.8 are based on the ideal model, presented in Section 2.4.1. With the included loss for a nonperfect single-photon source (based on the Klyshko efficiency, pigtailing efficiency, and detection efficiencies), the model fits the experimental findings.

To summarize, measurement-induced nonlinearity can be created with the experimental setup including *optical circuit A*. Theoretical calculations including imperfections match the experimental findings. By optimizing the experimental setup with focus on interface loss including misalignment and optimizing the heralding efficiency of the single-photon source, the visibility of the measurement-induced nonlinearity can be increased further. As the experimental results agree well with the theoretical model, the not yet validated expectation for the creation of two-mode squeezing seems promising.

5.2 Optical circuit B

For the integrated *optical circuit B*, depicted in Figure 5.3 b), we execute the same experiments as for the previous circuit in Section 5.1. Due to the additional beam splitter in the integrated circuit, we expect that different correlations between the photons in the four outputs are visible. While it can be expected that these photon statistics depend on the phase relation within the on-chip Mach-Zehnder interferometer structure, it is not possible to actively manipulate the phase on this passive device. The integration of an active phaseshifter is in principle possible on integrated lithium niobate waveguides. However, this would add more complexity to the circuitry and can be investigated in future experiments.

5.2.1 Single-photon interference

Following on the results presented in Section 5.1.1, the photon-bunching effect for the simultaneously arriving input states should have a different effect on the four output states, due to the additional beam splitter. However, the photons guided to the two outer ports (Output 1 and Output 4) should still follow the photon-bunching effect caused by the first beam splitter. Similar to *optical circuit A*, the individual countrates in the four output arms, postselected on a herald detection, are not influenced by the delay setting, as shown in Figure 5.9.

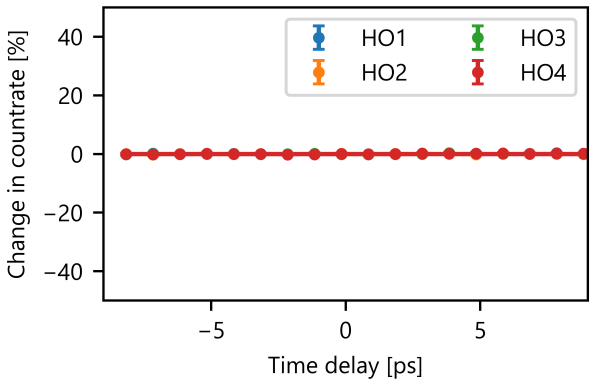

Figure 5.9: Percentage change in countrate for the four outputs postselected on a herald detection over the set time delay for *optical circuit B*, normalized to the constant countrate outside the shown measurement window. For a better comparison, the range of the vertical axis is chosen to match the vertical axis in Figure 5.10.

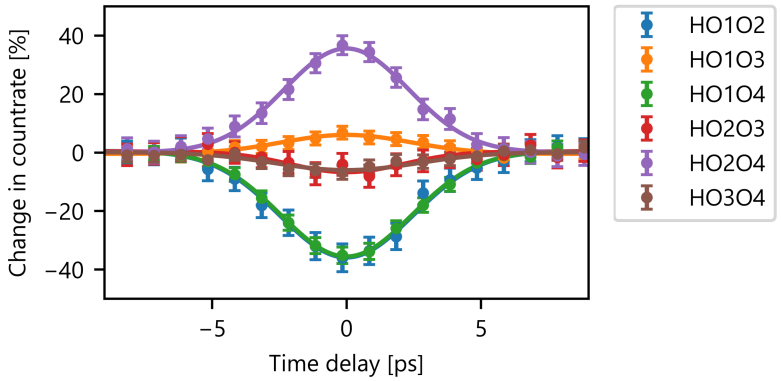

Figure 5.10: Percentage change in countrate for the simultaneous detection in two outputs postselected on a herald detection over the set time delay, normalized to the constant countrate outside the shown measurement window, and corresponding Gaussian fitting fo *optical circuit B*.

As expected, the simultaneous detection of at least one photon in Output 1, Output 4, and the herald detector is suppressed at zero time difference due to the photon bunching, as shown in Figure 5.10. The other combinations of outputs show different curve progressions when varying the time delay of the two input states, compared to the findings for *optical circuit A* in Figure 5.5. Especially the positive change for the combination of Output 2 and Output 4 at zero time delay and the negative change for the combination of Output 1 and Output 2 can be noted. These trends are caused by the fixed-phase Mach-Zehnder structure and can be reproduced using QuTiP simulations as shown for the photon count statistics at maximum interference in Figure 5.12. The break of symmetry, when comparing the different output combinations are partially caused by imperfections of the integrated beam splitters, but primarily by the phase relation of the two paths, together with the initial asymmetry, as the two different input states enter the sample from two distinct inputs.

To compare the interference visibility of the two fabricated samples, we determine the HOM visibility, based on the dip for coincidence detections in Output 1 and Output 4. The results are shown in Figure 5.11. For this structure, an experimental visibility of 36 % and simulated maximum visibility of 40 % is calculated based on Equation (2.22), similar to the values for the previous structure (see Section 5.1.1). Therefore, we can assume that the setup settings as well as the fabrication quality of the integrated circuits are comparable.

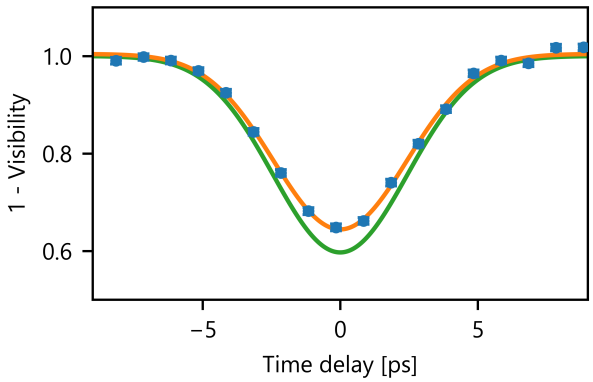

Figure 5.11: Interference visibility based on Equation (2.22) for the coincidence detection in the output combination Output 1 and Output 4 postselected on a herald detection over the set time delay and corresponding Gaussian fitting for *optical circuit B* in orange. The green line marks the maximum visibility based on QuTiP simulations.

5.2.2 Measurement-induced changes in the photon-number statistics

Based on Figure 5.10 and Figure 5.11, the time delay for maximum interference is clearly visible. With this setting, we investigate all different combinations of outputs. The measurement data is shown in Appendix Table A.9 and Table A.10. Compared to *optical circuit A*, it is not feasible to divide the circuit into two independent parts. Nevertheless, when

considering Output 2 and Output 3 as a newly created two-mode quantum state, the influence of a measurement operation in Output 1 and, or Output 4 on this state is investigated. The corresponding results are shown in Figure 5.12. Here, the nonlinear influence of the measurement is less visible.

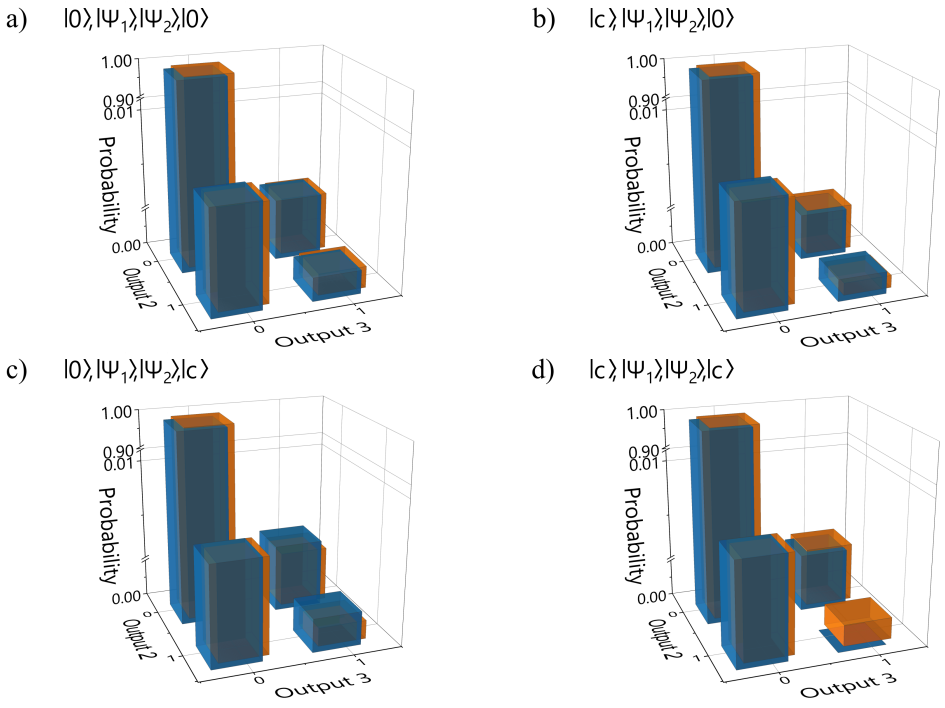

Figure 5.12: Photon count statistic of Output 2 and Output 3, postselected on different detection events in Output 1 and Output 4 and postselected on a herald detection for *optical circuit B*. The state $|c\rangle$ represent a click detection and therefore a state with at least one photon at this output. The blue bars correspond to the measured data, the orange bars correspond to simulation results.

The simulation results shown along with the experimental results in Figure 5.12, agree with each other although the phase difference in the Mach-Zehnder structure must be considered. While optimizations of the optical setup can drastically improve the visibility of the measurement-induced nonlinearity, Riabinin et al. showed that even with an optimized phase setting, the maximum two-mode squeezing which can be created with this circuit equals the maximum squeezing which can be created with *optical circuit A* [24]. Nevertheless, the realization of *optical circuit B* and the good long-time phase stability within the integrated circuit gives a promising outlook for future complex experiments.

All in all, the combination of the single-photon and coherent state source with the optical circuits reveals interesting features in the photon count statistics. Especially, an increased probability of finding a photon at a specific output despite photon subtraction is a clear indicator for measurement-induced nonlinearity. Furthermore, the great agreement between theoretical simulations and experimental findings indicates an extensive understanding of

the elaborated scheme.

Integrated Detectors 6

In Chapter 5, only commercial fiber-coupled superconducting detectors were used, as they are optimized for high detection efficiency and low noise. The integration of single-photon detectors onto waveguides working with evanescent coupling enables a simplification of the already discussed circuit designs and therefore also the expansion to more complex circuits and better scalability, as illustrated in Figure 6.1.

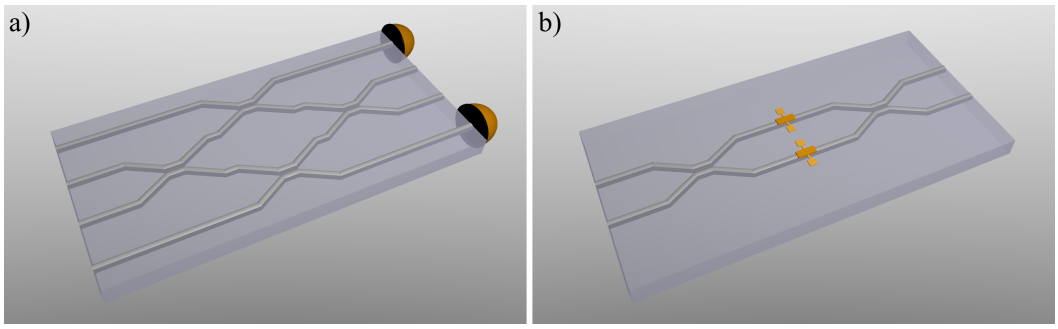

Figure 6.1: Illustration of the transition from *optical circuit B* using endface-coupled detectors in a) to the same circuit design using integrated detectors in b). Each integrated detector replaces one beam splitter and one endface-coupled detector due to evanescent coupling.

In this chapter, the work on two types of integrated superconducting single-photon detectors on lithium niobate waveguides is presented, namely the superconducting nanowire single-photon detector (SNSPD) and transition edge sensor (TES). This work was done in collaboration with the National Institute of Standards and Technology (NIST) in Boulder, Colorado. Waveguide samples were fabricated by the Paderborn University IQO Technology team led by Christof Eigner. TESs were fabricated by Adriana E. Lita and SNSPDs were fabricated by Varun B. Verma at NIST.

The important figures of merit for these detectors are introduced in Section 6.1. Subsequently, the individual working principles and an overview of existing work on integrated detectors on other material platforms are described. After that, we show the characterization results for integrated SNSPDs in Section 6.2, followed by the integrated TESs in Section 6.3.

6.1 Basics

The fundamental principle of single-photon detection is the creation of an electrical, or more generally computer-storable signal given the presence of a photon. When the photon is absorbed by the detector, it must transfer all its energy and, as it has no rest energy, therefore annihilate itself. For a successful photon detection, three criteria have to be fulfilled, similar to Reference [57] (p. 4):

1. The photon must reach the detector (collection efficiency)
2. The photon must be absorbed by the detector (absorption efficiency)
3. The absorbed photon must lead to a signal (internal efficiency)

Altogether, this gives the ***detection efficiency*** which is defined as the ratio between detected and impinging photons. While point one and two are usually tackled by optimizing the detector geometry or by using optical cavities, point three depends mostly on the intrinsic detection mechanism. As most detection mechanisms rely on the photo-electric effect of the absorbed photons in a metal or the electron-hole-pair creation in semiconductors, it is intuitive that this photon-to-current transformation strongly depends on the quantized photon energy, proportional to its frequency. For example, the detection efficiency of a silicon SPAD detector can reach 74 % for photons at 600 nm wavelength [58], but it goes to zero at telecommunication wavelengths around 1550 nm. The latter wavelength is very interesting for quantum optics, as optical fibers, one of the key components for light routing, have low transmission loss in this wavelength range and therefore many devices taken over from classical optics are optimized for this as well. Some detectors for this wavelength therefore consist of a frequency converter followed by a semiconductor detector optimized for lower wavelengths. Other semiconductor detectors, for example based on indium gallium arsenide, work at the desired wavelength. However, both techniques still have problems reaching more than 60 % detection efficiency and keeping a small noise floor at 1550 nm wavelength [59, 60]. Over the last two decades, a new detection mechanism for light detection at telecommunication wavelength became prominent in quantum optics [61–66]. This mechanism relies on the (partial) breakdown of superconductivity in a metal compound due to single-photon absorption. In recent years, these detectors have taken the lead in terms of detection efficiency (above 90 %) [67, 68], but also dark counts [69], timing jitter [70] and photon-number resolution [71]. Together with the recovery time and the already discussed detection efficiency, these form the important figures of merit for single-photon detectors and are now introduced in more detail.

Dark counts can be defined as false detector signals without an impinging photon and are normally stated as number of signals per second. These signals can come for example from fluctuations in the electrical current or other imperfections. For most experiments, dark counts are set equal to false counts, which also include unwanted counts from photons that should not be included in the experiment like room-light photons, high-energy photons

from space or black-body radiation. These error sources can often be reduced by additional shielding of the experiment or time-gating.

Timing jitter can be seen as the temporal uncertainty of a photon-detection event. Assuming a perfectly known arrival time of a photon, the arrival time of the created electrical signal will have some uncertainty, caused by the detection mechanism, detector design, and further electrical components including oscilloscopes or time taggers, but also electrical cables. The arrival time of a photon can be an important information in an experiment, for example when using the arrival time as an encoding basis or when applying a temporal acceptance window to minimize dark counts. Hence, a small timing jitter is desirable.

The ***recovery time*** can be defined as the period of time for the detector to reach its initial state after a detection event. Therefore, the maximum speed at which a detector can reliably operate equals the multiplicative inverse of the recovery time. It is related to the dead time which is the timing window in which the detector is not able to process a second photon after it detected one photon. In most cases, the dead time is slightly shorter than its recovery time.

Photon-number resolution is an additional feature of some single-photon detectors. Here, the output-signal shape or height is different for different impinging photon numbers. Therefore, it is possible to measure the number of photons for example of one laser pulse. For monochromatic light, some energy-resolving detectors can be transformed into photon-number-resolving detectors. A lack of photon-number resolution can partially be compensated by spatial or temporal detector multiplexing. However, multiplexing can be highly resource intensive and, as it is based on beam splitting, the possibility that more than one photon is detected by a non-photon-number resolving detector at once remains. This reduces multiplexing to a quasi-photon-number resolution which is sufficient for a lot of experiments [12] (pp. 217-241).

6.1.1 Superconducting nanowire single-photon detectors

One type of the already mentioned superconducting detectors is the superconducting nanowire single-photon detector (SNSPD). This detector type, which is used in the measurements in the previous chapters, first introduced by Gol'tsman et al. in 2001 [66] was optimized over the last decades to match current quantum optics applications [6, 72, 73]. Remarkable milestones were a reported detection efficiency of 93 % by Marsili et al. in 2013 [67] and 98 % by Reddy et al. in 2021 [68] at 1550 nm wavelength, dark counts of below one count per day, demonstrated by Hochberg et al. [69], timing jitter of 2.7ps at 400 nm and 4.6 ps at 1550 nm wavelength by Korzh et al. [70], and recovery times of 480ps by Münzberg et al. [74]. It must be noted that all these figures of merit cannot be reached within one state-of-the-art detector, as timing- and efficiency properties are often contrary. Therefore, commercially available detectors often have trade-offs in one or two figures of merit, depending on the application as shown in Table 6.1.

Table 6.1: Comparison of a commercially available SNSPD and the highest reported figures of merit for SNSPDs and TES

Detector type	Commercial SNSPD detector (Photonspot)	Best values reported (SNSPD)	Transition edge sensor [71]
Detection efficiency	85 %	98 % [68]	95 %
Dark counts	100 cps	$< 10^{-4}$ cps [69]	"negligible"
Timing jitter	70 ps	4.6 ps [70]	4 ns
Recovery time	50 ns	480 ps [74]	1 µs

In nearly all SNSPD designs, the detector outcomes look the same for all input photon numbers, depicted in Figure 6.2. The detectors act as click detectors and have no photon-number resolution. However, this property is more related to the detector-readout scheme as groups have shown that a photon-number resolution is per se not impossible for SNSPDs [75, 76]. Nevertheless, it is more convenient for most experiments to multiplex SNSPDs to gain information about photon numbers.

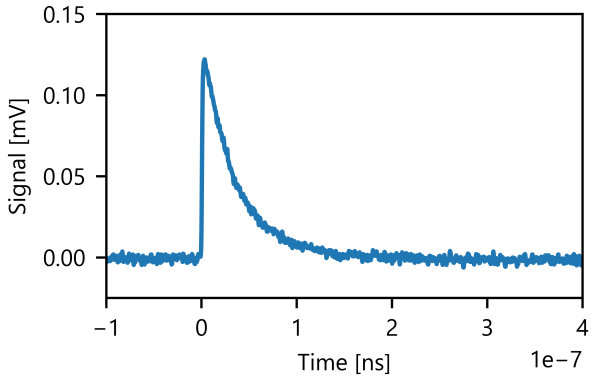

Figure 6.2: Amplified electrical detector response of a commercial superconducting nanowire single-photon detector after photon absorption.

The working principle of SNSPDs is an ongoing research topic, as new detector geometries give further insight in the microscopic processes in the detector [77]. A simplified model based on Reference [5, 78] and [57] (pp. 8-9) is depicted in Figure 6.3. To reach the superconductive state of the detector, the device (including a fiber-channel) has to be cooled down in a cryostat below its critical temperature. With a stable current source, the detector is biased just below its critical current. At this point, it is sensitive to the energy of a single photon even at infrared wavelengths. The energy absorption of one photon is sufficient to break down the superconductivity locally, called hotspot. To do so, the detector has to have a height in the nanometer range. Within this thin, biased wire, a magnetic vortex (topological defect in a thin, superconducting film [79]) is formed, crossing through the

wire, perpendicular to the charge flow, and resulting in an increase of the superconductive breakdown (resistive slab [57] (p. 8)). With this, a measurable voltage peak at the read-out line is created. Next, the wire can return to its initial state, as the current dissipates through a parallel resistor. It has to be noted that the operating temperature and necessary bias current depend on the device material and geometry, and are often in the range of 1-4 K and 5-20 µA. Common materials for SNSPDs are NbN, NbTiN, MoSi, and WSi which differ in their temperature-, timing-, and fabrication yield-properties [12] (pp. 191-192). For optimized material-, temperature-, and bias current-parameters, saturated internal efficiency can be reached. Furthermore, optical cavities and a meandered shape, matching the mode size of an optical fiber, helped to outperform other detectors in terms of total detection efficiency [68].

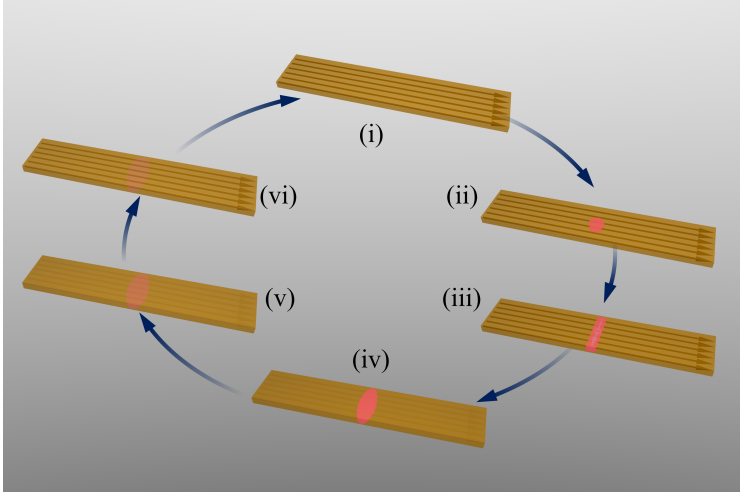

Figure 6.3: Schematic of the detection mechanism of an superconducting nanowire single-photon detector based on Reference [5] and [57] (pp. 8-9). The superconducting stripe is biased below its superconducting transition in (i). A photon absorption locally breaks the superconductivity in (ii). This forms a vortex crossing the wire in (iii), causing a wider collapse of the superconductive state in (iv). Due to a parallel resistor, the current flow through the detector is reduced and the normal resistive region decreases slowly in (v) and (vi).

6.1.2 Transition edge sensors

The transition edge sensor (TES) is a different type of superconducting detector. While the SNSPD relies on a local breakdown of superconductivity due to its geometry and current biasing, the TES uses the temperature dependent resistance curve between the fully superconductive and fully normal temperature state and acts as a microcalorimeter [57] (p. 33). To do so, the heat dissipation of the chosen materials and a sensitive voltage biasing are crucial. In Figure 6.4 a), the device resistance is shown for different temperatures which has a steep, but almost linear transition region. With the weak electron-phonon

interaction in tungsten, it is possible to overcome this transition with energy pulses in the higher electron-volt range which equal several absorbed 1550 nm-photons. Therefore, transition edge sensors have in contrast to SNSPDs an intrinsic energy resolution [80]. As the heat dissipation of transition edge sensors is slow, the energy-resolution of TESs can be used as a photon-number resolution [71] or spectral resolution. The latter is discussed in Appendix A.9.

To have precise control over the transition edge between the superconductive and resistive state, these detectors are operated at temperatures around 0.1 K or lower. Because every absorbed photon changes the temperature of the detector, the internal efficiency is 100 % [57] (p. 54). In addition to the required low temperatures, the small resistance changes have to be read out using an array of superconducting quantum interference device (SQUID) amplifiers. These amplifiers are also located in the cryostat and require a precise biasing. Due to their low noise and additional shielding from black body radiation at low temperatures, false counts are reduced. Furthermore, as measured TES traces are comparably slow, the detectors are often read out by recording not just a time stamp but the whole trace (see Figure 6.4 b), which enables additional filtering methods for false events based on signal shape, as described in Section 6.3.2.

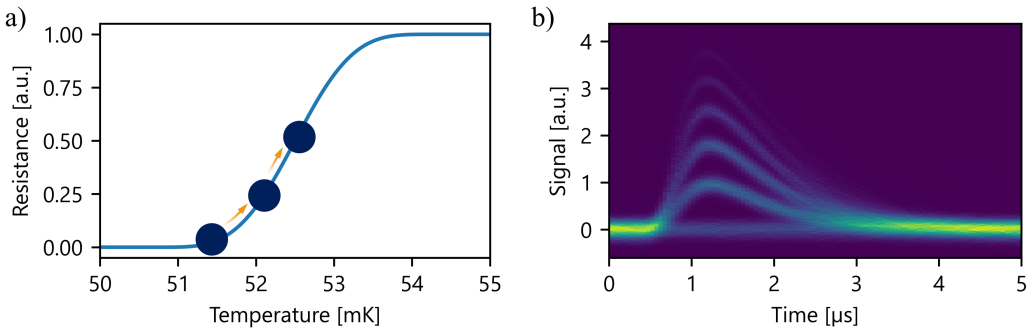

Figure 6.4: a) Resistance transition between the fully superconductive and normal resistive state based on Reference [57] (p. 34), and b) measured TES responses for different photon numbers for a fiber-coupled detector.

6.1.3 Integrated detectors

Compared to fiber-coupled detectors, integrated detectors come with new possibilities but also new challenges. While integration often enables better scalability and more flexibility, the material properties and fabrication steps can become more challenging. Especially surface roughnesses and lattice matching of the integration platforms and detector materials are important. In this thesis, only integrated detectors that are based on evanescent coupling from the integration platform to the integrated detectors are considered. This method is based on the fact that a guided waveguide mode partially lives in the surrounding of the waveguide due to a finite refractive index contrast between the

waveguide and its surrounding. Therefore, the mode confinement can lead to a spatial mode overlap between the waveguide mode and detection area, which corresponds to the collection efficiency, as explained in Section 6.1.1. Neglecting scattering at the waveguide-detector interfaces, an undetected photon remains inside the waveguide and can be detected by a second detector, or (in relation to this work) be interpreted and investigated as a manipulated quantum state after partial measurement. Therefore, an evanescently coupled detector can be described as a beam splitter with a detector in one output and the beam-splitting ratio given by the collection and absorption efficiency.

Over the last years, many groups have used evanescent coupling to integrate superconducting detectors on their waveguide platform. An overview is given in Table 6.2. While for example silicon and silicon nitride waveguides have the advantage of CMOS fabrication and provide an excellent mode overlap, their disadvantages lie in the integration of active optical components such as light modulators or switches due to a low χ^2-nonlinearity and their fiber-coupling efficiency for interfacing. The latter is also true for gallium arsenide, aluminum nitride, diamond, and lithium niobate on insulator. In general, it can be said that a higher mode confinement, which is beneficial for evanescent detection, is detrimental for fiber coupling. This can partially be compensated by tapers or tailored grating couplers. The earlier discussed titanium in-diffused lithium niobate waveguides, which are used in this work, have a weaker mode confinement, allowing for better fiber-coupling, as discussed in Section 4.3, but lower overlap between the evanescent field and the detector.

Table 6.2: Overview of different integration platforms and detector materials

Integration platform	SNSPD material	TES material
Silicon	NbN [81], NbTiN [82], WSi [83], MoSi [84]	
Silicon nitride	NbN [85], NbTiN [86], WSi [87]	
Tantalum pentoxide	NbTiN (Martin)	
Silica	WSi [88]	W [89]
Gallium arsenide	NbN [90]	
Alumininum nitride	NbN [91]	
Diamond	NbN [92], NbTiN [93]	
LNOI	NbN [94]	
Ti:LN	NbN [95], WSi [96]	W [97]

6.2 Integrated SNSPDs

The work on integrated superconducting nanowire single-photon detectors on titanium in-diffused lithium niobate waveguides can partially be found in Reference [96] and [50]. The fabrication process starts with the deposition of a 5 nm thin, amorphous tungsten silicide layer atop the waveguide sample using magnetron sputtering. Next, gold alignment markers are deposited using photolithographic structuring, aligned to the titanium in-diffused waveguides, and a subsequent lift-off process. With these gold markers, the spacing between four connected SNSPD-stripes with 400 µm length, 160 nm width and 160 nm spacing in a "w"-shape is written using e-beam lithography. After etching and removing the residual e-beam resist, the outer detector structure is formed using photolithography and subsequent etching. This process gives the final on-chip detector which is later bonded and connected to an electrical readout. While the individual detector length is limited to 400 µm due to the e-beam window, multiple detectors can be placed freely on the chip surface which directly points towards the scalability of integrated detectors. In addition, multiple in-line detectors can be used to increase the system detection efficiency. The design for on-chip SNSPDs is shown in Figure 6.5. On the fabricated samples, multiple of these waveguides per sample are investigated.

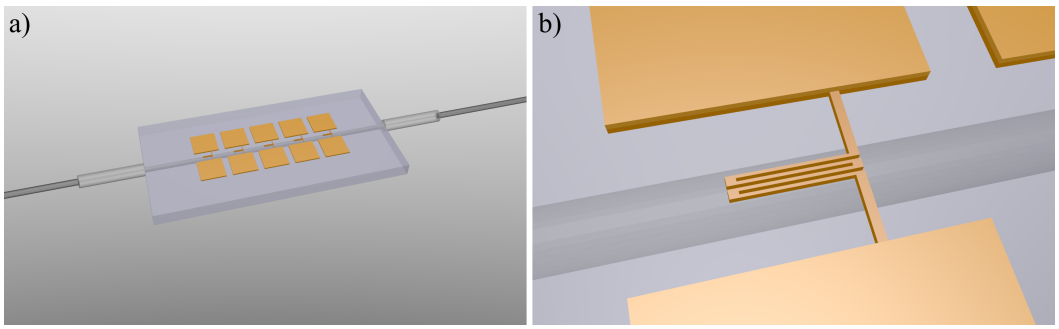

Figure 6.5: a) Superconducting nanowire single-photon detector design for integrated devices with five in-line detectors on a fiber-coupled sample, and b) inset on one of the detectors. The large gold areas represent bondpads usually in the range of 800 µm x 600 µmm enabling electrical contact of both sides of the integrated detector. The shown detector consists of four meandered, 400 µm long, and 160 nm wide tungsten stripes.

6.2.1 SNSPD simulations

As indicated in Section 4.1.1, we model the spatial waveguide modes in a titanium in-diffused lithium niobate waveguides using a commercially available mode-solving tool (Synopsis RSoft). With this, it is possible to investigate detector absorption using two- and three-dimensional mode simulations adding different structures and materials to the simulations. The ordinary refractive index of lithium niobate at different temperatures and wavelengths is based on a model from Edwards and Lawrence [98]. The extraordinary

refractive index is based on a model from Jundt [99]. For the refractive index distribution due to titanium in-diffusion a modified script provided by Synopsis Inc. is used which itself is based on equations by Strake et al. [100] and Korotky et al. [101]. We modified the the script based on empirical data to also take the surface profile of the waveguide samples into account, as well as the refractive index shifts at cryogenic temperatures. The resulting refractive index profiles for the two polarization modes are depicted in Figure 4.3. The refractive indices of additional dielectric layers and the different detector materials are provided by Varun Verma using ellipsometry measurements.

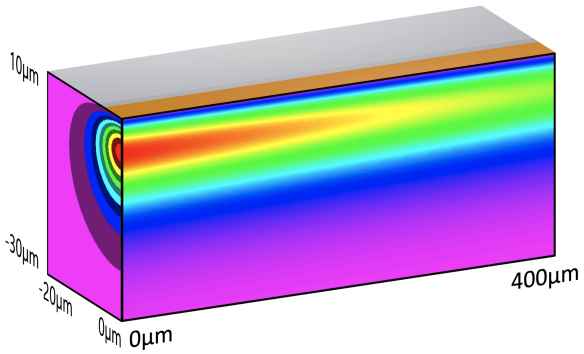

Figure 6.6: Three-dimensional illustration of the power decrease for a spatial mode traveling underneath an absorbing detector structure simulated in BeamPROP. The silver surface corresponds to the sample. The gold stripe illustrates the detector.

With the given geometries and refractive indices, we execute two-dimensional Finite Element Method (FEM) simulations, called FemSIM, or three-dimensional Beam Propagation (BeamPROP) simulations with the software. The latter is a Finite Difference Beam Propagation Method (FD-BPM) program, neglecting backwards-propagation and using only a semi-vectorial approach (treating the electric field as a vector not a scalar but with decoupled transverse field components). The detector segment cannot only be added and removed from the 3D simulation, but also its imaginary part of the refractive index and with it its absorption can be turned on and off. Therefore, also scatter can be investigated. An example of a 3D simulation using BeamPROP with an integrated detector is shown in Figure 6.6. Detector absorption can be calculated by comparing the mode intensity in front of and behind the detector.

FemSIM simulations provide a calculated spatial mode profile. Here, we directly calculate the expected detector absorption from the simulation results for the imaginary part of the effective refractive index [102] (p. 6). However, as these simulations can only be executed at a fixed position on the waveguide, it is not possible to include changes along the propagation direction using this method. Because of that, this method uses the assumption that changes to the spatial mode along the propagation direction are negligible. Here, only the BeamPROP simulations can include modal changes along the propagation direction excluding reflections. Therefore, we use them to directly investigate the propagation of light in a certain structure. BeamPROP simulations require higher computational power,

are more sensitive to numerical artifacts and are limited in the choice of measurement grids. On the other hand, they enable three-dimensional simulations. With these, modal changes along the waveguides can be investigated for the non-circular mode profiles shown in Figure 4.3. Because of that, both simulation types are used collectively to investigate the detector absorption of integrated superconducting detectors.

While for waveguides with smaller mode confinement (for example in silicon [81]) a 400 µm long detector would guarantee near unity collection- and absorption-efficiency, the weak mode confinement in titanium in-diffused waveguides drastically decreases the collection efficiency. For FemSIM simulations, we calculate an on-chip detection efficiency of 1 % for TE polarized light and 0.4 % for TM polarized light at 1550 nm wavelength for one 400 µm long detector based on the imaginary part of the simulated effective refractive indices.

While it is often sufficient to use a simulation grid of one tenth of the wavelength to overcome simulation artifacts, the maximum simulation grid is here upper bounded by the detector dimensions. FemSIM simulations can be executed on a non-uniform simulation grid using a higher precision in the detector area and a coarse grid at the area in the sample with a small titanium concentration. Due to simulation errors at the boundaries of the simulation window, the whole waveguide mode must be depicted. With the non-uniform grid, it is possible to overcome the discrepancy between the large micron-range mode size and nanometer high detector structures. In BeamPROP, due to limitations on the grid and the additional simulation extension into the traveling direction (3D simulation), it is not possible to execute these simulations on a fine enough grid with more than two datapoints per height element inside the detector. This decreases the credibility of BeamPROP simulations of the exact detector structure for integrated SNSPDs on titanium in-diffused waveguides, resulting in a relative error greater than 100 % when executing convergence tests on different simulation grids. Nevertheless, we exploit BeamPROP simulations when investigating integrated TESs in Section 6.3.1.

6.2.2 SNSPD flood illumination

After detector fabrication on a lithium niobate waveguide, the devices are investigated without light coupling through the waveguide. This includes resistance measurements at room temperature and cryogenic temperatures, and flood-illumination tests, measuring detector responses from a distant light source as depicted in Figure 6.7. For this, a pulsed 1550nm light-source is attenuated such that an average mean photon number in the single-photon regime (mean photon number between 0.1 and 2) is detected by the device under test inside a cryostat. If the mean photon number is set too low, the signal-to-noise ratio decreases. If the mean photon number is set too high, the high occurrence of multi-photon events and low occurrence of pulses of zero photons also reduces the measurement accuracy. Then, we record the detector outcomes in synchronization with a timestamp of the pulsed laser. In the exemplary measurement results in Figure 6.8 b), we detect a maximum count rate of 100000 counts per second while using a laser repetition rate of 500 kHz. This experiment is executed for different detector bias conditions and

can give insight into detector parameters such as the shape of a detector response, the internal efficiency, timing jitter, and recovery time, which are all independent of coupling direction.

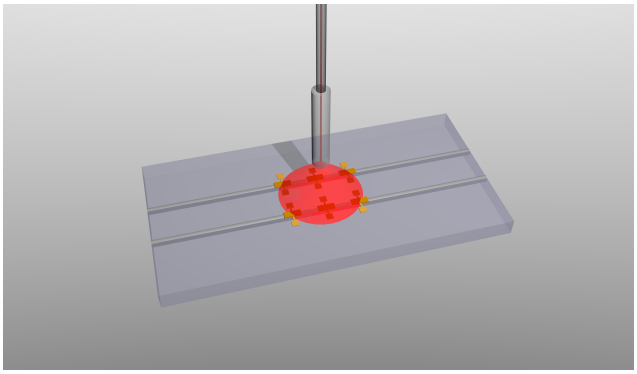

Figure 6.7: Schematic of a flood illumination experiment using a fiber pointing towards the integrated detectors. The red cone represents the laser spot, illuminating the sample.

A low collection efficiency can be compensated by elongating the detector, a stronger mode confinement, or in-line detector-multiplexing. On the contrary, a low internal efficiency directly corresponds to photon loss, as the photon is annihilated but not measured. Therefore, a high and stable internal efficiency is of great importance for quantum optics experiments. Due to the detection mechanism of SNSPDs, the probability of a photon with a certain energy causing a breakdown of the superconductivity and with it a detection event depends on the bias current. With too low bias current, the energy of a 1550 nm photon is not sufficient to cause a detection event. If the bias current is too high, small fluctuations in the current can increase the dark count probability up to the point where the bias current exceeds the critical current and the detector stays in the normal resistive state. In between, the probability of creating a detection event from a photon increases with bias current (probabilistic regime). At a fixed wavelength of 1550 nm, it is possible to saturate this probability (depending on the detector fabrication) and to reach a plateau where the internal efficiency is independent of the explicit value of the bias current. This directly corresponds to a saturation of the internal efficiency and is a sign for low constrictions in the detector fabrication [57] (p. 9). A high surface roughness or material inhomogeneities can hinder such a plateau.

To execute a flood illumination measurement, we bond and electrically connect an integrated SNSPDs in a helium sorption cryostat, reaching a base temperature of 0.77 K. Additional shielding inside the cryostat is not just beneficial for reaching this temperature in a closed-cycle system but also to minimize unwanted counts from black-body photons. The lithium niobate sample is glued to the sample holder using vacuum grease which gives a good temperature connection without causing strain from the temperature changes. For the e-beam written tungsten silicide SNSPD, we measure detector responses as shown in Figure 6.8 a), showing that the device responds to 1550 nm photons. When counting these photons by counting how often the electrical signal crosses a threshold in a time tagger, we

investigate the internal efficiency. The threshold level is set to 50 % of the maximum peak height of the detector response on the rising edge to minimize timing jitter. The results for the number of counts per second with the pulsed laser on and off (for dark-count measurements) are plotted in Figure 6.8 b). It can be seen that photon detection is very unlikely below a bias current of 1.5 µA and that there is a long plateau between 2.5 µA and 6.5 µA before latching (remaining in a fully resistive, non-functional state after photon absorption). This shows that it is possible to saturate the internal efficiency of integrated SNSPDs on lithium niobate waveguides.

While only a full quantum detector tomography [9] or the usage of a single-photon source can verify pure single-photon sensitivity, we assume based on the comparison with other single-photon sensitive SNSPDs that also the integrated SNSPDs are single-photon sensitive as we only use an attenuated pulsed laser that intrinsically contains multi-photon contributions.

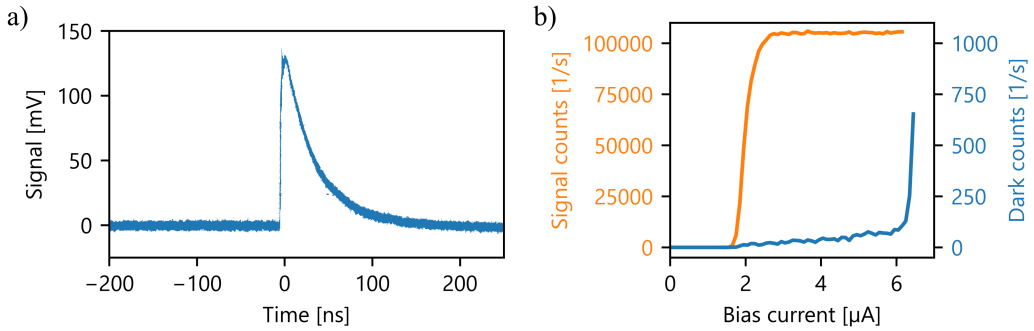

Figure 6.8: a) Detector response after photon absorption for an integrated superconducting nanowire single-photon detector, and b) measured number of counts per second over the bias current with a 1550 nm pulsed laser in orange as well as dark count measurements in blue.

6.2.3 SNSPD loss characterization

Using light propagation through a waveguide, we use a loss characterization as described in Section 4.1.2 to characterize detector absorption but also loss increase due to fabrication steps when depositing integrated detectors. As the waveguide endfaces are not influenced by additional detectors on the waveguide, the endface reflectivity and waveguide dimensions stay the same before and after detector fabrication. A general loss increase for example due to etching steps in the detector fabrication would also have an effect on adjacent waveguides with no detectors. Therefore, an overall loss increase on those waveguides gives insight on the influence of detector fabrication, while loss increase on waveguides with detectors gives insight on the effect of light hitting the integrated detectors. It has to be pointed out that this method can only measure the loss increase due to an on-chip detector, but not differentiate between detector absorption and scatter.

Only the former would lead to a successful detection event. Therefore, the latter has to be minimized which we investigate with the earlier introduced simulations and following detection-efficiency characterization.

For the investigated samples with integrated SNSPDs, the overall waveguide loss for waveguides without detectors increased from 0.03 dB/cm ± 0.01 dB/cm to 0.20 dB/cm ± 0.08 dB/cm for both polarization modes on the investigated sample. We calculate the uncertainty from the standard deviation of 14 characterized waveguides without detectors. It is expected that especially small damage at the endfaces of the sample causes the loss to increase. This can be investigated by additional polishing steps and subsequent loss characterization. However, as polishing the chip carries the risk of damaging the detectors, it is deliberately avoided on the investigated sample. Therefore, we cannot exclude a loss increase of 0.17 dB/cm ± 0.08 dB/cm caused by the detector fabrication steps at this stage.

For waveguides with five in-line SNSPDs we measure an additional transmission-loss increase. Here, the measurement with TE polarized light shows additional loss of 0.07 dB/cm ± 0.03 dB/cm and the measurement with TM polarized light shows a loss increase of 0.02 dB/cm ± 0.01 dB/cm for 18 investigated waveguides. Distributing this additional loss increase over the five detectors per waveguide leads to an expected detection efficiency of 0.6 % ± 0.3 % in TE polarization and 0.2 % ± 0.1 % in TM polarization. Comparing these results to the simulation results from Section 6.2.1 (a detection efficiency of 1 % in TE polarization and 0.4 % in TM polarization) suggests an overestimation of the simulated detection efficiency. However, the expected low detection efficiency is confirmed in both cases.

6.2.4 SNSPD efficiency characterization

When characterizing the detection efficiency, one usually carries out a measurement of the system detection efficiency (SDE) which is normally defined as the ratio between an input mean photon number at a certain interface (for example a fiber connection) and the detected mean photon number. For integrated detectors the interface corresponds to a fiber connection before the fiber-to-chip interface. With this, in contrast to the on-chip detection efficiency, fiber-to-chip coupling loss is included which is closer to general applications including off-chip sources. There are many ways to estimate the on-chip detection efficiency from the system detection efficiency. One example is the usage of an additional chip-to-fiber control port to differentiate coupling loss, or using multiple input ports. In close relation to the circuit design in this work, we can estimate the on-chip detection efficiency from a known fiber-to-chip coupling. Using both endfaces as an input port and multiple detectors on a waveguide, the different detector responses can be used to differentiate between the number of evanescently coupled photons and detected scattered photons. Therefore, also the total throughput through the sample and both fiber-chip-interfaces must be investigated. Besides measuring the total throughput through the sample and the individual detector responses, a precise measurement of the input mean photon number is a critical part.

Input state calibration

For this work, we use two different methods for calibrating the input mean photon number. The ***attenuator method*** requires one calibrated reference detector and is based on the assumption of a linear behavior of a variable optical attenuator (VOA) also at the single-photon level [67]. The setup is shown in Figure 6.9. Using a reference detector and different attenuator settings, a linear correlation between the attenuation setting and the mean photon number is used to infer the impinging mean photon number on the device under test (DUT). For this method, it is advantageous but not necessary to utilize a reference detector which is calibrated at the same range of photon numbers to minimize the uncertainty based on the assumption of the linear attenuation behavior.

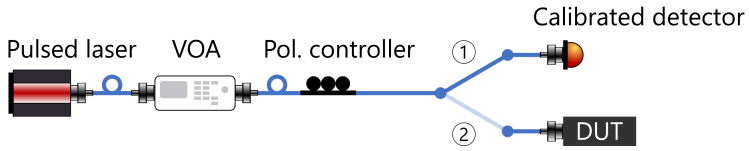

Figure 6.9: Optical setup for the attenuator method to calibrate the impinging mean photon number at a device under test (DUT) using one variable optical attenuator (VOA) and one calibrated detector. Component drawings are partially taken from Reference [37].

The ***splitting-ratio method*** requires (in contrast to the attenuator method) two calibrated reference detectors with a wide dynamic range [97, 103]. However, both calibrated reference detectors do not have to work at the single-photon level. The setup is shown in Figure 6.10. Here, first, the ratio between the two detectors is precisely set and measured using a low attenuation on VOA1 and a high attenuation on VOA2. Then, the attenuation on VOA1 is increased to reach the single-photon level at the second detector or device under test, respectively. This method does not require any assumptions on the attenuators (including a linear attenuation behavior) besides temporal stability. In addition, it is possible to include fluctuations in the laser power as this can be monitored by detector 1 during the whole data acquisition.

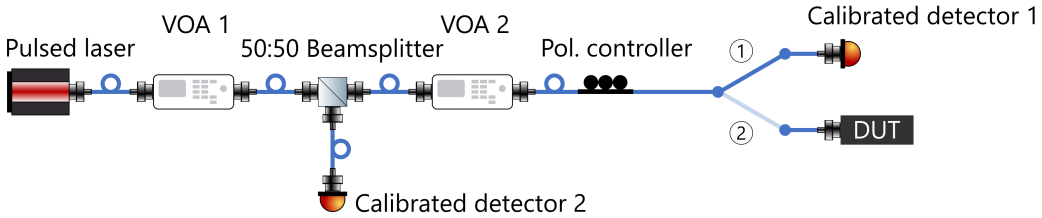

Figure 6.10: Optical setup for the splitting-ratio method to calibrate the impinging mean photon number at a device under test (DUT) using two variable optical attenuators (VOA) and two calibrated detectors. Component drawings are partially taken from Reference [37].

With both methods, it is possible to calculate the impinging mean photon number for a system detection efficiency measurement. The method of choice depends on the availability of calibrated single-photon detectors or wide dynamic range attenuators. For the

characterization of integrated SNSPDs, we chose the attenuator method while we apply the splitting ratio method in Section 6.3.4 for integrated TESs.

Using a calibrated click detector as the reference, we assume Poisson statistics from a coherent laser source to transform click probabilities to photons per pulse and mean photon numbers. As an example, the probability of detecting exactly one photon at a mean photon number of $\bar{n} = 1.5$ is $p_1 = 1.5\mathrm{e}^{-1.5} = 33.47\,\%$ and detecting not zero photons is $p_{k\neq 0} = 1 - p_0 = 1 - \mathrm{e}^{-1.5} = 77.69\,\%$. These values can then be compared to the obtained measurement results from the device under test. Using multiple, overlapping coherent states, one can even execute a full quantum detector tomography which gives insight into nonlinear responses of a detector [9, 10]. For calculating the on-chip detection efficiency, interface loss and photon absorption from other inline detectors must be considered.

System detection efficiency measurement

With the results from SNSPD simulations in Section 6.2.1 and loss characterization in 6.2.3, we expect the detection efficiency to be small even though the internal efficiency is saturated. As additional imperfections can lead to deviations of the actual system detection efficiency from these estimations, we execute a full characterization of the SDE. For this, we pigtail both sides of the straight waveguides, as sketched in Figure 6.5 a), using the technique described in Section 4.3. At room temperature we measure a coupling efficiency of 48 % ± 1 % per interface. This relatively low pigtailing efficiency can either come from a misalignment during the curing process of the UV-glue or also by a nonideal sample endface as already suggested in the previous section. We monitor the optical throughput through the sample during a cooldown after pigtailing where the power dropped linearly. At cryogenic temperatures, it is not possible to measure the individual coupling efficiencies for each endface but just the total throughput. Assuming no additional loss-increase besides a misalignment of the fibers, a minimum throughput per interface can be calculated to be 26 % ± 3 %. At this cooldown, only two wired-up detectors responded to single photons, due to pyroelectric damage, explained in Section 6.2.5.

We investigate the detection efficiency for the two detectors with photons coming from each fiber connection and in both polarization modes. A crucial factor when investigating the system detection efficiency is the differentiation between a scattered photon (for example coming from the fiber connection) and a photon that is traveling through the waveguide and is evanescently coupled. Both cases contribute to the system detection efficiency. In fact, it is possible to achieve a relatively high system detection efficiency with no photons traveling through the waveguide as long as the scattering center is close to the detector. Therefore, only the investigation of multiple in-line detectors, polarization dependence and bi-directional waveguide coupling can verify evanescent coupling. This is further elaborated in Table 6.3 and can be expressed with the equation

$$\eta_{\mathrm{SDE},i} = \eta_{\mathrm{fc1,2}}(1-\alpha_{\mathrm{wg},i})(1-\eta_{\mathrm{det}})^{N-i}\eta_{\mathrm{det}} + (1-\eta_{\mathrm{fc1,2}})\eta_{\mathrm{scat},i}, \tag{6.1}$$

where $\eta_{\mathrm{SDE},i}$ is the system detection efficiency for detector i, $\eta_{\mathrm{fc1,2}}$ is the fiber-to-chip coupling efficiency of the utilized input side, and $\alpha_{\mathrm{wg},i}$ is the waveguide loss depending on the distance between the endface and the detector. As all detectors on one waveguide have the same design, we assume the on-chip detection efficiency η_{det} to be the same for all N detectors. $\eta_{\mathrm{scat},i}$ includes the probability of detecting a photon which was initially scattered at the fiber-to-chip interface. Therefore, $\eta_{\mathrm{scat},i}$ decreases drastically with the distance between this interface and detector i.

For the investigated on-chip SNSPDs, the detection efficiency is polarization sensitive while the total throughput through the sample and with it the fiber coupling is not. In addition, the expected behavior for the dependence on the input direction as well as the position in the in-line design suggests evanescent coupling from the waveguide to the on-chip detectors. We calculate the on-chip detection efficiency per detector to be 0.7 % ± 0.2 % and 0.10 % ± 0.03 % for two different polarization orientations. For this, all waveguide losses are neglected. Using an input mean photon number of $\bar{n} = 1.50 \pm 0.08$ and a repetition rate of 500 kHz, the highest observed detector countrates (measured over one minute) are (1320 ± 5) counts per second for the second and (1280 ± 5) counts per second for the second last in-line detector. Minimizing the countrate using a polarization controller, both detectors show (200 ± 1) counts per second. Based on the description in Table 6.3, η_{scat} in Equation 6.1 is set to zero. The influence of dark counts can be neglected as all measurements are executed in synchronization with a laser-synchronized trigger and 8 ns wide coincidence window.

As no polarization-maintaining fibers are used, it is not possible to directly assign these detection efficiencies to the TE and TM polarization modes. However, comparisons to the loss characterization and simulation results suggest that the higher on-chip efficiency corresponds to TE polarized light.

The independent investigations of the detection efficiency (using simulations, loss characterization, and a direct measurement efficiency characterization) show detection efficiencies per device of 1 %, 0.6 % ± 0.3 %, and 0.7 % ± 0.2 %, respectively. While the agreement of these measurement results is satisfying, the efficiency itself is low compared to nanophotonic integration platforms. All in all, we can proof that integrated SNSPDs on titanium in-diffused lithium niobate waveguides were successfully realized.

Table 6.3: Comparison of the dependence on different parameters for scattered photons and evanescently coupled photons, detected by an on-chip detector.

Dependence	Scattered photon	Evanescently coupled photon
Fiber coupling efficiency	Antiproportional, when fiber connection equals scattering center	Proportional
Input direction	Decreases with distance to scattering center	Independent, when excluding other in-line detectors
Polarization	Independent, when fiber coupling is polarization independent	Depends on individual waveguide modes

6.2.5 Pyroelectric damage

Due to the great scalability of integrated optics, low on-chip detection efficiencies can be compensated by in-line detector multiplexing as long as the low efficiency is attributed to a small collection efficiency and therefore an undetected photon still remains inside the waveguide. For the calculated detection efficiency of 0.7 %, one would need at least 99 detectors to reach a combined on-chip detection efficiency of 50 % as

$$1 - (1 - 0.7\,\%)^{99} = 50\,\%. \tag{6.2}$$

This is problematic, as these detectors would need a 40 mm long sample just for detection and high requirements on the cryostat due to the heat dissipation when wiring-up all detectors individually. Therefore, additional design changes to the detector are required to increase the detection efficiency.

In addition, another challenge emerged when investigating on-chip detectors on lithium niobate. While the fabrication yield of the on-chip devices is very good and could potentially enable the deposition of hundreds of detectors, a lot of them are damaged during the cooldown process. Covering the work on multiple detector designs and multiple lithium niobate samples that where partially used to explore this damage, only 18 out of 62 detectors survived at least one cooldown. This was monitored by measuring the resistance of the devices.

As lithium niobate is pyroelectric, electrical charges build up during the cooldown [104–106]. While these charges can dissipate and annihilate under atmosphere conditions, this is less possible under vacuum [105]. Micrographs of a WSi structure on lithium niobate, as shown in Figure 6.11, taken after one temperature cycle down to 0.1 K and back, suggest an electric discharge through the on-chip device causing the nanowires to explode.

This effect which we also observe using molybdenum silicide detectors reduces the yield of functional on-chip detectors on lithium niobate at cryogenic temperatures. While it might be possible to overcome this problem by investigating different detector geometries

or the usage of additional conductive layers in future work, one has to pay attention to not lose the saturated internal efficiency and induce loss.

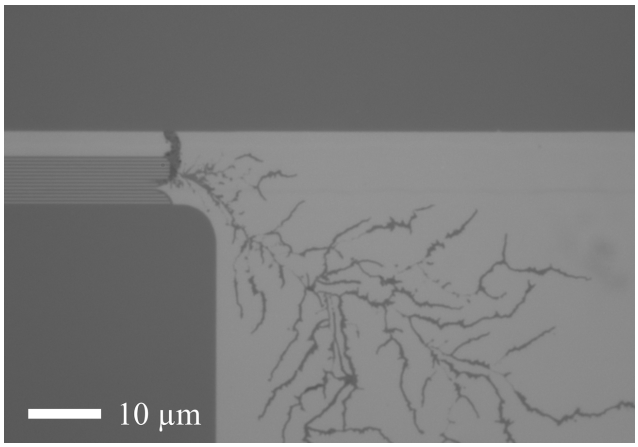

Figure 6.11: Micrograph of a WSi contact pad on lithium niobate after one cooldown showing pyroelectric damage.

6.3 Integrated TESs

The work on integrated transition edge sensors on titanium in-diffused lithium niobate waveguides can partially be found in Reference [96] and [97]. As already visualized in Table 6.2, integrated transition edge sensors are less investigated on integrated devices, mainly due to the higher system requirements in the form of lower temperatures and SQUID-readout. For this detector type, the same characterization methods are executed as for the integrated SNSPDs.

Transition edge sensors can be deposited on lithium niobate using magnetron sputtering and subsequent photolithographic structuring. With this, we place a homogeneous amorphous tungsten layer directly on top of the waveguide [96, 97]. As the dimensions for TESs are normally in the two-digit micrometer size for width and length, and 20 nm to 40 nm for the height, the waveguide surface roughness is less critical compared to the earlier discussed integrated SNSPDs. In addition, this leads to lower room temperature resistances, making them more robust against pyroelectric damage. For this work, different TESs geometries, inspired by Reference [107] and Reference [108], are investigated as depicted in Figure 6.12, all with a height of 20 nm.

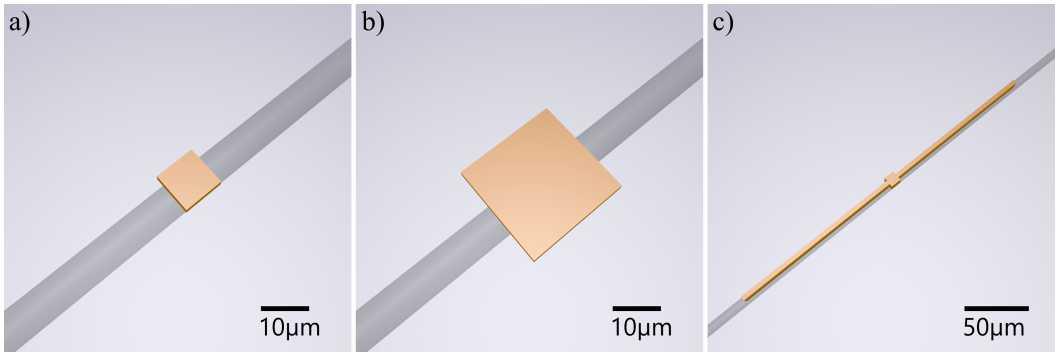

Figure 6.12: Transition edge sensor (TES) dimensions of tested integrated devices: a) 10 µm x 10 µm x 20 nm TES, b) 25 µm x 25 µm x 20 nm TES, and c) 10 µm x 10 µm x 20 nm TES core with two 150 µm x 4 µm x 20 nm TES fins

6.3.1 TES simulations

As described in Section 6.2.1, we first investigate the different structures in computer simulations. The simulated absorption results are shown in Table 6.4. From the results, we see that the overall absorption efficiency of the different on-chip TESs is again small for both polarization orientations. This can be explained by the small mode overlap as discussed earlier. Furthermore, the different outcomes for TE and TM polarization can be explained by the small difference in mode confinement and mode height compared to the sample surface due to differences in titanium in-diffusion for the different crystal orientations as well as differences in the interaction of the two polarization directions with the material. As the two independent simulation methods (FemSIM and BeamPROP) agree very well, we assume interface reflections and mode changes during the propagation to be negligible. In addition, assuming perfect waveguiding, all loss can be attributed to detector absorption. Comparing the different detector geometries, the core-with-fins structure leads to the highest absorption due to the biggest longitudinal overlap. Analog to SNSPDs, multiplexing or elongating the detection area can already be considered as one possibility to increase the absorption efficiency as also shown in Reference [107].

Table 6.4: Simulation results using FemSIM and BeamPROP. Based on convergence tests and variations in the input simulation parameters, the uncertainties are expected to be in the 0.1 % range.

TES geometry	TE FemSIM absorption [%]	TE BeamPROP absorption [%]	TM FemSIM absorption [%]	TM BeamPROP absorption [%]
10 µm square	0.1	0.1	0.6	0.5
25 µm square	0.2	0.2	1.5	1.4
Core with fins	1.1	1.0	10.3	9.9

6.3.2 TES flood illumination

To test the photon response, the on-chip detectors are wire-bonded, connected to superconducting quantum interference devices (SQUIDs) and cooled down below 0.1 K. At this temperature the detectors are superconductive. Then, flood illumination tests are executed as described in section 6.1.2 For this, the individual detector outcomes are recorded. This measurement was executed by Thomas Gerrits at NIST. When overlaying the laser timestamps, each detector shows multiple outcomes which differ in their shape and height, similar to Figure 6.4 b). We sort all collected detector responses (traces) of a single detector in a histogram. While the maximum peak height is an obvious parameter for this sorting, we implement an improved method using the information of the whole trace based on a Wiener filter [109]. Here, an average trace is calculated and convoluted with each trace. This way, the whole trace-shape and not just the maximum peak height is used to sort the detector outcomes. It enables a higher resolution and an additional post-process temporal filter of detection events resulting from black body radiation which are uncorrelated to the laser timestamp. As we use a single-wavelength laser at 1550 nm (corresponding to 800 eV), the different detector outcomes must come from different photon numbers per pulse. The individual detectors are placed at different positions on the chip and therefore see different portions of the distant light source (see Figure 6.7), hence a calculated mean photon number from the histograms is no meaningful figure of merit under flood illumination. We calculate the energy resolution and uncertainty on the measured photon numbers per pulse from the full-width-half-maximum (FWHM) of the histograms. In Figure 6.13, it can be seen that this FWHM is smaller for the smallest 10 µm-square detector and broadens for the detectors with additional fins. One explanation is the different heat conductivity between the detector and lithium niobate sample which is geometry-dependent. In addition, a small shoulder can be seen on the 10 µm-square device. This shoulder is a known phenomenon for small TESs and can be caused by photons that "*interact with the voltage bias rails rather than the central part of the sensor*" [80]. This phenomenon becomes more prominent for smaller detectors. The bigger 25 µm x 25 µm detector shows a poorer photon-number resolution (energy resolution) as the individual peaks overlap more. For the detector with

additional fins, it can be seen that less photons were detected by the device, as no detector traces corresponding to higher energies or photon numbers are visible. While we can fully attribute this to the detector geometry and placement of the flood-illumination fiber, it can also be seen that the energy resolution is further reduced.

The measurement results prove that all detector geometries can be used as on-chip single-photon detectors. However, combining these results with the earlier shown simulation results, there is a trade-off between detector absorption (detection efficiency) and energy resolution (photon-number resolution). During several temperature cycles down to cryogenic temperatures for flood illumination, no sign of detector damage due to pyroelectricity was recognized.

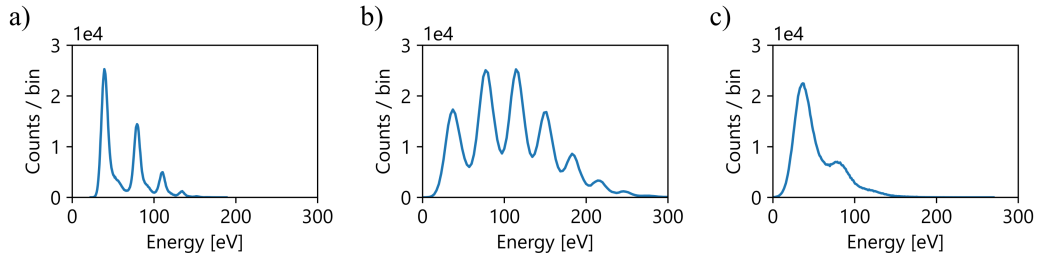

Figure 6.13: Flood illumination histogram plots showing the energy resolution for different transition edge sensor (TES) geometries: a) 10 µm x 10 µm x 20 nm TES, b) 25 µm x 25 µm x 20 nm TES, and c) 10 µm x 10 µm x 20 nm TES core with two 150 µm x 4 µm x 20 nm TES fins.

6.3.3 TES loss characterization

We execute a loss characterization to investigate and compare loss increase due to detector fabrication and loss increase due to the on-chip detectors, as described in Section 6.2.3. For detectors without fins, the detection absorption is too small to make a significant statement. On the contrary, waveguides with multiple deposited TESs with fins show a significant loss increase. The results for a lithium niobate waveguide sample with integrated TESs, shown in Table 6.5, were presented in my MSc. thesis [110] and Reference [96]. Calculating the loss increase per detector and attributing all loss increase to detector absorption, this gives an estimated detection efficiency of (0.9 ± 0.7) % in TE polarization and (13 ± 2) % in TM polarization for TESs with fins, matching the simulation results in Section 6.3.1. As detectors without fins perform better under flood illumination but show no measurable loss increase, we execute a full proof-of-principle detection efficiency characterization, as described in Section 6.2.4, to estimate the detection efficiency.

Table 6.5: Loss characterization results for integrated TESs with fins based on Reference [110] and [96].

Waveguide type	Loss in TE polarization [dB]	Loss in TM polarization [dB]
Waveguides with no detectors	0.24 ± 0.04	0.3 ± 0.1
Waveguides with three detectors	0.29 ± 0.03	0.96 ± 0.05
Waveguides with five detectors	0.34 ± 0.03	1.70 ± 0.05

6.3.4 TES efficiency characterization

To investigate the detection efficiency and how the TES responds to evanescently coupled photons in general, we fiber-couple both endfaces of the lithium niobate sample with multiple TESs integrated on a straight waveguide to provide optical access to the waveguide at cryogenic temperatures. This work was done in collaboration with Thomas Gerrits at NIST. As the detectors are very sensitive to black body radiation and stray light, additional shielding and even colder temperatures of 0.01 K in a dilution refrigerator are used for the efficiency characterization. The same fiber-coupling technique as used in Section 6.2.4 is used again. We achieve a total transmission of 43 % through the whole sample. This transmission value contains fiber and waveguide loss (which are further neglected), two FC/FC fiber couplers, loss due to endface reflections, loss due to imperfect mode-matching, and alignment loss at both endfaces. The waveguide, chosen for detector efficiency characterization, has three 25 µm x 25 µm x 20nm TESs deposited onto it. Although these detectors show no significant loss increase caused by the missing fins as described in Section 6.3.3, they are chosen because of their distinct energy resolution as shown in Section 6.3.2. One of the detectors is depicted in Figure 6.14 a).

Two of the three detectors with equal dimensions are electrically connected to SQUID amplifiers. Due to the surface guiding waveguides, the glue connection between the fiber and waveguide endfaces are not symmetric, as shown in Figure 6.14 b). Therefore, glue contraction due to temperature changes misaligns the system and reduce the transmission. This effect can be overcome by a more complex gluing technique based on the same principle but using additional counter pieces on the sample surface [110]. As the sample surface is a critical part for integrated detector, the simpler and less temperature-stable connection is chosen here. After fiber splicing both pigtail fibers to fiber feedthroughs in the cryostat, the sample is cooled to a stable base temperature of 0.01 K. Here, we measure a polarization-insensitive transmission trough the waveguide chip of (8 ± 2) %. We attribute the drop in transmission to the glue contraction. Assuming both endfaces to have nearly equal coupling efficiencies, the fiber-coupling efficiency for each side is calculated to be 28 % at 0.01 K. Despite the transmission drop, this value is still comparable to other work shown in Table 6.2.

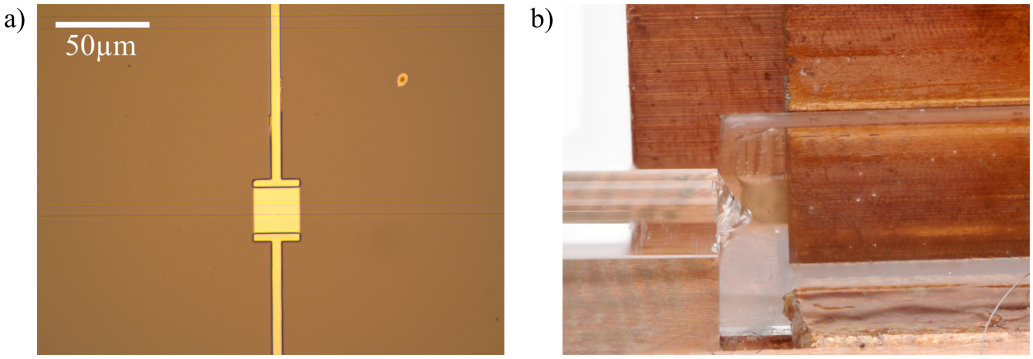

Figure 6.14: a) Microscope image of an integrated 25 µm x 25 µm x 20 nm tungsten transition edge sensor on a 6 µm wide lithium niobate waveguide, and b) focus stacked image of the fiber-to-chip connection. Here, one can see the asymmetric glue joint which can cause misalignment during temperature changes.

We investigate the detection efficiency for both incoupling directions as well as both electrically connected detectors, and both optical polarizations that are guided by the waveguides. We record the individual detector responses after adjusting and measuring the input mean photon number. As two calibrated detectors were available for this measurement, we use the splitting-ratio method as described in Section 6.2.4. Figure 6.15 shows the different traces corresponding to different photon numbers from one integrated TES.

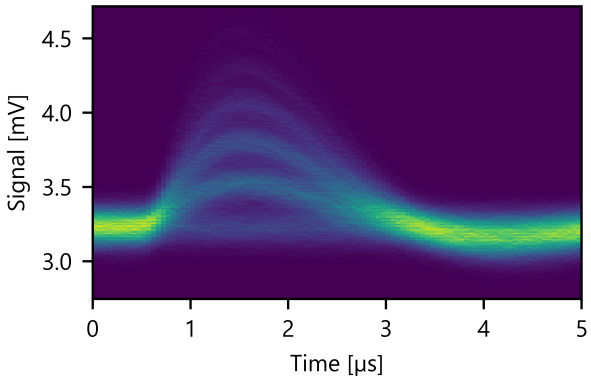

Figure 6.15: Heatmap plot of measured detector responses with different peak heights corresponding to different photon numbers per pulse for an integrated transition edge sensor.

For each setting, we record and evaluate 819200 traces, as discussed in Section 6.3.2. We sort the results in histograms and compare them to a Poisson distribution, resulting in a derived mean photon number for each incoupling direction, detector, and polarization, as shown in Figure 6.16. While the influence of the incoupling direction is negligible and the influence of the individual detector on the waveguide lies within the measurement accuracy of the calculated mean photon number, the influence of the polarization setting is critical.

Together with the impinging mean photon number, the system detection efficiency is calculated to be (0.23 ± 0.04) % and (0.19 ± 0.04) % for the two detectors for one polarization orientation, and (0.06 ± 0.01) % and (0.07 ± 0.01) % for the other polarization orientation. Similar to Section 6.2.4, we can assign the efficiency values for the two polarization settings to the polarization modes TM and TE, based on loss characterization and simulation results. As the total transmission is polarization insensitive, the measurement results must be attributed to evanescent coupling which agrees well with our simulations and loss characterization following the relations in Table 6.3. If the detection events would come from scattered photons, the incoupling direction and position of the individual detectors would have a bigger influence and can therefore be neglected. The results can be seen as a proof-of-principle for integrated TESs on lithium niobate waveguides and evanescent coupling verification.

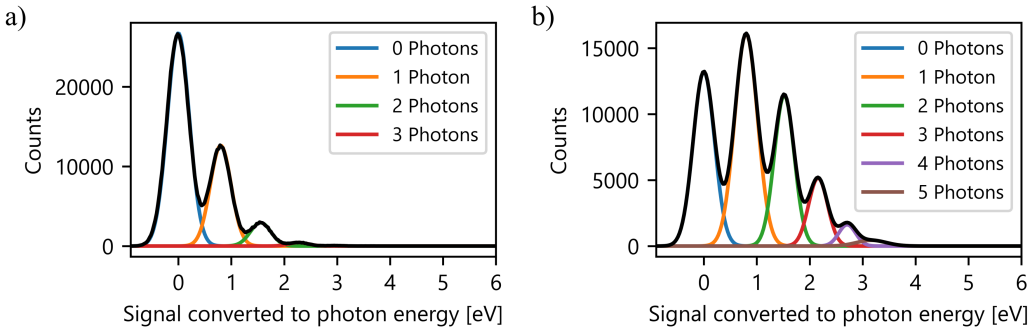

Figure 6.16: Histograms of the evaluated detector responses of an integrated transition edge sensor converted to the underlying photon energies for one detector in black and Gaussian fitting for the individual peaks in a) TE polarization and b) TM polarization.

Conclusion and Outlook 7

In this work, we explored the different elements for creating measurement-induced nonlinearities. We showed that interesting quantum states can be created by combining the interference of a single photon and coherent state with a subsequent measurement operation in the form of a photon subtraction. By using state-of-the-art technologies such as SPDC single-photon sources, integrated optical circuits, and superconducting detectors, the findings of this work can be understood as proof-of-principle experiments for creating complex photon-number correlations between two modes. Furthermore, we investigated the integration of superconducting detectors on titanium in-diffused lithium niobate waveguides as integrated detectors provide the potential for a more compact and more efficient realization of the presented schemes.

The theoretical simulations point out the great potential for creating complex multi-photon states as two-mode squeezed vacuum and exotic two-mode states with complex correlations. Especially, as other methods require high pump powers or multiplexing of different sources, the shown circuit designs can be very effective in that sense. The good agreement of simulations with included photon loss and experimental results suggests an extensive understanding of the developed scheme.

Nevertheless, the experimental realization can still be optimized. With the available laser systems and nonlinear crystal, strong filtering was necessary to match the optical spectra of the input states, inducing high loss. In addition, the combination of the utilized photon source and detectors hindered the exploration of higher photon numbers. Here, the switch to a more suitable laser system can drastically improve the visibility of interference and measurement-induced effects. In addition, it enables us to use time-multiplexed (quasi-)photon-number resolving detectors with a longer recovery time.

The fabricated integrated circuits have proven to be well suited for these complex experiments. Multi-channel beam splitter structures can be fabricated with optical lithography. This technique provides great flexibility and long term stability for different integrated circuit designs. We showed that waveguiding loss is almost negligible, and different beam-splitting ratios can be realized. In addition, the measured multi-channel fiber-coupling efficiency of 77 % provides an efficient solution for easy to use transitions from freespace optics to fiber-coupled and on-chip setups.

Regarding the investigations of integrated superconducting detectors, it was possible to measure detector responses to single photons for both detector types, superconducting nanowire single-photon detectors and transition edge sensors. In addition, evanescent coupling was confirmed. Despite a high fabrication yield, SNSPDs were often damaged during the cooldown process due to pyroelectric discharge in lithium niobate. Furthermore,

the on-chip detection efficiency for the investigated detector designs for both detector types was low. While it was possible to attribute this to a low collection efficiency, the detector design must be further optimized before combining detectors with more complex integrated circuits.

The usage of state-of-the-art technologies comes with the advantage that an ongoing optimization of the individual technologies simultaneously improves the presented experiments and vice versa. As an example, the recent demonstrations of photolithographically written micron-wide SNSPDs [111, 112] are a promising solution for high-efficient integrated detectors in microphotonics due to stronger evanescent coupling. Therefore, the further developments of the presented work will drastically benefit from these improvements.

Besides experimental improvements, a quantitative measure for measurement-induced nonlinearity must be found. As the discorrelation parameter introduced in Reference [23] is not applicable and the measurement of the maximum induced two-mode squeezing suggested in Reference [24] is challenging, finding a comprehensive quantifier is a question for further research.

Looking forward, the combination of an active integration platform and superconducting detectors provides the opportunity for a further extension of the scheme, following the increasing demand for multi-photon quantum states in various quantum optics applications.

Bibliography 8

[1] L. D. P. Smullin and G. Fiocco, Optical echoes from the moon, Nature **194**, 1267 (1962).

[2] G. G. Taylor, D. Morozov, N. R. Gemmell, K. Erotokritou, S. Miki, H. Terai, and R. H. Hadfield, Photon counting LIDAR at 2.3 μm wavelength with superconducting nanowires, Optics Express **27**, 38147–38158 (2019).

[3] E. Agrell, M. Karlsson, A. R. Chraplyvy, D. J. Richardson, P. M. Krummrich, P. Winzer, K. Roberts, J. K. Fischer, S. J. Savory, B. J. Eggleton, M. Secondini, F. R. Kschischang, A. Lord, J. Prat, I. Tomkos, J. E. Bowers, S. Srinivasan, M. Brandt-Pearce, and N. Gisin, Roadmap of optical communications, Journal of Optics **18**, 063002 (2016).

[4] T. B. H. Tentrup, T. Hummel, T. A. W. Wolterink, R. Uppu, A. P. Mosk, and P. W. H. Pinkse, Transmitting more than 10 bit with a single photon, Optics Express **25**, 2826–2833 (2017).

[5] C. M. Natarajan, M. G. Tanner, and R. H. Hadfield, Superconducting nanowire single-photon detectors: physics and applications, Superconductor Science and Technology **25**, 063001 (2012).

[6] L. You, Superconducting nanowire single-photon detectors for quantum information, Nanophotonics **9**, 2673–2692 (2020).

[7] L. K. Shalm, E. Meyer-Scott, B. G. Christensen, P. Bierhorst, M. A. Wayne, M. J. Stevens, T. Gerrits, S. Glancy, D. R. Hamel, M. S. Allman, K. J. Coakley, S. D. Dyer, C. Hodge, A. E. Lita, V. B. Verma, C. Lambrocco, E. Tortorici, A. L. Migdall, Y. Zhang, D. R. Kumor, W. H. Farr, F. Marsili, M. D. Shaw, J. A. Stern, C. Abellán, W. Amaya, V. Pruneri, T. Jennewein, M. W. Mitchell, P. G. Kwiat, J. C. Bienfang, R. P. Mirin, E. Knill, and S. W. Nam, Strong loophole-free test of local realism, Physical Review Letters **115**, 250402 (2015).

[8] C. Gerry and P. Knight, *Introductory quantum optics*, Vol. 1 (Cambridge University Press, 2004).

[9] J. S. Lundeen, A. Feito, H. Coldenstrodt-Ronge, K. L. Pregnell, C. Silberhorn, T. C. Ralph, J. Eisert, M. B. Plenio, and I. A. Walmsley, Tomography of quantum detectors, Nature Physics **5**, 27–30 (2009).

[10] T. Schapeler, J. P. Höpker, and T. J. Bartley, Quantum detector tomography of a 2×2 multi-pixel array of superconducting nanowire single photon detectors, Optics Express **28**, 33035–33043 (2019).

[11] S. Scheel, K. Nemoto, W. J. Munro, and P. L. Knight, Measurement-induced nonlinearity in linear optics, Physical Review A **68**, 032310 (2003).

[12] A. Migdall, S. Polyakov, J. Fan, and J. Bienfang, *Single-photon generation and detection*, Vol. 45 (Academic Press, 2013).

[13] A. Christ and C. Silberhorn, Limits on the deterministic creation of pure single-photon states using parametric down-conversion, Physical Review A **85**, 023829 (2012).

[14] O. S. Magana-Loaiza, R. de J. Leon-Montiel, A. Perez-Leija, A. B. U'Ren, C. You, K. Busch, A. E. Lita, S. W. Nam, R. P. Mirin, and T. Gerrits, Multiphoton quantum-state engineering using conditional measurements, npj Quantum Information **5**, 80 (2019).

[15] T. Gerrits, S. Glancy, T. S. Clement, B. Calkins, A. E. Lita, A. J. Miller, A. L. Migdall, S. W. Nam, R. P. Mirin, and E. Knill, Generation of optical coherent-state superpositions by number-resolved photon subtraction from the squeezed vacuum, Physical Review A **82**, 031802 (2010).

[16] A. Zavatta, V. Parigi, M. S. Kim, and M. Bellini, Subtracting photons from arbitrary light fields: experimental test of coherent state invariance by single-photon annihilation, New Journal of Physics **10**, 123006 (2008).

[17] Y. Zhai, F. E. Becerra, B. L. Glebov, J. Wen, A. E. Lita, B. Calkins, T. Gerrits, J. Fan, S. W. Nam, and A. Migdall, Photon-number-resolved detection of photon-subtracted thermal light, Optics Letters **38**, 2171–2173 (2013).

[18] A. Ourjoumtsev, R. Tualle-Brouri, J. Laurat, and P. Grangier, Generating optical Schroedinger kittens for quantum information processing, Science **312**, 83–86 (2006).

[19] A. Ourjoumtsev, H. Jeong, R. Tualle-Brouri, and P. Grangier, Generating of optical Schroedinger cats from photon number states, Nature **448**, 784–786 (2007).

[20] K. Wakui, H. Takahashi, A. Furusawa, and M. Sasaki, Photon subtracted squeezed states generated with periodically poled KTiOPO4, Optics Express **15**, 3568–3574 (2007).

[21] T. J. Bartley, G. Donati, J. B. Spring, X.-M. Jin, M. Barbieri, A. Datta, B. J. Smith, and I. A. Walmsley, Multiphoton state engineering by heralded interference between single photons and coherent states, Physical Review A **86**, 043820 (2012).

[22] A. I. Lvovsky and J. Mlynek, Quantum-optical catalysis: generating nonclassical states of light by means of linear optics, Physical Review Letters **88**, 250401 (2002).

[23] E. Meyer-Scott, J. Tiedau, G. Harder, L. K. Shalm, and T. J. Bartley, Discorrelated quantum states, Scientific Reports **7**, 41622 (2017).

[24] M. Riabinin, P. R. Sharapova, T. J. Bartley, and T. Meier, Generating two-mode squeezing with multimode measurement-induced nonlinearity, Journal of Physics Communications **5**, 045002 (2021).

[25] J. Wang, F. Sciarrino, A. Laing, and M. G. Thompson, Integrated photonic quantum technologies, Nature Photonics **14**, 273–284 (2020).

[26] S. Tanzilli, H. D. Riedmatten, W. Tittel, H. Zbinden, P. Baldi, M. D. Micheli, D. B. Ostrowsky, and N. Gisin, Highly efficient photon-pair source using periodically poled lithium niobate waveguide, Electronics Letters **37**, 26–28 (2001).

[27] M. Massaro, *Probably one photon* (PhD Thesis, Paderborn University, 2020).

[28] V. Ansari, J. M. Donohue, B. Brecht, and C. Silberhorn, Tailoring nonlinear processes for quantum optics with pulsed temporal-mode encodings, Optica **5**, 534–550 (2018).

[29] A. Eckstein, A. Christ, P. J. Mosley, and C. Silberhorn, Realistic g(2) measurement of a PDC source with single photon detectors in the presence of background, Physica Status Solidi C **8**, 1216–1219 (2011).

[30] A. M. Branczyk, Hong-ou-mandel interference, Arxiv (quant-ph), 1711.00080v1 (2017).

[31] P. J. Mosley, J. S. Lundeen, B. J. Smith, P. Wasylczyk, A. B. U'Ren, C. Silberhorn, and I. A. Walmsley, Heralded generation of ultrafast single photons in pure quantum states, Physical Review Letters **100**, 133601 (2008).

[32] C. K. Hong, Z. Y. Ou, and L. Mandel, Measurement of subpicosecond time intervals between two photons by interference, Physical Review Letters **59**, 2044 (1987).

[33] J. R. Johansson, P. D. Nation, and F. Nori, QuTiP 2: a python framework for the dynamics of open quantum systems, Computer Physics Communications **184**, 1234 (2013).

[34] P. Nation and J. Johansson, *14.01.2022*, `www.qutip.org`.

[35] T. J. Bartley, *Experimental entanglement distillation of continuous-variable optical states* (DPhil Thesis, University of Oxford, 2013).

[36] U. Leonhardt, *Measuring the quantum state of light*, Vol. 1 (Cambridge University Press, 1997).

[37] A. Freise, *Gwoptics.org*, `http://www.gwoptics.org/ComponentLibrary/`.

[38] A. I. Lvovsky and M. G. Raymer, Continous-variable optical quantum-state tomography, Review of Modern Physics **81**, 299 (2009).

[39] G. S. Thekkadath, B. A. Bell, R. B. Patel, M. S. Kim, and I. A. Walmsley, Measuring the joint spectral mode of photon pairs using intensity interferometry, Arxiv (quant-ph), 2107.06244 (2021).

[40] E. Meyer-Scott, N. Montaut, J. Tiedau, L. Sansoni, H. Herrmann, and T. J. Bartley, Limits on the heralding efficiencies and spectral purities of spectrally filtered single photons from photon-pair sources, Physical Review A **95**, 061803(R) (2017).

[41] R. J. Glauber, The quantum theory of optical coherence, Physical Review **130**, 2529 (1963).

[42] N. A. Lange, J. P. Höpker, R. Ricken, V. Quiring, C. Eigner, C. Silberhon, and T. J. Bartley, Supplementary document for cryogenic integrated spontaneous parametric down-conversion, Optica **9** (2022).

[43] A. Christ, K. Laiho, A. Eckstein, K. N. Cassemiro, and C. Silberhorn, Probing multimode squeezing with correlation functions, New Journal of Physics **13**, 033027 (2011).

[44] N. Montaut, *Integrated single photon sources: development to benchmarking* (PhD Thesis, Paderborn University, 2019).

[45] F. Thiele, F. vom Bruch, V. Quiring, R. Ricken, H. Herrmann, C. Eigner, C. Silberhorn, and T. J. Bartley, Cryogenic electro-optic polarisation conversion in titanium indiffused lithium niobate waveguides, Optics Express **28**, 28961–28968 (2010).

[46] M. Bartnick, M. Santandrea, J. P. Höpker, F. Thiele, R. Ricken, V. Quiring, C. Eigner, H. Herrmann, C. Silberhorn, and T. J. Bartley, Cryogenic second-harmonic generation in periodically poled lithium niobate waveguides, Physical Review Applied **15**, 024028 (2021).

[47] N. A. Lange, J. P. Höpker, R. Ricken, V. Quiring, C. Eigner, C. Silberhon, and T. J. Bartley, Cryogenic integrated spontaneous parametric down-conversion, Optica **9**, 108–111 (2022).

[48] F. Thiele, F. vom Bruch, J. Brockmeier, M. Protte, T. Hummel, R. Ricken, V. Quiring, S. Lengeling, H. Herrmann, C. Eigner, C. Silberhorn, and T. J. Bartley, Cryogenic

electro-optic modulation in titanium in-diffused lithium niobate waveguides, Arxiv (quant-ph), 2202.00306 (2022).

[49] P. R. Sharapova, K. H. Luo, H. Herrmann, M. Reichelt, T. Meier, and C. Silberhorn, Toolbox for the design of LiNbO3-based passive and active integrated quantum circuits, New Journal of Physics **19**, 123009 (2017).

[50] J. P. Höpker, V. B. Verma, M. Protte, R. Ricken, V. Quirinq, C. Eigner, L. Ebers, M. Hammer, J. Förstner, C. Silberhorn, R. P. Mirin, S. W. Nam, and T. J. Bartley, Integrated superconducting nanowire single-photon detectors on titanium in-diffused lithium niobate waveguides, Journal of Physics: Photonics **3**, 034022 (2021).

[51] R. Regener and W. Sohler, Loss in low-finesse Ti:LiNbO3 optical waveguide resonators, Applied Physics B **36**, 143–147 (1985).

[52] W. Demtröder, *Experimentalphysik 2*, Vol. 5 (Springer-Lehrbuch, 2009).

[53] Thorlabs Inc., *08.09.2021*, `www.thorlabs.com/thorproduct.cfm?partnumber=TN1550R5F2`.

[54] N. Montaut, L. Sansoni, E. Meyer-Scott, R. Ricken, V. Quiring, H. Herrmann, and C. Silberhorn, High-efficiency plug-and-play source of heralded single photons, Physical Review Applied **8**, 024021 (2017).

[55] G. D. Giuseppe, M. Atatüre, M. D. Shaw, A. V. Sergienko, B. E. A. Saleh, M. C. Teich, A. J. Miller, S. W. Nam, and J. Martinis, Direct observation of photon pairs at a single output port of a beam-splitter interferometer, Physical Review A **68**, 063817 (2003).

[56] T. Schapeler, *Quantum detector tomography of superconducting detector arrays* (MSc Thesis, Paderborn University, 2020).

[57] R. Hadfield and G. Johansson, *Superconducting devices in quantum optics*, Vol. 1 (Springer, Cham, 2016).

[58] O. Thomas, Z. L. Yuan, J. F. Dynes, A. W. Sharpe, and A. J. Shields, Efficient photon number detection with silicon avalanche photodiodes, Applied Physics Letters **97**, 031102 (2010).

[59] D. S. Bethune, W. P. Risk, and G. W. Pabst, A high-performance integrated single-photon detector for telecom wavelengths, Journal of Modern Optics **51**, 1359–1368 (2004).

[60] A. P. VanDevender and P. G. Kwiat, Quantum transduction via frequency upconversion (invited), Journal of the Optical Society of America B **24**, 295–299 (2007).

[61] A. M. Kadin, M. Leung, A. D. Smith, and J. M. Murduck, Nonbolometric infrared detection in thin superconducting films via photoproduction of fluxon pairs, IEEE Transactions on Magnetics **27**, 1540–1543 (1991).

[62] A. M. Kadin and M. W. Johnson, Nonequilibrium photon-induced hotspot: a new mechanism for photodetection in ultrathin metallic films, Applied Physics Letters **69**, 3938 (1996).

[63] M. A. C. Perryman, C. L. Foden, and A. Peacock, A new approach to optical photon detection, ESA Symposium on Photon Detectors for Space Instrumentation **SEE N94-15025 03-19**, 21–26 (1992).

[64] K. D. Irwin, G. C. Hilton, D. A. Wollman, and J. M. Martinis, X-ray detection using a superconducting transition-edge sensor microcalorimeter with electrothermal feedback, Applied Physics Letters **69**, 1945–1947 (1996).

[65] A. Peacock, P. Verhoeve, N. Rando, A. van Dordrecht, B. G. Taylor, C. Erd, M. A. C. Perryman, R. Venn, J. Howlett, D. J. Goldie, J. Lumley, and M. Wallis, Single optical photon detection with a superconducting tunnel junction, Nature **381**, 135–137 (1996).

[66] G. N. Gol'tsman, O. Okunev, G. Chulkova, A. Lipatov, A. Semenov, K. Smirnov, B. Voronov, A. Dzardanov, C. Williams, and R. Sobolewski, Picosecond superconducting single-photon optical detector, Applied Physics Letters **79**, 705 (2001).

[67] F. Marsili, V. B. Verma, J. A. Stern, S. Harrington, A. E. Lita, T. Gerrits, I. Vayshenker, B. Baek, M. D. Shaw, R. P. Mirin, and S. W. Nam, Detecting single infrared photons with 93% system efficiency, Nature Photonics **7**, 210–214 (2013).

[68] D. V. Reddy, R. R. Nerem, A. E. Lita, S. W. Nam, R. P. Mirin, and V. B. Verma, Superconducting nanowire single-photon detectors with 98% system detection efficiency at 1550 nm, Optica **7**, 1649–1653 (2021).

[69] Y. Hochberg, I. Charaev, S.-W. Nam, V. Verma, M. Colangelo, and K. K. Berggren, Detecting sub-GeV dark matter with superconducting nanowires, Physical Review Letters **123**, 151802 (2019).

[70] B. Korzh, Q.-Y. Zhao, J. P. Allmaras, S. Frasca, T. M. Autry, E. A. Bersin, A. D. Beyer, R. M. Briggs, B. Bumble, M. Colangelo, G. M. Crouch, A. E. Dane, T. Gerrits, A. E. Lita, F. Marsili, G. Moody, C. Peña, E. Ramirez, J. D. Rezac, N. Sinclair, M. J. Stevens, A. E. Velasco, V. B. Verma, E. E. Wollman, S. Xie, D. Zhu, P. D. Hale, M. Spiropulu, K. L. Silverman, R. P. Mirin, S. W. Nam, A. G. Kozorezov, M. D. Shaw, and K. K. Berggren, Demonstration of sub-3 ps temporal resolution with a superconducting nanowire single-photon detector, Nature Photonics **14**, 250–255 (2020).

[71] A. E. Lita, A. J. Miller, and S. W. Nam, Counting near-infrared single-photons with 95% efficiency, Optics Express **16**, 3032–3040 (2008).

[72] I. Holzman and Y. Ivry, Superconducting nanowires for single-photon detection: progress, challenges, and opportunities, Advanced Quantum Technologies **2**, 1800058 (2019).

[73] I. E. Zadeh, J. Chang, J. W. N. Los, S. Gyger, A. W. Elshaari, S. Steinhauer, S. N. Dorenbos, and V. Zwiller, Superconducting nanowire single-photon detectors: a perspective on evolution, state-of-the-art, future developments, and applications, Applied Physics Letters **118**, 190502 (2021).

[74] J. Münzberg, A. Vetter, F. Beutel, W. Hartmann, S. Ferrari, W. H. P. Pernice, and C. Rockstuhl, Superconducting nanowire single-photon detector implemented in a 2D photonic crystal cavity, Optica **5**, 658–665 (2018).

[75] C. Cahall, K. L. Nicolich, N. T. Islam, G. P. Lafyatis, A. J. Miller, D. J. Gauthier, and J. Kim, Multi-photon detection using a conventional superconducting nanowire single-photon detector, Optica **4**, 1534–1535 (2017).

[76] D. Zhu, M. Colangelo, C. Chen, B. A. Korzh, F. N. C. Wong, M. D. Shaw, and K. K. Berggren, Resolving photon numbers using a superconducting nanowire with impedance-matching taper, Nano Letters **20**, 3858–3863 (2020).

[77] Y. P. Korneeva, N. N. Manova, I. N. Florya, M. Y. Mikhailov, O. Dobrovolskiy, A. A. Korneev, and D. Y. Vodolazov, Different single-photon response of wide and narrow superconducting Mo(x)Si(1-x) strips, Physical Review Applied **13**, 024011 (2020).

[78] J. J. Renema, R. Gaudio, Q. Wang, Z. Zhou, A. Gaggero, F. Mattioli, R. Leoni, D. Sahin, M. J. A. de Dood, A. Fiore, and M. P. van Exter, Experimental test of theories of the detection mechanism in a nanowire superconducting single photon detector, Physical Review Letters **112**, 117604 (2014).

[79] S. Jahani, L.-P. Yang, A. B. Tepole, J. C. Bardin, H. X. Tang, and Z. Jacob, Probabilisitc vortex crossing criterion for superconducting nanowire single-photon detectors, Journal of Applied Physics **127**, 143101 (2020).

[80] B. Cabrera, R. M. Clarke, P. Colling, A. J. Miller, S. Nam, and R. W. Romani, Detection of single infrared, optical, and ultraviolet photons using superconducting transition edge sensors, Applied Physics Letters **73**, 735 (1998).

[81] W. Pernice, C. Schuck, O. Minaeva, M. Li, G. Goltsman, A. Sergienko, and H. Tang, High-speed and high-efficiency travelling wave single-photon detectors embedded in nanophotonic circuits, Nature Communications **3**, 1325 (2012).

[82] M. K. Akhlaghi, E. Schelew, and J. F. Young, Waveguide integrated superconducting single-photon detectors implemented as near-perfect absorbers of coherent radiation, Nature Communications **6**, 8233 (2015).

[83] S. Buckley, J. Chiles, A. N. McCaughan, G. Moody, K. L. Silverman, M. J. Stevens, R. P. Mirin, S. W. Nam, and J. M. Shainline, All-silicon light-emitting diodes waveguide-integrated with superconducting single-photon detectors, Applied Physics Letters **111**, 141101 (2017).

[84] J. Li, R. A. Kirkwood, L. J. Baker, D. Bosworth, K. Erotokritou, A. Banerjee, R. M. Heath, C. M. Natarajan, Z. H. Barber, M. Sorel, and R. H. Hadfield, Nano-optical single-photon response mapping of waveguide integrated molybdenum silicide (MoSi) superconducting nanowires, Optics Express **24**, 250–255 (2016).

[85] O. Kahl, S. Ferrari, V. Kovalyuk, A. Vetter, G. Lewes-Malandrakis, C. Nebel, A. Korneev, G. Goltsman, and W. Pernice, Spectrally multiplexed single-photon detection with hybrid superconducting nanophotonic circuits, Optica **4**, 557–562 (2017).

[86] C. Schuck, W. H. P. Pernice, and H. X. Tang, Waveguide integrated low noise NbTiN nanowire single-photon detectors with milli-Hz dark count rate, Scientific Reports **3**, 1893 (2013).

[87] J. M. Shainline, S. M. Buckley, N. Nader, C. M. Gentry, K. C. Cossel, J. W. Cleary, M. Popović, N. R. Newbury, S. W. Nam, and R. P. Mirin, Room-temperature-deposited dielectrics and superconductors for integrated photonics, Optics Express **25**, 10322–10334 (2017).

[88] D. Smith, D. S. Phillips, P. L. Mennea, V. B. Verma, A. E. Lita, T. Gerrits, R. P. Mirin, R. H. Bannerman, P. C. Gow, J. J. Renema, R. J. Francis-Jones, R. B. Patel, S. Sempere-Llagostera, P. G. Smith, S. W. Nam, I. A. Walmsley, and J. C. Gates, Multiplexed superconducting nanowire single-photon detectors on UV-written silica waveguides, Single Photon Workshop (2019).

[89] T. Gerrits, N. Thomas-Peter, J. C. Gates, A. E. Lita, B. J. Metcalf, B. Calkins, N. A. Tomlin, A. E. Fox, A. L. Linares, J. B. Spring, N. K. Langford, R. Mirin, P. G. Smith, I. A. Walmsley, and S. W. Nam, On-chip, photon-number-resolving, telecom-band detectors for scalable photonic information processing, Conference on Lasers and Electro-Optics 2012 (2012).

[90] J. P. Sprengers, A. Gaggero, D. Sahin, S. Jahanmirinejad, G. Frucci, F. Mattioli, R. Leoni, J. Beetz, M. Lermer, M. Kamp, S. Höfling, R. Sanjines, and A. Fiore, Waveguide superconducting single-photon detectors for integrated quantum photonic circuits, Applied Physics Letters **99**, 181110 (2011).

[91] F. Najafi, J. Mower, N. C. Harris, F. Bellei, A. Dane, C. Lee, X. Hu, P. Kharel, F. Marsili, S. Assefa, K. K. Berggren, and D. Englund, On-chip detection of non-classical light by scalable integration of single-photon detectors, Nature Communications **6**, 5873 (2015).

[92] P. Rath, O. Kahl, S. Ferrari, F. Sproll, G. Lewes-Malandrakis, D. Brink, K. Ilin, M. Siegel, C. Nebel, and W. Pernice, Superconducting single-photon detectors integrated with diamond nanophotonic circuits, Light: Science & Applications **4**, e338 (2015).

[93] H. A. Atikian, S. Meesala, M. J. Burek, Y.-I. Sohn, J. Israelian, A. S. Patri, N. Clarke, A. Sipahigil, R. E. Evans, D. D. Sukachev, R. Westervelt, M. D. Lukin, and M. Loncar, *Novel fabrication of diamond nanophotonics coupled to single-photon detectors*, www.doi.org/10.1117/2.1201611.006765, 2017.

[94] A. A. Sayem, R. Cheng, S. Wang, and H. X. Tang, Lithium-niobate-on-insulator waveguide-integrated superconducting nanowire single-photon detectors, Applied Physics Letters **116**, 151102 (2020).

[95] M. G. Tanner, L. S. E. Alvarez, W. Jiang, R. J. Warburton, Z. H. Barber, and R. H. Hadfield, A superconducting nanowire single photon detector on lithium niobate, Nanotechnology **23**, 505201 (2012).

[96] J. P. Höpker, M. Bartnick, E. Meyer-Scott, F. Thiele, T. Meier, T. Bartley, S. Krapick, N. M. Montaut, M. Santandrea, H. Herrmann, S. Lengeling, R. Ricken, V. Quiring, A. E. Lita, V. B. Verma, T. Gerrits, S. W. Nam, and C. Silberhorn, Towards integrated superconducting detectors on lithium niobate waveguides, SPIE Quantum Photonic Devices (2017).

[97] J. P. Höpker, T. Gerrits, A. Lita, S. Krapick, H. Herrmann, R. Ricken, V. Quiring, R. Mirin, S. W. Nam, C. Silberhorn, and T. J. Bartley, Integrated transition edge sensors on titanium in-diffused lithium niobate waveguides, APL Photonics **4**, 056103 (2019).

[98] G. J. Edwards and M. Lawrence, A temperature-dependent dispersion equation for congruently grown lithium niobate, Optical and Quantum Electronics **16**, 373–375 (1984).

[99] D. H. Jundt, Temperature-dependent sellmeier equation for the index of refraction, ne, in congruent lithium niobate, Optics Letters **22**, 1553–1555 (1997).

[100] E. Strake, G. Bava, and I. Montrosset, Guided modes of Ti:LiNbO3 channel waveguides: a novel quasi-analytical technique in comparison with the scalar finite-element method, Journal of Lightwave Technology **6**, 1126–1135 (1988).

[101] S. Korotky, W. Minford, L. Buhl, M. Divino, and R. Alferness, Mode size and method for estimating the propagation constant of single-mode Ti:LiNbO3 strip waveguides, IEEE Journal of Quantum Electronics **18**, 1796–1801 (1982).

[102] Synopsys Inc., *Rsoft FemSIM v2016.03 user guide* (2016).

[103] T. Gerrits, A. Migdall, J. C. Bienfang, J. Lehman, S. W. Nam, J. Splett, I. Vayshenker, and J. Wang, Calibration of free-space and fiber-coupled single-photon detectors, Metrologia **57**, 015002 (2020).

[104] S. B. Lang, Pyroelectricity: from ancient curiosity to modern imaging tool, Physics Today **58**, 31 (2005).

[105] S. Jachalke, E. Mehner, H. Stöcker, J. Hanzig, M. Sonntag, T. Weigel, T. Leisegang, and D. C. Meyer, How to measure the pyroelectric coefficient, Applied Physics Reviews **4**, 021303 (2017).

[106] A. N. Oleinik, P. V. Karataev, A. A. Klenin, A. S. Kubankin, K. V. Fedorov, and A. V. Shchagin, Lateral surface electrization of z-cut lithium niobate during pyroelectric effect, Russian Physics Journal **63**, 119–125 (2020).

[107] B. Calkins, P. L. Mennea, A. E. Lita, B. J. Metcalf, W. S. Kolthammer, A. Lamas-Linares, J. B. Spring, P. C. Humphreys, R. P. Mirin, J. C. Gates, P. G. R. Smith, I. A. Walmsley, T. Gerrits, and S. W. Nam, High quantum-efficiency photon-number-resolving detector for photonic on-chip information processing, Optics Express **21**, 22657–22670 (2013).

[108] T. Gerrits, N. Thomas-Peter, J. C. Gates, A. E. Lita, B. J. Metcalf, B. Calkins, N. A. Tomlin, A. E. Fox, A. L. Linares, J. B. Spring, N. K. Langford, R. P. Mirin, P. G. R. Smith, I. A. Walmsley, and S. W. Nam, On-chip, photon-number-resolving, telecommunication-band detectors for scalable photonic information processing, Physical Review A **84**, 060301 (2011).

[109] D. J. Fixsen, S. H. Moseley, T. Gerrits, A. E. Lita, and S. W. Nam, Optimal energy measurement in nonlinear systems: an application of differential geometry, Journal of Low Temperature Physics **176**, 16–26 (2014).

[110] J. P. Höpker, *Integrated cryogenic manipulation and detection of photonic quantum states* (MSc Thesis, Paderborn University, 2017).

[111] J. Chiles, S. M. Buckley, A. E. Lita, V. B. Verma, J. Allmaras, B. Korzh, M. D. Shaw, J. M. Shainline, R. P. Mirin, and S. W. Nam, Superconducting microwire detectors based on WSi with single-photon sensitivity in the near-infrared, Applied Physics Letters **116**, 242602 (2020).

[112] M. Protte, V. B. Verma, J. P. Höpker, R. P. Mirin, S. W. Nam, and T. J. Bartley, Laser-lithographically written micron-wide superconducting nanowire single-photon detectors, Arxiv (physics.ins-det), 2112.07976 (2022).

[113] K. Hattori, S. Inoue, R. Kobayashi, K. Niwa, T. Numata, and D. Fukuda, Optical transition-edge sensors: dependence of system detection efficiency on wavelength, IEEE Transactions on Instrumentation and Measurement **68**, 2253–2259 (2019).

[114] Z. Yang, T. Albrow-Owen, W. Cai, and T. Hasan, Miniaturization of optical spectrometers, Science **371**, eabe0722 (2021).

[115] K. Niwa, T. Numata, K. Hattori, and D. Fukuda, Few-photon color imaging using energy-dispersive superconducting transition-edge sensor spectrometry, Scientific Reports **7**, 45660 (2017).

[116] P. C. Nagler, M. A. Greenhouse, S. H. Moseley, B. J. Rauscher, and J. E. Sadleir, Development of transition edge sensor detectors optimized for single-photon spectroscopy in the optical and near-infrared, SPIE High Energy, Optical, and Infrared Detectors for Astronomy VIII (2018).

Appendix

A

A.1 Wave equation and the harmonic oscillator

In Section 2.1, the analogy between the electromagnetic field and harmonic oscillator is introduced. In this section, this analogy is elaborated further. Starting with Maxwell's equations in vacuum and setting c=$\frac{1}{\sqrt{\mu_0 \varepsilon_0}}$, where μ_0 is the vacuum permeability, ε_0 the vacuum permittivity, E the electric field, B the magnetic field, and $\frac{\partial}{\partial t}$ the partial time derivation, the equations can be written as (Reference [52] (pp. 140-195))

$$\nabla \cdot E = 0, \tag{A.1}$$

$$\nabla \cdot B = 0, \tag{A.2}$$

$$\nabla \times E = -\frac{1}{c}\frac{\partial B}{\partial t}, \tag{A.3}$$

$$\nabla \times B = \frac{1}{c}\frac{\partial E}{\partial t}. \tag{A.4}$$

In the Coloumb gauge $\nabla \cdot A = 0$ for $B = \nabla \times A$, it follows that (Reference [8] (p. 18))

$$0 = \nabla^2 A - \frac{1}{c^2}\frac{\partial^2 A}{\partial t^2}, \tag{A.5}$$

which is the wave equation for the vector potential A with speed c.

A solution to this wave equation is the plane wave (Reference [8] (p. 20))

$$A_k = \epsilon_{k,s} A_{k,s} \mathrm{e}^{i(kr-\omega_k t)}, \tag{A.6}$$

where $\epsilon_{k,s}$ represents the real polarization vector and $A_{k,s}$ is the complex wave amplitude for the two polarizations s. k is the wavenumber, ω_k the angular frequency, and r the spatial variable. In addition, it holds that $\omega_k = \mathrm{c}|k|$.

For an unconfined system (infinite space), k is unrestricted, but for a confined system with volume $V = L^3$ which can be expanded to $L \to \infty$ (with periodic boundary conditions), it holds that

$$k = \frac{2\pi}{L} m \text{ with } m = 0, 1, 2, 3, \ldots \tag{A.7}$$

Therefore, the solution with these boundary conditions can be written as

$$A(r,t) = \sum_{k,s} \epsilon_{k,s} \left(A_{k,s} \mathrm{e}^{i(kr-\omega_k t)} + A^*_{k,s} \mathrm{e}^{-i(kr-\omega_k t)} \right). \tag{A.8}$$

Combining this with $E = -\frac{\partial A}{\partial t}$, it follows that

$$E(r,t) = \sum_{k,s} \epsilon_{k,s} i\omega_k \left(A_{k,s} \mathrm{e}^{i(kr-\omega_k t)} + A^*_{k,s} \mathrm{e}^{-i(kr-\omega_k t)} \right). \tag{A.9}$$

The total energy of this radiation field is given by (Reference [8] (p. 21))

$$\begin{aligned} H &= \frac{1}{2} \int_V dV \left(\varepsilon_0 E^2 + \frac{1}{\mu_0} B^2 \right) && \text{(A.10)} \\ &= \sum_{k,s} \varepsilon_0 V \omega_k^2 \left(A_{k,s} A^*_{k,s} + A^*_{k,s} A_{k,s} \right). && \text{(A.11)} \end{aligned}$$

This equation has the same form as the harmonic oscillator

$$H = \frac{1}{2} \hbar\omega (\hat{a}\hat{a}^\dagger + \hat{a}^\dagger \hat{a}). \tag{A.12}$$

Therefore, restricting Equation (A.11) to only one mode, $A_{k,s}$ and $A^*_{k,s}$ can be written (in analogy to Equation (2.2) and (2.3)) as

$$A_{k,s} = \frac{\gamma}{\sqrt{2\hbar\omega}} (\omega q + ip), \tag{A.13}$$

$$A^*_{k,s} = \frac{\gamma}{\sqrt{2\hbar\omega}} (\omega q - ip). \tag{A.14}$$

Here, γ is a constant prefactor. Rearranging these equations, shows the analogy between the form of the generalized position and its conjugate momentum variables q and p for the harmonic oscillator and the real and imaginary part of the amplitude of an electromagnetic field, as

$$q = \frac{\sqrt{2\hbar\omega}}{\gamma\omega} \frac{A_{k,s} + A^*_{k,s}}{2} = \frac{\sqrt{2\hbar\omega}}{\gamma\omega} \mathrm{Re}(A_{k,s}) \tag{A.15}$$

$$p = \frac{\sqrt{2\hbar\omega}}{\gamma} \frac{A_{k,s} - A^*_{k,s}}{2i} = \frac{\sqrt{2\hbar\omega}}{\gamma} \mathrm{Im}(A_{k,s}) \tag{A.16}$$

A.2 Analytical investigation of single-photon interference

In Section 2.3, it is shown graphically that the photon-number statistics resulting from the interference of different Fock states cannot be treated as a combination of a partial interference with a subsequent photon addition. In this section, this statement is investigated analytically. As explained in Reference [8] (p. 139), the output modes of a 50:50 beam splitter are related to the input modes as

$$\hat{c} = \frac{1}{\sqrt{2}}(\hat{a} + i\hat{b}), \tag{A.17}$$

$$\hat{d} = \frac{1}{\sqrt{2}}(i\hat{a} + \hat{b}). \tag{A.18}$$

Therefore, the creation operators can be rewritten as

$$\hat{a} = \frac{1}{\sqrt{2}}(\hat{c} + i\hat{d}), \tag{A.19}$$

$$\hat{b} = \frac{1}{\sqrt{2}}(i\hat{c} + \hat{d}). \tag{A.20}$$

Next, the output states for different inputs ($|1,0\rangle$, $|2,0\rangle$, $|3,0\rangle$, $|1,1\rangle$, and $|2,1\rangle$) are calculated.

$$|1,0\rangle = \hat{a}^\dagger |0,0\rangle \xrightarrow{BS} \frac{\hat{c}^\dagger + i\hat{d}^\dagger}{\sqrt{2}} |0,0\rangle \tag{A.21}$$

$$= \frac{1}{\sqrt{2}}(|1,0\rangle + i\,|0,1\rangle) \tag{A.22}$$

$$|2,0\rangle = \frac{1}{\sqrt{2}}(\hat{a}^\dagger)^2 |0,0\rangle \xrightarrow{BS} \frac{1}{\sqrt{2}}\left(\frac{\hat{c}^\dagger + i\hat{d}^\dagger}{\sqrt{2}}\right)^2 |0,0\rangle \tag{A.23}$$

$$= \frac{1}{2}(|2,0\rangle + \sqrt{2}i\,|1,1\rangle - |0,2\rangle) \tag{A.24}$$

$$|3,0\rangle = \frac{1}{\sqrt{6}}(\hat{a}^\dagger)^3 |0,0\rangle \xrightarrow{BS} \frac{1}{\sqrt{6}}\left(\frac{\hat{c}^\dagger + i\hat{d}^\dagger}{\sqrt{2}}\right)^3 |0,0\rangle \tag{A.25}$$

$$= \frac{1}{\sqrt{8}}(|3,0\rangle + \sqrt{3}i\,|2,1\rangle - \sqrt{3}\,|1,2\rangle - i\,|0,3\rangle) \tag{A.26}$$

$$|1,1\rangle = \hat{a}^\dagger \hat{b}^\dagger |0,0\rangle \xrightarrow{BS} \frac{\hat{c}^\dagger + i\hat{d}^\dagger}{\sqrt{2}} \frac{i\hat{c}^\dagger + \hat{d}^\dagger}{\sqrt{2}} |0,0\rangle \tag{A.27}$$

$$= \frac{i}{\sqrt{2}}(|2,0\rangle + |0,2\rangle) \tag{A.28}$$

$$|2,1\rangle = \frac{1}{\sqrt{2}}(\hat{a}^\dagger)^2 \hat{b}^\dagger |0,0\rangle \xrightarrow{BS} \frac{1}{\sqrt{2}} \left(\frac{\hat{c}^\dagger + i\hat{d}^\dagger}{\sqrt{2}}\right)^2 \left(\frac{i\hat{c}^\dagger + \hat{d}^\dagger}{\sqrt{2}}\right) |0,0\rangle \tag{A.29}$$

$$= \frac{1}{\sqrt{8}}(\sqrt{3}i\,|3,0\rangle - |2,1\rangle + i\,|1,2\rangle - \sqrt{3}\,|0,3\rangle) \tag{A.30}$$

When comparing the results for $|3,0\rangle$ and $|2,1\rangle$, it can be seen that they are not identical even though they contain the same total photon number. While all output states are symmetrical due to the 50:50 beam splitter, any photon addition in one of the outputs breaks this symmetry. Therefore, a subsequent photon addition in combination with the interference of fewer photons cannot be used to replicate multi-photon interference.

Assuming that two states are send through the beam splitter with a small time difference (therefore two separate temporal modes) that cannot be resolved with otherwise perfect photon-number resolving detectors, the probabilities for different measurement outcomes can be compared.

Starting with the input $|1,0\rangle\,|1,0\rangle$ which corresponds to two single photons entering the beam splitter one after another, it transforms as

$$|1,0\rangle\,|1,0\rangle \xrightarrow{BS} \frac{1}{2}(|1,0\rangle\,|1,0\rangle + i\,|1,0\rangle\,|0,1\rangle + i\,|0,1\rangle\,|1,0\rangle - |0,1\rangle\,|0,1\rangle). \tag{A.31}$$

Therefore, the probabilities of the different outcomes are

$$p(1,0,1,0) = \frac{1}{4}, \tag{A.32}$$

$$p(1,0,0,1) = \frac{1}{4}, \tag{A.33}$$

$$p(0,1,1,0) = \frac{1}{4}, \tag{A.34}$$

$$p(0,1,0,1) = \frac{1}{4}. \tag{A.35}$$

Adding the probabilities due to the non-temporal detector resolution gives

$$p(2,0) = p(1,0,1,0) = \frac{1}{4}, \tag{A.36}$$

$$p(1,1) = p(1,0,0,1) + p(0,1,1,0) = \frac{1}{2}, \tag{A.37}$$

$$p(0,2) = p(0,1,0,1) = \frac{1}{4}, \tag{A.38}$$

which matches the result for the $|2,0\rangle$ ($|2,0\rangle\,|0,0\rangle$) input state. This method can be repeated for the input states $|2,0\rangle\,|1,0\rangle$ and $|2,0\rangle\,|0,1\rangle$ as

$$|2,0\rangle\,|1,0\rangle \xrightarrow{BS} \frac{1}{4}(\sqrt{2}\,|2,0\rangle\,|1,0\rangle + 2i\,|1,1\rangle\,|1,0\rangle - \sqrt{2}\,|0,2\rangle\,|1,0\rangle \tag{A.39}$$

$$+\sqrt{2}i\,|2,0\rangle\,|0,1\rangle - 2\,|1,1\rangle\,|0,1\rangle - \sqrt{2}i\,|0,2\rangle\,|0,1\rangle\,, \tag{A.40}$$

$$|2,0\rangle\,|0,1\rangle \xrightarrow{BS} \frac{1}{4}(\sqrt{2}i\,|2,0\rangle\,|1,0\rangle - 2\,|1,1\rangle\,|1,0\rangle - \sqrt{2}i\,|0,2\rangle\,|1,0\rangle \tag{A.41}$$

$$+\sqrt{2}\,|2,0\rangle\,|0,1\rangle + 2i\,|1,1\rangle\,|0,1\rangle - \sqrt{2}\,|0,2\rangle\,|0,1\rangle\,. \tag{A.42}$$

For both inputs, the added probabilities are

$$p(3,0) = p(2,0,1,0) = \frac{1}{8}, \tag{A.43}$$

$$p(2,1) = p(2,0,0,1) + p(1,1,1,0) = \frac{3}{8}, \tag{A.44}$$

$$p(1,2) = p(1,1,0,1) + p(0,2,1,0) = \frac{3}{8}, \tag{A.45}$$

$$p(0,3) = p(0,2,0,1) = \frac{1}{8}. \tag{A.46}$$

These probabilities match the results for the $|3,0\rangle$ ($|3,0\rangle\,|0,0\rangle$) input state.

When investigating the input $|1,1\rangle\,|1,0\rangle$ with the same total photon number, it transforms to

$$|1,1\rangle\,|1,0\rangle \xrightarrow{BS} \frac{1}{2}(i\,|2,0\rangle\,|1,0\rangle + i\,|0,2\rangle\,|1,0\rangle - |2,0\rangle\,|0,1\rangle - |0,2\rangle\,|0,1\rangle). \tag{A.47}$$

Here the probabilities

$$p(3,0) = p(2,0,1,0) = \frac{1}{4}, \tag{A.48}$$

$$p(2,1) = p(2,0,0,1) = \frac{1}{4}, \tag{A.49}$$

$$p(1,2) = p(0,2,1,0) = \frac{1}{4}, \tag{A.50}$$

$$p(0,3) = p(0,2,0,1) = \frac{1}{4} \tag{A.51}$$

do not match the $|3,0\rangle\,|0,0\rangle$ input but also not the $|2,1\rangle\,|0,0\rangle$ input. Therefore, even when including a second set of modes, multi-photon interference cannot simply be treated as a combination of subsets of interfering and non-interfering states.

A.3 Analytical investigation of a photon-subtracted coherent state

While photon subtraction acts linearly on Fock states and nonlinear on thermal states, also coherent states have a special role in this scenario. As shown in Section 2.1, a coherent state can be written as

$$|\alpha\rangle = \mathrm{e}^{-\frac{1}{2}|\alpha|^2} \sum_{n=0}^{\infty} \frac{\alpha^n}{\sqrt{n!}} |n\rangle = \mathrm{e}^{-\frac{1}{2}|\alpha|^2} \sum_{n=0}^{\infty} \frac{\alpha^n (\hat{a}^\dagger)^n}{n} |0\rangle . \tag{A.52}$$

Including the power series for the exponential function leads to

$$|\alpha\rangle = \mathrm{e}^{-\frac{|\alpha|^1}{2} + \alpha \hat{a}^\dagger} |0\rangle . \tag{A.53}$$

Using Equation (2.9), it holds that

$$\mathrm{e}^{-\alpha^* \hat{a}} |0\rangle = |0\rangle . \tag{A.54}$$

Form expanding Equation (A.53), it follows that

$$|\alpha\rangle = \mathrm{e}^{-\frac{|\alpha|^1}{2} + \alpha \hat{a}^\dagger - \alpha^* \hat{a}} |0\rangle \tag{A.55}$$

$$= \mathrm{e}^{\alpha \hat{a}^\dagger - \alpha^* \hat{a}} |0\rangle = \hat{D}(\alpha) |0\rangle . \tag{A.56}$$

In analogy to Section A.2, the outcome of a beam splitter can be investigated as

$$|0, \alpha\rangle \xrightarrow{BS} \mathrm{e}^{\frac{\alpha}{\sqrt{2}}\left(i\hat{c}^\dagger + \hat{d}^\dagger\right) - \frac{\alpha^*}{\sqrt{2}}\left(-i\hat{c}^\dagger + \hat{d}^\dagger\right)} |0, 0\rangle = \frac{1}{\sqrt{2}} |i\alpha, \alpha\rangle = |\alpha'\rangle |\beta'\rangle . \tag{A.57}$$

It can be seen that both output modes of the beam splitter are again coherent states with a reduces amplitude. When executing a measurement $\hat{\Pi}_B$ on the second output put $|\beta'\rangle$, the first output $|\alpha'\rangle$ is not influenced as

$$\mathrm{Tr}_B(\hat{1}_A \otimes \hat{\Pi}_B |\alpha'\rangle \langle\alpha'| \otimes |\beta'\rangle \langle\beta'|) = |\alpha'\rangle \langle\alpha'| \otimes \mathrm{Tr}_B(\hat{\Pi}_B |\beta'\rangle \langle\beta'|). \tag{A.58}$$

A.4 QuTiP simulations with coherent-state amplitudes higher than one

While the QuTiP simulations presented in Section 2.4 contain a coherent-state amplitude of one for clarity, features like discorrelation [23], become more visible at higher coherent-state amplitudes. Unfortunately, it was not possible to investigate bigger coherent states experimentally, due to the discrepancy between the laser repetition rate and detector dead time as well as latching. When investigating these states in computer simulations, care must be taken when setting the maximum levels in the limited Hilbert space. Too small values lead to inaccurate simulation results, while too large values require high computing power. Figure A.1 shows the simulation results for the interference of a single photon and coherent state of mean photon number $\bar{n}$=2 in *optical circuit A*. Figure A.2 shows the simulation results using a mean photon number of $\bar{n}$=4, respectively.

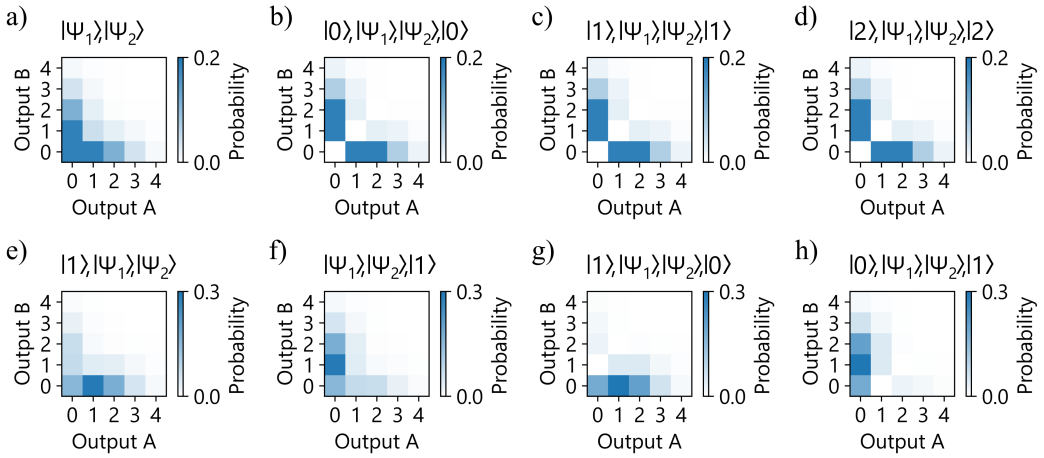

Figure A.1: Photon-number statistics for a single photon and coherent state of mean photon number $\bar{n}$=2 interfering in *optical circuit A*; a) no measurement at both detectors, b) subtraction of zero photons at both detectors, c) subtraction of one photon at both detectors, d) subtraction of two photons at both detectors, e) and f) subtraction of one photon at one detector and no measurement at the other detector, and g) and h) subtraction of one photon at one detector and zero photons at the other detector.

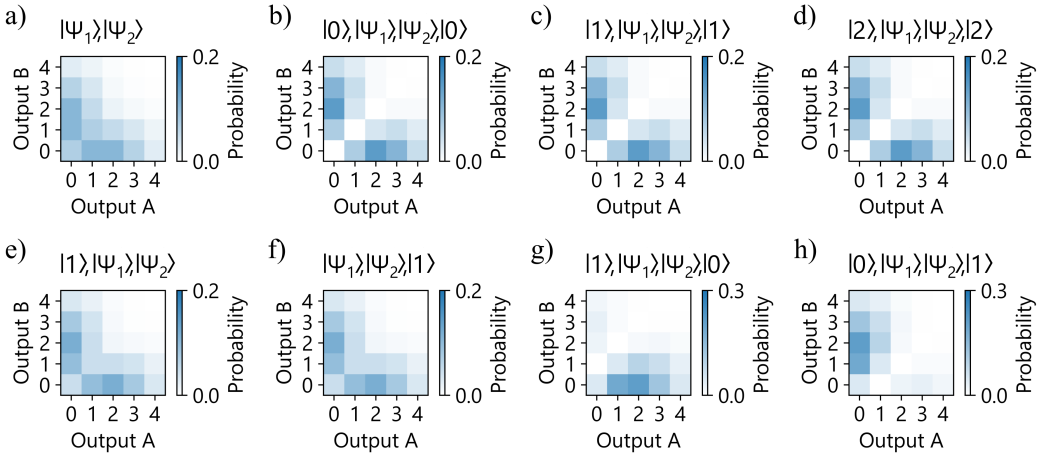

Figure A.2: Photon-number statistics for a single photon and coherent state of mean photon number $\bar{n}$=4 interfering in *optical circuit A*; a) no measurement at both detectors, b) subtraction of zero photons at both detectors, c) subtraction of one photon at both detectors, d) subtraction of two photons at both detectors, e) and f) subtraction of one photon at one detector and no measurement at the other detector, and g) and h) subtraction of one photon at one detector and zero photons at the other detector.

A.5 Specifications of utilized devices

In this section, tabular specifications for the utilized devices and measurement results are provided. Table A.1 shows the device names of the components. Table A.2 gives a direct comparison of the two utilized laser systems. Table A.3 shows the settings and resulting efficiencies of the fiber-coupled single-photon detectors.

Table A.1: Overview of the devices used in the setup shown in Figure 3.2

Component	Device name
Laser 1	NKT Photonics Origami 15 LP
Laser 2	Calmar Cazadero FLCPA-02C
SHG crystal	Covesion MgO:ppLiNbO$_3$ MSGH1550
SPDC crystal	Bulk ppKTP, Paderborn University (IQO-Group)
VDL	OZ Optics Optical Delay Line ODL-650 (650 ps maximum delay)
Herald SNSPD	Photonspot SNSPD L225 (83 % detection efficiency at 1550 nm)

Table A.2: Datasheet comparison of the two used laser systems. *The repetition rate of Laser 2 can be varied in 16 steps, but is kept at a fixed repetition rate for this work.

Label	Laser 1	Laser 2
Device name	Origami laser	Cazadero laser
Central wavelength	1557.4 nm	1545.1 nm
Spectral bandwidth	13.8 nm	5.9 nm
Pulse length	191 fs	445 fs
Repetition rate	79.9 MHz	625.3 kHz *
Maximum pulse energy	1.98 nJ	3.23 µJ

Table A.3: Specifications of the utilized fiber-coupled superconducting nanowire single-photon detectors including the internal laboratory name, the set bias current on the detector's current source, the threshold voltage on the rising edge for the readout using a time tagger after signal amplification, and measured detection efficiency.

Category	Herald Detector	Detector 1	Detector 2	Detector 3	Detector 4
Identifier	L225	S302	S303	L254	L285
Bias current [μA]	9.2	5.4	5.8	11	17
Threshold voltage [mV]	50	50	50	20	20
Efficiency [%]	83 ±4 %	81 ±4 %	80 ±4 %	75 ±4 %	69 ±4 %

A.6 Single-photon source characterization using the Cazadero laser

As the utilized Cazadero laser (see Table A.1) was malfunctioning as explained in Section 3.1, this laser system could not be used for successful single-photon interference. However, the usage of the developed single-photon source setup can be interesting for future single-photon experiments where no interference effects are included. This section provides a characterization of this setup in analogy to Section 3.3.

Figure A.3 shows the wavelength spectrum of the Cazadero laser and the converted SHG spectrum. Both spectra are highly distorted. Despite this distortion, the $g^{(2)}[0]$-value is close to one (see Table A.4).

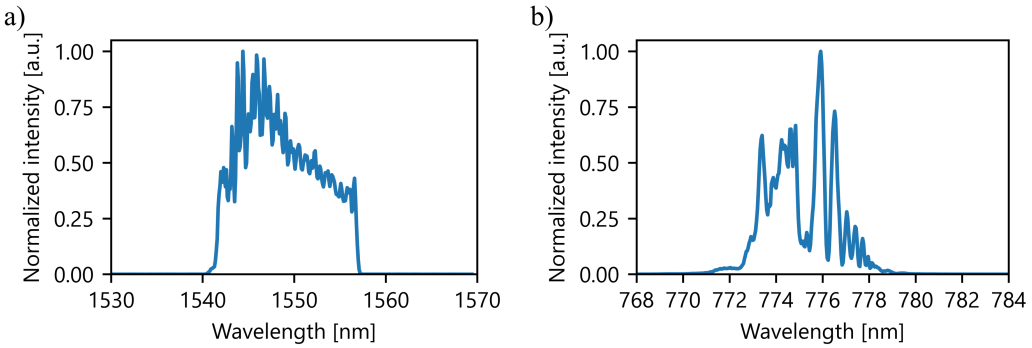

Figure A.3: Optical spectrum of a) the Cazadero laser and b) the spectrum of the SHG signal measured with an optical spectrum analyzer.

Table A.4: Measurement results for the second-order autocorrelation function $g^{(2)}[0]$ and contained laser and detection rates measured for 300 s and normalized to one second for the Cazadero laser.

R [1/s]	625307 ± 1
C_{Det1} [1/s]	4212 ± 4
C_{Det2} [1/s]	3572 ± 4
$C_{\text{Det1,Det2}}$ [1/s]	25 ± 1
$g^{(2)}(\Delta t = 0)$	1.04 ± 0.04

The resulting JSI measurement when pumping the periodically poled KTP crystal with the Cazazadero laser is shown in Figure A.4.

As the Cazadero pump spectrum is highly distorted, it creates correlations between signal and idler photons. Heralding on an idler photon, the signal photons are in multiple modes.

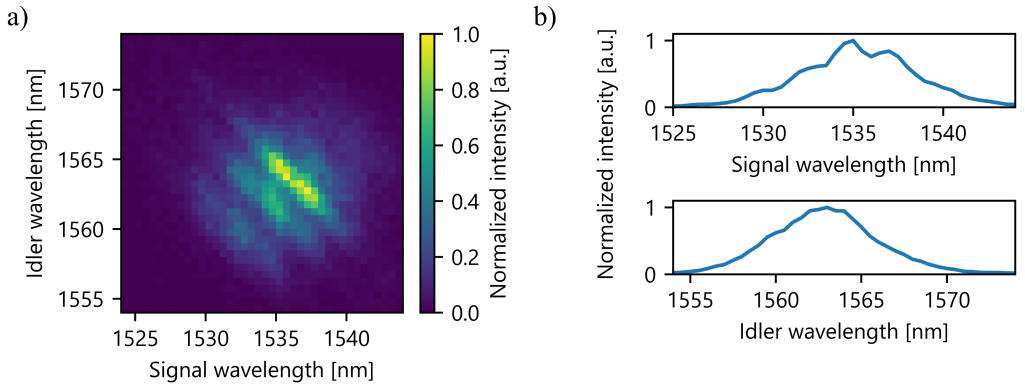

Figure A.4: a) Joint spectral intensity measurement pumping the KTP crystal with the frequency-converted Cazadero laser, and b) marginal spectra based on the horizontal or vertical integration of the JSI.

Using the 4f-line for the SHG signal in the setup (Figure 3.2), we can clean the pump spectrum. Closing the slit, narrows down the SHG spectrum as shown in Figure A.5.

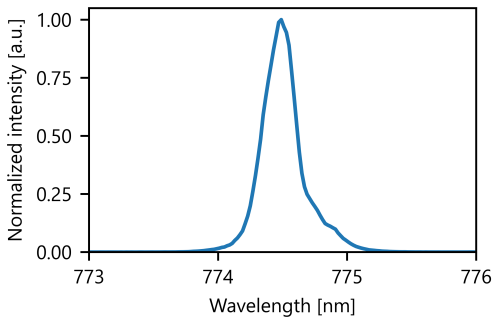

Figure A.5: Optical spectrum of the SHG signals using the Cazadero laser, measured with an optical spectrum analyzer.

Using the filtered SHG Cazadero pump results in an undistorted but correlated JSI, as shown in Figure A.6. As both arms (signal and idler photons) are strongly filtered, the individual countrates (number of clicks per second) are reduced. This results in only (71 ± 2) counts per second for the simultaneous detection of signal and herald photons for this configuration, as seen in Table A.5.

Furthermore, as can be seen when comparing the last two columns in Table 3.2, adding one filter in the herald arm can improve the heralding efficiency. All in all, the double-filtered source provides the highest heralding efficiency at the targeted wavelength.

When investigating the second-order autocorrelation function for this source as shown in Section 3.3.4, the creation of nonclassical states is verified while the additional filtering results in a Schmidt number close to one as shown in Table A.6.

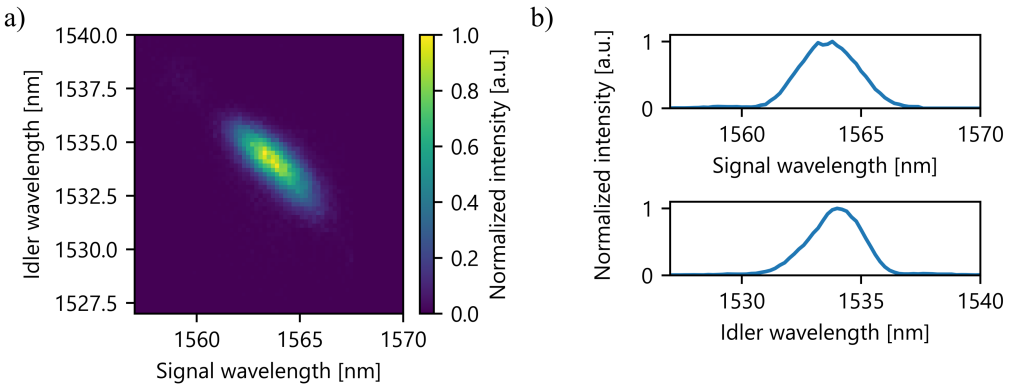

Figure A.6: a) Joint spectral intensity measurement pumping the KTP crystal with the filtered SHG signal of the Cazadero laser, and b) marginal spectra based on the horizontal or vertical integration of the JSI.

Table A.5: Measurement results for the heralding efficiency for the Cazadero laser system with and without the bandpass filter in the signal arm, and one bandpass filter in the signal and herald arm in the last column. The count and repetition rate are shown in 1/s, while the actual measurement was executed for 30 s. The shown detection efficiencies are based on an independent detection-efficiency characterization.

	No filter	Signal filter	Signal and idler filter
R [1/s]	625307 ± 1	625307 ± 1	625307 ± 1
$\eta_{\text{Det s}}$	0.80 ± 0.04	0.80 ± 0.04	0.80 ± 0.04
$\eta_{\text{Det h}}$	0.83 ± 0.04	0.83 ± 0.04	0.83 ± 0.04
$C_{\text{s}}[1/s]$	18117 ± 25	406 ± 4	934 ± 6
$C_{\text{h}}[1/s]$	13754 ± 21	15169 ± 22	1248 ± 7
$C_{\text{s,h}}$ [1/s]	3728 ±11	114 ±1.9	71 ±1.5
p_{s}	$2.897 \cdot 10^{-2}$ ± (0.14 %)	$6.49 \cdot 10^{-4}$ ± (1.0 %)	$1.49 \cdot 10^{-3}$ ± (0.7 %)
p_{h}	$2.199 \cdot 10^{-2}$ ± (0.15 %)	$2.426 \cdot 10^{-2}$ ± (0.15 %)	$1.97 \cdot 10^{-3}$ ± (0.6 %)
p_{cc}	$5.96 \cdot 10^{-3}$ ± (0.3 %)	$1.82 \cdot 10^{-4}$ ± (1.8 %)	$1.14 \cdot 10^{-4}$ ± (2.8 %)
$\eta_{\text{s}}\eta_{\text{Det s}}$ [%]	27.10 ± 0.09	0.752 ± 0.013	5.69 ± 0.16
η_{s} [%]	33.9 ± 1.7	0.94 ± 0.05	7.1 ± 0.4
p_{SPDC}	0.1069 ± 0.0004	0.0864 ± 0.0017	0.0263 ± 0.0006

Table A.6: Measurement results for the heralded and unheralded second-order autocorrelation function for 100 s for the two laser systems.

C_{s1}	37100 ± 190
C_{s2}	26490 ± 160
C_{h}	104000 ± 400
$C_{\mathrm{s1,\,s2}}$	30 ± 6
$C_{\mathrm{s1,\,h}}$	2970 ± 60
$C_{\mathrm{s2,\,h}}$	2100 ± 50
$C_{\mathrm{s1,\,s2,\,h}}$	4 ± 2
$g_u^{(2)}(\Delta t = 0)$	1.9 ± 0.4
K	1.1 ± 0.5
$g_h^{(2)}(\Delta t = 0)$	0.07 ± 0.03

A.7 Multi-channel fiber-pigtailing setup

In this section, the different steps for multi-channel fiber-pigtailing are shown.

Step 1: The fiber ferrule is attached to a six-axis motorized stage, held in place with a vacuum pump (Figure A.7 a)).

Step 2: The backreflection of the fiber ferrule is aligned with the angular adjustment of the six-axis motorized stage to be perpendicular to the incident beam and then moved aside (Figure A.7 a)).

Step 3: The waveguide sample is installed and its endface backreflection is aligned with a green alignment laser from the other side (Figure A.7 b)).

Step 4: The lenses and photodiode are placed in the setup with the subsequent alignment of the input lens focus, the horizontal and vertical position of the sample and output lens position (Figure A.7 c)).

Step 5: Waveguide coupling for one input of the multi-channel structure is optimized by maximizing the photocurrent of the photodiode for one of the outputs of the multi-channel structure (Figure A.7 c)).

Step 6: The output lens and photodiode are again exchanged with the already angular-aligned multi-channel fiber (Figure A.7 d)).

Step 7: Waveguide-to-chip coupling is optimized using two photodiodes connected to two neighboring fibers. For this, the six-axis motorized stage is optimized. As the coupling depends on the distance between the two endfaces, the fiber ferrule almost touches the waveguide endface in this step (Figure A.7 d)).

Step 8: The ferrule is moved backwards along the waveguide direction and a small drop of UV-glue (Norland 81) is placed at the ferrule endface (Figure A.7 e)).

Step 9: The ferrule is moved back to the previous position, where the liquid glue is connecting both endfaces and optical coupling is optimized with small adjustments. To improve temperature stability, the ferrule is pushed closer to the sample endface (Figure A.7 f)).

Step 10: Using first a ring of UV-LEDs mounted around the sample for 1 min and then a high-power UV-gun at different positions for 60 s, the UV-glue is cured (Figure A.7 g))

Step 11: After the UV-glue is fully cured, the vacuum pump is turned off and the six-axis motorized stage is moved backwards, leaving the fiber connected to the sample.

Step 12: To protect the fragile connection, a sideblock is mounted to the sample holder and the fiber is glued to this sideblock, again using the UV-glue and UV-gun (Figure A.7 h)).

Step 13: For pigtailing the second sample endface, the sample is turned around. At this stage the fiber-coupling efficiency for the first side can be measured with a powermeter. Next, all steps are redone with a reduced alignment procedure in Step 4 and Step 5, as the 1550 nm laser is now directly connected to the input fiber of the sample.

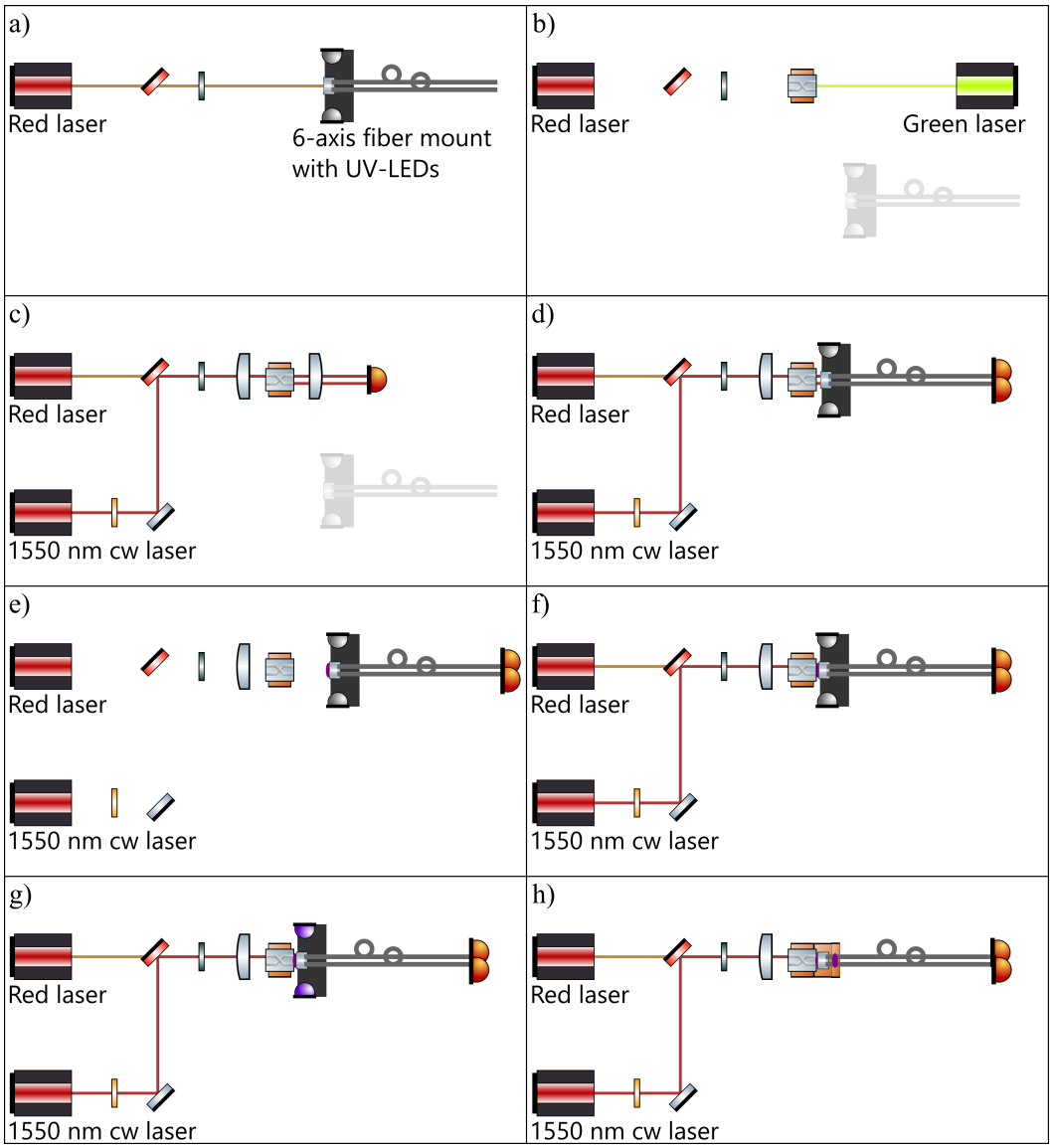

Figure A.7: Experimental setup for multi-channel fiber coupling divided in eight sub-figures, referenced in the text. The legend for unlabeled components is shown in Figure 4.4. Component drawings are partially taken from Reference [37].

A.8 Tabular measurement results for Chapter 5

In this section, tabular measurement results (Table A.7 - A.10) for the measured photon counts for the experiments in Chapter 5 are provided.

Table A.7: Measurement results for the different coincidental detection events, when interfering a coherent state and single photon from a PDC source for *optical circuit A*. A detection event of a herald photon is abbreviated with H. A detection event in Output 1 is abbreviated with O1, accordingly for the other outputs.

Detector combination	Total counts	Probability postselected on a herald detection
H	$6.53 \cdot 10^7$	1
O1	$7.813 \cdot 10^7$	-
O2	$1.013 \cdot 10^8$	-
O3	$6.818 \cdot 10^7$	-
O4	$7.004 \cdot 10^7$	-
HO1	$2.39 \cdot 10^5$	$3.663 \cdot 10^{-3}$
HO2	$3.025 \cdot 10^5$	$4.671 \cdot 10^{-3}$
HO3	$1.782 \cdot 10^5$	$2.2729 \cdot 10^{-3}$
HO4	$2.097 \cdot 10^5$	$3.21 \cdot 10^{-3}$
HO1O2	1422	$2.167 \cdot 10^{-5}$
HO1O3	420	$6.368 \cdot 10^{-6}$
HO1O4	454	$7.007 \cdot 10^{-6}$
HO2O3	522	$7.956 \cdot 10^{-6}$
HO2O4	597	$9.116 \cdot 10^{-6}$
HO3O4	776	$1.184 \cdot 10^{-5}$
HO1O2O3	1	$1.419 \cdot 10^{-8}$
HO1O2O4	3	$4.416 \cdot 10^{-8}$
HO1O3O4	1	$2.366 \cdot 10^{-8}$
HO2O3O4	2	$3.785 \cdot 10^{-8}$
HO1O2O3O4	0	0

Table A.8: Measurement results for the different coincidental detection events, when blocking the single photon state and just measuring the coherent state for *optical circuit A*. A detection event of a herald photon is abbreviated with H. A detection event in Output 1 is abbreviated with O1, accordingly for the other outputs.

Detector combination	Total counts	Probability postselected on a herald detection
H	$1.152 \cdot 10^8$	1
O1	$1.373 \cdot 10^8$	-
O2	$1.785 \cdot 10^8$	-
O3	$1.196 \cdot 10^8$	-
O4	$1.236 \cdot 10^8$	-
HO1	$3.22 \cdot 10^5$	$2.794 \cdot 10^{-3}$
HO2	$4.147 \cdot 10^5$	$3.599 \cdot 10^{-3}$
HO3	$2.503 \cdot 10^5$	$2.172 \cdot 10^{-3}$
HO4	$2.9 \cdot 10^5$	$2.516 \cdot 10^{-3}$
HO1O2	1118	$9.702 \cdot 10^{-6}$
HO1O3	682	$5.918 \cdot 10^{-6}$
HO1O4	905	$7.854 \cdot 10^{-6}$
HO2O3	900	$7.81 \cdot 10^{-6}$
HO2O4	1068	$9.268 \cdot 10^{-6}$
HO3O4	637	$5.528 \cdot 10^{-6}$
HO1O2O3	1	$8.678 \cdot 10^{-9}$
HO1O2O4	3	$2.603 \cdot 10^{-8}$
HO1O3O4	1	$8.678 \cdot 10^{-9}$
HO2O3O4	2	$1.736 \cdot 10^{-8}$
HO1O2O3O4	0	0

Table A.9: Measurement results for the different coincidental detection events, when interfering a coherent state and single photon from a PDC source for *optical circuit B*. A detection event of a herald photon is abreviated with H. A detection event in Output 1 is abbreviated with O1, accordingly for the other outputs.

Detector combination	Total counts	Probability postselected on a herald detection
H	$2.228 \cdot 10^8$	1
O1	$5.947 \cdot 10^8$	-
O2	$7.467 \cdot 10^7$	-
O3	$8.23 \cdot 10^8$	-
O4	$6.025 \cdot 10^8$	-
HO1	$1.698 \cdot 10^6$	$7.623 \cdot 10^{-3}$
HO2	$6.467 \cdot 10^5$	$2.902 \cdot 10^{-3}$
HO3	$1.63 \cdot 10^6$	$7.315 \cdot 10^{-3}$
HO4	$1.688 \cdot 10^6$	$7.577 \cdot 10^{-3}$
HO1O2	2644	$1.187 \cdot 10^{-5}$
HO1O3	13166	$5.909 \cdot 10^{-5}$
HO1O4	8332	$3.739 \cdot 10^{-5}$
HO2O3	4259	$1.911 \cdot 10^{-5}$
HO2O4	5534	$2.484 \cdot 10^{-5}$
HO3O4	11730	$5.265 \cdot 10^{-5}$
HO1O2O3	16	$7.181 \cdot 10^{-8}$
HO1O2O4	27	$1.212 \cdot 10^{-7}$
HO1O3O4	65	$2.917 \cdot 10^{-7}$
HO2O3O4	27	$1.212 \cdot 10^{-7}$
HO1O2O3O4	1	$4.488 \cdot 10^{-9}$

Table A.10: Measurement results for the different coincidental detection events, when blocking the single photon state and just measuring the coherent state for *optical circuit B*. A detection event of a herald photon is abbreviated with H. A detection event in Output 1 is abbreviated with O1, accordingly for the other outputs.

Detector combination	Total counts	Probability postselected on a herald detection
H	$1.134 \cdot 10^8$	1
O1	$2.78 \cdot 10^8$	-
O2	$3.511 \cdot 10^7$	-
O3	$3.864 \cdot 10^8$	-
O4	$2.819 \cdot 10^8$	-
HO1	$6.435 \cdot 10^5$	$5.673 \cdot 10^{-3}$
HO2	$7.877 \cdot 10^4$	$6.945 \cdot 10^{-4}$
HO3	$7.818 \cdot 10^5$	$6.892 \cdot 10^{-3}$
HO4	$6.538 \cdot 10^5$	$5.764 \cdot 10^{-3}$
HO1O2	438	$3.865 \cdot 10^{-6}$
HO1O3	4463	$3.935 \cdot 10^{-5}$
HO1O4	3750	$3.306 \cdot 10^{-5}$
HO2O3	538	$4.747 \cdot 10^{-6}$
HO2O4	451	$3.976 \cdot 10^{-6}$
HO3O4	4509	$3.975 \cdot 10^{-5}$
HO1O2O3	3	$2.471 \cdot 10^{-8}$
HO1O2O4	2	$1.812 \cdot 10^{-8}$
HO1O3O4	25	$2.241 \cdot 10^{-7}$
HO2O3O4	3	$2.471 \cdot 10^{-8}$
HO1O2O3O4	0	0

A.9 Transition edge sensors as a single-photon spectrometer

In this section, the usage of a transition edge sensor as single-photon spectrometer is discussed. Usually, the energy resolution of a transition edge sensor is used as a photon-number resolution for monochromatic light. Otherwise, the detection of one photon with a certain energy, results in the same detector response as the detection of two photons, each containing half the energy (twice the wavelength) of the first photon. As shown in Section 3.3.2, the spectrum of a single photon can be a crucial information.

For TESs, the energy resolution is defined as the FWHM of the one-photon peak divided by the photon energy (1550 nm wavelength correspond to 0.8 eV). The theoretical minimal energy resolution ΔE_{min} can be written as (Reference [80])

$$\Delta E_{\mathrm{min}} \approx 2.355\sqrt{4\sqrt{\frac{n}{2}}\mathrm{k_B}T_c E_{\mathrm{max}}}. \tag{A.59}$$

Here, n is the power law dependence of the thermal conductance, $\mathrm{k_B}$ is the Boltzmann constant, T_c is the critical temperature of the superconductor and E_{max} is the maximal accepted energy as

$$E_{\mathrm{max}} = \frac{CT_c}{\alpha}. \tag{A.60}$$

C is the heat capacity of the electron system and $\alpha = (d\ln R(T)/d\ln T)_{V=\mathrm{const}}$ for the sensors temperature dependent resistivity $R(T)$.

However, further noise terms from SQUID amplifiers as well as a non-unity coupling efficiency from the initial photon energy to the sensor (escape of phonons from the film before interacting with the electron system) must be included [80]. Using material parameters supplied by Brice Calkins for the tungsten TESs, we can investigate the energy resolution dependent on the detector volume. For this, a typical TES height of 20 nm is used. The resulting energy resolution over the square detector width is shown in Figure A.8 a). It can be seen that the energy resolution scales linearly with the detector width. Converting the energy resolution to a spectral resolution in Figure A.8 b) at a detector width of 10 µm, this corresponds to a FWHM of approximately 250 nm for the one-photon peak at 1550 nm wavelength. At 620 nm wavelength, it corresponds to a FWHM of 40 nm assuming a wavelength-independent energy resolution [113]. While this resolution is sufficient for photon counting (Rayleigh criterion [52] (p. 376)), it depends on the individual application and wavelength range of interest, if this resolution is practical [114]. As an example, Reference [115] shows the usage of TESs for RGB imaging. For a spectrally broadband use however, further system requirements (suitable SQUID amplifier settings and lower base temperature) must be fulfilled [116]. Especially for small detector widths, the detection efficiency strongly depends on the detector size and the detector is more sensitive to artifacts [80]. Here, integrated detectors can overcome this challenge as shown in Section 6.1.3.

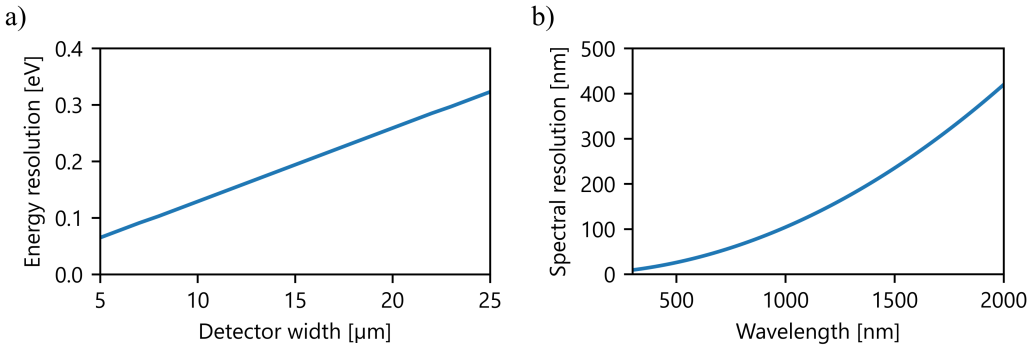

Figure A.8: a) TES energy resolution over the detector width at a fixed photon energy of 0.8 eV, and b) converted spectral resolution over wavelength for a fixed detector width of 10 µm.